

**NAVAL POSTGRADUATE SCHOOL
Monterey, California**



THESIS

**OPTIMUM SYMMETRICAL NUMBER SYSTEM
PHASE SAMPLED DIRECTION FINDING
ANTENNA ARCHITECTURES**

by

Thomas N. Hatziathanasiou

June 1998

Thesis Advisor:
Thesis Co-Advisor:

Phillip E. Pace
David D. Cleary

Approved for public release; distribution is unlimited.

DTIC QUALITY INSPECTED 1

19980727 164

REPORT DOCUMENTATION PAGE

Form Approved
OMB No. 0704-0188

Public reporting burden for this collection of information is estimated to average 1 hour per response, including the time for reviewing instruction, searching existing data sources, gathering and maintaining the data needed, and completing and reviewing the collection of information. Send comments regarding this burden estimate or any other aspect of this collection of information, including suggestions for reducing this burden, to Washington headquarters Services, Directorate for Information Operations and Reports, 1215 Jefferson Davis Highway, Suite 1204, Arlington, VA 22202-4302, and to the Office of Management and Budget, Paperwork Reduction Project (0704-0188) Washington DC 20503.

1. AGENCY USE ONLY (Leave blank)		2. REPORT DATE June 1998	3. REPORT TYPE AND DATES COVERED Master's Thesis	
4. TITLE AND SUBTITLE OPTIMUM SYMMETRICAL NUMBER SYSTEM PHASE SAMPLED DIRECTION FINDING ANTENNA ARCHITECTURES			5. FUNDING NUMBERS	
6. AUTHOR(S) Thomas N. Hatzithanasiou			8. PERFORMING ORGANIZATION REPORT NUMBER	
7. PERFORMING ORGANIZATION NAME(S) AND ADDRESS(ES) Naval Postgraduate School Monterey, CA 93943-5000			10. SPONSORING / MONITORING AGENCY REPORT NUMBER	
9. SPONSORING / MONITORING AGENCY NAME(S) AND ADDRESS(ES) None			11. SUPPLEMENTARY NOTES The views expressed in this thesis are those of the author and do not reflect the official policy or position of the Department of Defense or the U.S. Government.	
12a. DISTRIBUTION / AVAILABILITY STATEMENT Approved for public release; distribution is unlimited.			12b. DISTRIBUTION CODE	
13. ABSTRACT (maximum 200 words) A new interferometer direction finding array architecture based on the optimum symmetrical number system (OSNS) is presented. OSNS arrays are capable of unambiguous high-resolution direction finding with as few as three elements, with multiple baseline options. The OSNS DF antenna architecture being investigated uses the OSNS to decompose the analog spatial filtering operation into a number of parallel sub-operations (moduli) that are of smaller complexity. One two-element interferometer is used for each sub-operation and only requires a precision in accordance with its modulus. A much higher spatial resolution is achieved after the sub-operations are recombined. By incorporating the OSNS concept, the dynamic range of a specific configuration of antenna element spacings and comparator arrangements can be analyzed exactly. In this thesis, the OSNS DF antenna concept was demonstrated experimentally, by designing, fabricating and measuring the performance of a three-element array at 8.5 GHz. These three elements are grouped into two pairs (channels) according to the set of relatively prime moduli ($m_1 = 6$, $m_2 = 11$). A mixer is used to determine the phase difference between each pair of elements. The output voltage from the mixer in each channel is a symmetrical folding waveform that is DC biased and amplified using a summing amplifier. The output voltage of the amplifier is amplitude analyzed using a small comparator ladder. An EEPROM is used to recombine the results of these low precision channels to yield the high resolution direction of arrival (DOA). Simulated and experimental results are presented and compared.				
14. SUBJECT TERMS Direction Finding Antennas, Array Antennas, Rectangular Aperture Antennas, Open-ended Waveguides, Optimum Symmetrical Number System (OSNS), Weighted Summing Amplifier, Analog-to-Digital Converter, Comparator ladder.			15. NUMBER OF PAGES 215	
17. SECURITY CLASSIFICATION OF REPORT Unclassified			16. PRICE CODE	
18. SECURITY CLASSIFICATION OF THIS PAGE Unclassified		19. SECURITY CLASSIFICATION OF ABSTRACT Unclassified		20. LIMITATION OF ABSTRACT UL

NSN 7540-01-280-5500

Standard Form 298 (Rev. 2-89)
Prescribed by ANSI Std. Z39-18

Approved for public release; distribution is unlimited

**OPTIMUM SYMMETRICAL NUMBER SYSTEM
PHASE SAMPLED DIRECTION FINDING
ANTENNA ARCHITECTURES**

Thomas N. Hatziathanasiou
Major, Hellenic Air Force
B.S., Hellenic Air Force Academy, 1984

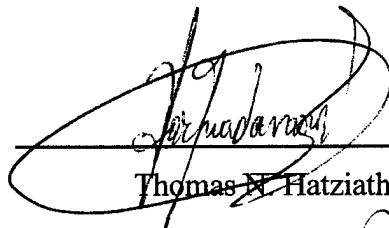
Submitted in partial fulfillment of the
requirements for the degree of

MASTER OF SCIENCE IN APPLIED PHYSICS

from the

**NAVAL POSTGRADUATE SCHOOL
June 1998**

Author:

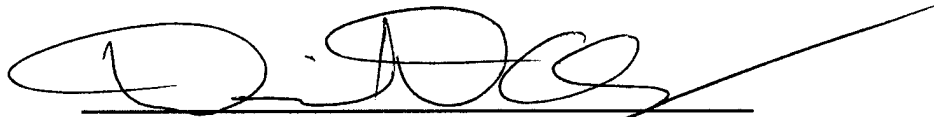


Thomas N. Hatziathanasiou

Approved by:



Phillip E. Pace, Thesis Advisor



David D. Cleary, Thesis Co-Advisor



William B. Maier, Chairman
Physics Department

ABSTRACT

A new interferometer direction finding array architecture based on the optimum symmetrical number system (OSNS) is presented. OSNS arrays are capable of unambiguous high-resolution direction finding with as few as three elements, with multiple baseline options. The OSNS DF antenna architecture being investigated uses the OSNS to decompose the analog spatial filtering operation into a number of parallel sub-operations (moduli) that are of smaller complexity. One two-element interferometer is used for each sub-operation and only requires a precision in accordance with its modulus. A much higher spatial resolution is achieved after the sub-operations are recombined. By incorporating the OSNS concept, the dynamic range of a specific configuration of antenna element spacings and comparator arrangements can be analyzed exactly. In this thesis, the OSNS DF antenna concept was demonstrated experimentally, by designing, fabricating and measuring the performance of a three-element array at 8.5 GHz. These three elements are grouped into two pairs (channels) according to the set of relatively prime moduli ($m_1 = 6$, $m_2 = 11$). A mixer is used to determine the phase difference between each pair of elements. The output voltage from the mixer in each channel is a symmetrical folding waveform that is DC biased and amplified using a summing amplifier. The output voltage of the amplifier is amplitude analyzed using a small comparator ladder. An EEPROM is used to recombine the results of these low precision channels to yield the high resolution direction of arrival (DOA). Simulated and experimental results are presented and compared.

TABLE OF CONTENTS

I.	INTRODUCTION	1
A.	DIRECTION FINDING ANTENNAS	1
B.	PRINCIPAL CONTRIBUTIONS	6
C.	THESIS OUTLINE	8
II.	LINEAR ARRAY ANTENNA ARCHITECTURE	11
A.	INTRODUCTION TO ARRAY ANTENNAS.....	11
B.	RADIATION FROM AN OPEN-ENDED WAVEGUIDE (TE ₁₀ MODE)	12
	Rectangular Aperture	15
C.	TWO-ELEMENT ARRAY ANTENNA	21
D.	N-ELEMENT LINEAR ARRAY ANTENNA	25
III.	PHASE SAMPLED LINEAR INTERFEROMETER DIRECTION FINDING (DF) ANTENNA	33
A.	PHASE COMPARISON SYSTEM	35
B.	MATHEMATICAL APPROACH FOR DETERMINING THE DOA ...	37
IV.	OPTIMUM SYMMETRICAL NUMBER SYSTEM (OSNS)	47

A.	OSNS PREPROCESSING	47
B.	OSNS ANTENNA ARCHITECTURE	50
V.	ANALOG TO DIGITAL CONVERSION (ADC)	57
VI.	DESIGN AND FABRICATION	65
A.	ARRAY ANTENNA	65
1.	Design of the Array and Ground Plane	66
2.	Low Noise Amplifiers (LNA)	75
3.	Phase shift alignment	80
4.	Mixer	81
5.	Construction and testing of the antenna	83
6.	Labview program for reading the mixer output voltage	90
B.	SUMMING AMPLIFYING CIRCUIT	91
C.	A/D CONVERSION BOARD	97
1.	Reference Voltage Generation Subsection	100
2.	Comparator Subsection	108
3.	EEPROM Section	114
VII.	SIMULATION RESULTS	119
VIII.	EXPERIMENTAL RESULTS AND COMPARISON WITH THE THEORETICAL ONES	127

A.	MIXER OUTPUT	127
B.	SUMMING AMPLIFIER OUTPUT	134
C.	A/D CONVERSION OUTPUT	135
IX.	SUMMARY AND CONCLUSIONS	137
	APPENDIX A. MATLAB CODES	141
	APPENDIX B. LABVIEW VI CODES	159
	APPENDIX C. MOD_EMUP PROGRAM FOR EEPROM	167
	APPENDIX D. MAX 916 DATA SHEETS.....	173
	APPENDIX E. LM 741CN DATA SHEETS.....	179
	APPENDIX F. XICOR X28C256 DATA SHEETS.....	183
	LIST OF REFERENCES	191
	INITIAL DISTRIBUTION LIST	193

LIST OF FIGURES

Figure 2.1: Actual and equivalent problem models:	14
(a) Actual problem	
(b) Equivalent problem	
Figure 2.2: Rectangular aperture on an infinite electric ground plane	15
Figure 2.3: Equivalent model for waveguide aperture mounted on an infinite flat electric ground plane	16
Figure 2.4: Aperture antenna analysis, where the right graph illustrates the far-field case	17
Figure 2.5: Geometry of a two-element linear array:	23
(a) Two infinitesimal dipoles	
(b) Far-field observations	
Figure 2.6: Far-field geometry of N-element linear array of isotropic sources	26
Figure 3.1: Functional Elements of the direction-finding process	34
Figure 3.2: Basic phase difference technique	36
Figure 3.3: Geometry for two disposed antenna elements	39
Figure 3.4: Angle of arrival vs phase difference at the elements for $d = \frac{\lambda}{2}$	41
Figure 3.5: Phase difference at the elements vs mixer output voltage for $d = \frac{\lambda}{2}$	43
Figure 3.6: Angle of arrival vs mixer output voltage for $d = \frac{\lambda}{2}$	44

Figure 3.7: Angle of arrival vs mixer output voltage for $d = 7.5\lambda$	46
Figure 4.1: OSNS folding waveforms and output codes for :	
$m_1=3$ and $m_2=4$, and $m_3=5$	49
Figure 4.2: Schematic representation of the OSNS antenna architecture for	
instantaneous direction finding	51
Figure 5.1: Block diagram of the basic elements of an A/D converter	57
Figure 5.2: Time-domain response of an ideal S/H circuit	58
Figure 5.3: Quantization Process	60
Figure 5.4: Transfer characteristic of an ideal ADC	61
Figure 6.1: Block diagram of the OSNS phase-sampled DF array antenna	
based on the moduli $m_1 = 6$ and $m_2 = 11$	67
Figure 6.2: Directional Finding Array Antenna Ground Plane Cutout	71
Figure 6.3: Rectangular aperture antenna element	72
Figure 6.4: TE ₁₀ waveguide cross-section with net electric fields	74
Figure 6.5: TE ₁₀ propagation electric fields	74
Figure 6.6: Transfer functions of the six low noise amplifiers	78
Figure 6.7: Transfer function of the six amplifiers (individually – in cascade)	79
Figure 6.8: Built antenna (front view), surrounded by absorber for reducing	
the edge effects	84
Figure 6.9: Built antenna (backside view), showing the parts of the construction	85
Figure 6.10: Antenna mounted on the pedestal, in the anechoic chamber	86
Figure 6.11: Ground plane with the antenna elements in detail	87

Figure 6.12: A focus on some components of the antenna:	88
(a) Big Low Noise Amplifiers (LNAs),	
(b) Small Low Noise Amplifiers (LNAs),	
(c) Wavegudes.	
Figure 6.13: A mixer connected at the system	89
Figure 6.14: Transmitting horn antenna in the anechoic chamber	89
Figure 6.15: Basic Inverting Summing Circuit	92
Figure 6.16: Weighted Summing Amplifier Circuit	95
Figure 6.17: Response of the Weighted Summing Amplifier circuit	96
Figure 6.18: Block Diagram of the A/D Conversion Board and the Logic Analyzer	97
Figure 6.19: Schematic Diagram of the Comparator board for Channel #1 (mod 6)	98
Figure 6.20: Schematic Diagram of the Comparator board for Channel #2 (mod 11)	99
Figure 6.21: Schematic Diagram of the EEPROM section and the Logic Analyzer	100
Figure 6.22: Schematic diagram illustrating the sub-circuit of resistors in series, with a potentiometer embedded, connected straight to each comparator subsection	104
Figure 6.23: Block diagram of a MAX916 comparator	110
Figure 6.24: The timing diagram for the clock function	112
Figure 6.25: Circuit symbol of the floating-gate MOSFET used as an EPROM cell	116
Figure 7.1: Mixer Output Voltage and the OSNS Quantization Code for the pair of elements (1,3) corresponding to modulus $m_1=6$	120
Figure 7.2: Mixer Output Voltage and the OSNS Quantization Code for the pair of elements (1,2) corresponding to modulus $m_2=11$	121

Figure 7.3: Comparator Outputs corresponding to modulus $m_1=6$ (thresholds T1 – T5)	122
Figure 7.4: Comparator Outputs corresponding to modulus $m_2=11$ (thresholds T1 – T5)	123
Figure 7.5: Comparator Outputs corresponding to modulus $m_2=11$ (thresholds T6 – T10)	124
Figure 7.6: OSNS Resolved Direction of Arrival for $-90^\circ < \phi < 90^\circ$ and the effect of the element factor (EF) on the array antenna transfer function	125
Figure 7.7: Simulated Transfer Function of OSNS antenna, for interval $-90^\circ < \phi < 90^\circ$, using $m_1=6$ and $m_2=11$	126
Figure 8.1: Experimental Measurements of the response of both channels.....	127
Figure 8.2: Experimental & Simulated folding waveforms using channel 1 ($m_1=6$) ...	128
Figure 8.3: Experimental & Simulated folding waveforms using channel 2 ($m_2=11$) ..	129
Figure 8.4: Wide angle experimental results due to edge effects for $m_1 = 6$	131
Figure 8.5: Wide angle experimental results due to mutual coupling and edge effects for $m_2=11$	132
Figure 8.6: Experimental antenna Transfer Function, using computer code	133
Figure 8.7: Summing Amplifier's Output Voltage	134
Figure 8.8: Experimental antenna Transfer Function	135
Figure 9.1: Trade-offs for two and three channel arrays for combinations of relatively prime integers less than 50. Each circle represents a unique OSNS configuration	140
Figure B.1: Configuration to link devices using a GPIB cable	159

Figure B.2: A GPIB Connector Showing Signal Assignment160

Figure B.3: Front Panel162

Figure B.4: Writes command string and send it to the GPIB device (multimeter)163

Figure B.5: Frame 1 waits for GPIB to assert SRQ164

Frame 2 reads measurement from multimeter.

Figure B.6: Clears the SRQ mode in order to be ready for the next request165

LIST OF TABLES

Table 4.1: Quantization of OSNS waveforms using moduli set $m_1=3$, $m_2=4$, and $m_3=5$	48
Table 4.2: Several OSNS arrays having the same Spatial Resolution ($M = 60$)	56
Table 6.1: OSNS Dynamic Range ($M = 66$) using moduli set $m_1 = 6$ and $m_2 = 11$	68
Table 6.2: Normalized Comparator Matching Threshold Values (Volts), for each pair of elements	103
Table 6.3: R_{ref_i} and the corresponding V_{ref_i} , for each channel	107
Table 6.4: Actual, measured values for the components included in each channel, for setting R_{ref_i} and the corresponding V_{ref_i}	108
Table 6.5: Translation of the thermometer code to a binary representation	113
Table 6.6: Transformation of binary to hexadecimal code and vice versa	117

ACKNOWLEDGEMENT

I would like to thank Professor Phillip E. Pace, my thesis advisor, for giving me the chance to work on this project, and for his patience, goodwill, and guidance. I would like to acknowledge the help of Professor David C. Jenn for his direction and advice. To my thesis co-advisor, Professor David Cleary, thank you for your consideration. To Bob Vitale, from the Microwave Laboratory, thank you for your cooperation and help in constructing the antenna, performing the experiments, and the measurements on the anechoic chamber. To Jeff Knight, thank you for your support in constructing some of the circuits and your help and experience in testing them. Special thanks to my lovely wife Louiza and my children for their support and patience during this long time of research. Thank you Lord for empowering me with courage, and blessing me with opportunity. A special mention goes to the Hellenic Air Force for giving me the opportunity to be intellectually challenged at the Naval Postgraduate School.

I. INTRODUCTION

A. DIRECTION FINDING ANTENNAS

In recent years, microwave passive direction finding (DF) has emerged as a distinct technology apart from HF/VHF and radar associated DF methods. With the advent of sophisticated high-performance anti-aircraft and anti-ship missile systems, electronic warfare has been tasked with the problem of recognizing not just the threat but rather the state it is in: acquisition, launch, and control or terminal guidance. The need for early warning and protection has led to the development of complex electronic warfare protection suites and radar warning receivers (RWR), both of which make extensive use of microwave passive DF methods. [Ref. 1]

A direction finding (DF) system is a passive device that determines the direction of arrival (DOA) of electromagnetic energy. It receives the incident electromagnetic wave, processes the received signal, and determines the direction of the transmitting source [Ref. 2]. DF systems provide several important functions in modern electronic warfare (EW) systems; they provide an emitter's bearing, or angle of arrival that can be used as an invariant sorting parameter in the deinterleaving of agile pulsed radar signals and in separating closely spaced communications emitters [Ref. 3]. DF systems are also used in a wide range of civilian and other military systems to provide an emitter's bearing [Ref. 4]. Applications include the identification of radar and communication systems, navigation and targeting, law enforcement, wildlife conservation, and signal intelligence [Ref. 4].

There are several desirable characteristics of a DF architecture. Among them are (1) high accuracy, (2) small response time, (3) small size (minimum number of antenna elements), (4) high resolution, (5) wide instantaneous bandwidth, and (6) wide instantaneous field of view. [Ref. 4]

Accuracy depends directly on the probability of detection of a receiving system, which depends upon false-alarm rate, type of receiver technique, the antenna system, and factors established by the target such as range, scan, and time modulation factors. Response time depends on the architecture used and the bandwidth. Other important performance metrics are the processing gain and the probability of intercept (POI). The antenna is a critical component of a DF system, and frequently is the limiting factor in the system performance. The antenna size has also traditionally been a problem. For example, high frequency (HF) DF arrays typically require a large spacing between the elements to obtain a fine spatial resolution. The large spacing becomes a packaging problem due to platform restrictions. [Ref. 4]

The DF systems are separated into three categories according to their aperture. They are: small-aperture (or narrow-aperture), medium-aperture, and large-aperture (or wide-aperture). Small-aperture systems generally have their aperture equal to half the wavelength of the highest frequency, while the large-aperture region is considered to start from about two times the wavelength. Medium-aperture systems are considered to start from 0.2 to 1.2 wavelengths. [Ref. 2]

DF systems fall into the three main categories of scanning beam, simultaneous-multiple-beam, and interferometer techniques. The mechanically scanning beam requires only

a single receiver and exhibits high sensitivity due to the use of a directive antenna. This technique has the disadvantage of having a low probability of intercept (POI). The simultaneous-multiple-beam system uses an antenna, or several antennas, forming a number of simultaneous beams, thereby retaining the high sensitivity of the scanning antenna approach while providing a fast response. However, it requires many parallel receiving channels, each with full frequency coverage. Interferometer systems, which by definition use phase-comparison techniques, have the advantage of fast response, but generally use wide-coverage antennas, which result in low sensitivity. In addition, they require relatively complex microwave circuitry, which must maintain a precise phase match over a wide frequency band under extreme environmental conditions. When high accuracy is required (on the order of 0.1 to 1 degree); wide baseline interferometers are utilized with ambiguity resolving circuitry. [Ref. 3]

The direction of arrival is mainly determined by one of three methods: (1) amplitude response, (2) time delay, or (3) phase difference, or phase sampling. In all three methods the angle of arrival of the electromagnetic wave is converted into a voltage, although the technique for interpreting the voltage is different in each case. All three methods contain ambiguities and limitations, which vary for each case. Also we have to keep in mind that the direction finding procedure is subject to several kinds of errors, which can accumulate under certain circumstances. [Ref. 5]

The amplitude response method mainly uses dipole-like antenna patterns to obtain the DF information. A radiation pattern of a dipole looks like an "eight;" it is broad at the maximum and sharp at the minimum. By rotating the dipole it is possible to find the direction

of the emitter with a relatively high accuracy; it will be the null position, where the voltage at the antenna terminals goes to zero. There is a 180-degree ambiguity, because of the pattern symmetry. If mechanical rotation of the dipole is not easy to accomplish, two dipoles positioned so as to give orthogonal patterns can be used. [Ref. 5]

Time delay techniques generally use long baselines of multiple wavelengths. Direction-of-Arrival information is obtained from the time difference between the arrival time of an electromagnetic wave at two separated antennas on a baseline of distance d . Time difference t is independent of the operating frequency, and is given by

$$t = \frac{d}{c} \sin \phi \quad (1-1)$$

where ϕ = angle of arrival of the electromagnetic wave.

Time delay, uses at least two antenna elements. This technique requires that one antenna be a reference antenna that starts the time-interval measurement. Following this technique, the direction of the emitter is obtained. [Ref. 2]

The phase sampled linear interferometer algorithm uses groups of antenna elements with different spacings to obtain time-of-arrival relationships that translate into measurable phase differences that are used to determine the angle of arrival. Since the distances from the emitter to the two elements are not the same (except for the broadside case), the incident wave arrives at the two antenna elements after traveling uneven path lengths, and thus it

arrives with a different phase. The direction resolving ability of the array generally increases with the spacing between the elements. However, widely spaced elements give rise to ambiguities in the direction estimate. The ambiguous measurements, from a widely spaced pair of elements, are resolved by another more closely spaced baseline pair. In principle, there is sufficient information from three elements to uniquely determine the angle of arrival to any desired accuracy. The phase that is sampled is proportional to the spacing, the wavelength, and the angle of incidence. Since the first two factors are constant, the DF information can be obtained. [Ref. 4]

This thesis describes the development and shows the results for a phase-sampled DF array antenna based on the optimum symmetrical number system (OSNS). The OSNS DF antenna architecture being investigated uses the OSNS to decompose the analog spatial filtering operation into a number of parallel sub-operations (moduli) that are of smaller complexity. One two-element interferometer is used for each sub-operation and only requires a precision in accordance with its modulus. A much higher spatial resolution is achieved after the spatial filtering results of the low precision sub-operations of all the OSNS moduli are recombined. Symmetrical number systems have been used previously to increase the efficiency of folding analog-to-digital converter architectures, efficiently encode digital antenna links, and increase the resolvable bandwidth of 2- and 3-channel digital intercept receivers. [Ref. 6-10]

B. PRINCIPAL CONTRIBUTIONS

This thesis describes the development and shows the experimental results for a new high-resolution phase-sampled DF array based on an Optimum Symmetrical Number System (OSNS) encoding technique. The use of the symmetrically folding phase waveform provides for a simple straightforward implementation.

The objective of this research is to experimentally investigate the fundamental OSNS phased sampled DF antenna concepts by building a prototype and measuring its performance in the anechoic chamber. The output of each channel is quantized using a small bank of comparators. The comparator matching threshold voltages for each channel are non-uniformly spaced. Using the binary outputs of the comparators an electrically erasable programmable read-only memory (EEPROM) maps the transfer function of the OSNS DF antenna and the DOA is determined.

An OSNS DF 2-channel antenna was designed having three separate antenna elements: one primary element and two secondary ones. Each one of the elements is a medium aperture radio direction finder that operates up to 8.5GHz. The output of the primary element is mixed with the output of each of the two secondary elements thus forming two output channels. The phase difference between the primary channel and the secondary channel is converted to a voltage. In each channel, the output phase signals are symmetrically folding waveforms with the folding period being a function of the channel modulus. The antenna was constructed and tested in the anechoic chamber. A weighted summing amplifier was designed, constructed, and connected to the mixer output of each channel in order to shift and amplify the symmetrically folding waveforms coming out of each mixer. An analog-

to-digital conversion board, for each channel, was designed and constructed using comparators as the main components for each board. The output of each weighted summing amplifier is amplitude analyzed by this small group of comparators. The comparator outputs represent the input phase response in a thermometer-like code that is eventually converted to a compact digital representation of the DOA. The conversion requires a logic block that is realized using an electrically erasable programmable read-only memory (EEPROM) Xicor X28C256, which was programmed to provide the desired direction of arrival. A high resolution DF is achieved after the N different SNS moduli are used and the results of these low-precision channels are recombined to yield the DOA. Labview codes were written for reading, and storing the data coming out of each part of the antenna structure.

A simulation, using Matlab, was developed to determine the expected results from the design, construction, and expected testing of the OSNS DF array antenna hardware simulation. A comparison between the experimental results and the simulation, are carried out and show close agreement demonstrating the feasibility of the concept.

The resulting angle of arrival estimates contain quantization errors that increase with the angle off of the electrical boresight. Also, the edge effects, that are present at the end-fire locations, give erroneous results. The phase responses for both channels were aligned at an input DOA of 50° . Encoding errors also appear when the sampled angle of arrival occurs about the code transition points. These errors occur, which occur when some of the comparators that is supposed to change state do not causing a large error in the resolved DOA. Interpolation and other SNS encoding schemes are being investigated to eliminate these occurrences.

C. THESIS OUTLINE

Chapter II presents a theoretical background material on the design and implementation of the linear array antenna. The radiation behavior of the individual rectangular aperture element is demonstrated. The equations giving the electric field at the rectangular aperture element are derived from its excitation. A 2- and N-element linear array antenna is investigated detailing the electric field pattern for each individual element and for the array antenna as a whole. The array factor (AF) associated with the linear array is derived. Chapter III describes the mathematical derivation of the phase difference between the antenna elements, how this phase difference is related to the mixer voltage output, and the determination of the direction of arrival of the signal from the source. Chapter IV is devoted to the encoding of the phase response with the OSNS. First the OSNS preprocessing is introduced. The OSNS antenna architecture is then derived including the inter-element spacing, the folding period for each channel and the spatial resolution of the array. Chapter V describes the process of converting the continuous-time (analog) signal to a digital sequence using analog-to-digital converter (ADC) devices. The ADC samples and quantizes the analog signal. Chapter VI describes the actual design and the fabrication of the direction finding architecture. It begins with the design of the three main parts; the array antenna (the ground plane and the individual components constructing the whole antenna), the weighed summing amplifier circuit, and the analog-to-digital converter, and the EEPROM. Individual components such as the low noise amplifiers and the mixers were measured on the network analyzer, and evaluated in the lab in order for their transfer response to be determined. The binary code, the gray code and the hexadecimal code used for mapping the electrically

erasable programmable read-only memory to determine the DOA is also described. Chapter VII presents the simulation results for each part of the architecture. Chapter VIII presents the experimental anechoic chamber results including the voltage output of the mixer for each channel, the voltage output of the weighted summing amplifier circuit, and the final results coming out of the A/D conversion system. Chapter IX presents a summary and states some conclusions and recommendations for future research. The Appendices provide the computer codes developed, (Matlab, Labview), and other useful design data, and details for a better understanding of the concept.

II. LINEAR ARRAY ANTENNA ARCHITECTURES

A. INTRODUCTION TO ARRAY ANTENNAS

Usually the radiation pattern of a single element is relatively wide, and each element provides low directivity (gain). In many applications it is necessary to design antennas with very directive characteristics (very high gain). This can only be accomplished by increasing the electrical size of the antenna. Enlarging the dimensions of single elements often leads to more directive characteristics. Another way to enlarge the dimensions of the antenna, without necessarily increasing the size of the individual elements, is to form an assembly of radiating elements in an electrical and geometrical configuration. The antenna formed by multi-elements is referred to as an *array antenna*, or simply an *array*. In most cases, the elements of an array are identical, although this is not necessary, it is often convenient, simpler, and more practical. The individual elements of an array may be of any form (wires, apertures, etc.). [Ref. 11]

The total field of the array is determined by the vector addition of the fields radiated by the individual elements, assuming that the current in each element is the same as that of the isolated element. This is usually not the case and depends on the separation between the elements. To provide very directive patterns, it is necessary that the fields from the elements of the array interfere constructively (add) in the desired direction and interfere destructively (cancel each other) in the remaining space. Ideally this can be accomplished, but practically it is only approached. In an array of identical elements, there are five controls that can be used to shape the overall pattern of the antenna. These are:

1. The geometrical configuration of the overall array (linear, rectangular, circular, spherical, etc.),
2. The relative displacement between the elements,
3. The excitation amplitude of the individual elements,
4. The excitation phase of the individual elements,
5. The relative pattern of the individual elements. [Ref. 11]

Placing the elements along a line forms the simplest, and one of the most practical arrays. This arrangement is the conventional *linear array* configuration. In addition to linear arrays (placing elements along a line), individual radiators can be positioned along a rectangular grid to form a rectangular or planar array. Planar arrays provide additional variables, which can be used to control and shape the pattern of the array. Planar arrays are more versatile and can provide more symmetrical patterns with lower side lobes. In addition, they can be used to scan the main beam of the antenna toward any point in space.

Applications include tracking radar, search radar, remote sensing, communications, and many others. Another class of arrays is that of the conformal arrays, where the element locations must conform to some non-planar surface such as that found on an aircraft or a missile. [Ref. 11]

B. RADIATION FROM AN OPEN-ENDED WAVEGUIDE (TE_{10} MODE)

After analyzing the array antenna theory, it would be useful if we could say some words about the aperture antennas and especially about rectangular aperture antennas.

An aperture antenna must have an aperture length and width of at least several wavelengths in order to have a high gain. Thus the aperture-type antennas find their most important applications in the microwave frequency band where the wavelength is only a few centimeters. The current distribution is not known exactly and only physical intuition or experimental measurements can provide a reasonable approximation to it. A very useful technique to determine the current distribution is the Field Equivalence Principle.

The Field Equivalence Principle is a principle by which actual sources, such an antenna, are replaced by equivalent sources. The fictitious sources are said to be equivalent within a region because they produce the same fields within that region. The equivalence principle is based on the uniqueness theorem, which states that:

A field in a lossy region is uniquely specified by the sources within the region plus the tangential components of the electric field over the boundary, or the tangential components of the magnetic field over the boundary, or the former over part of the boundary and the latter over the rest of the boundary. [Ref. 11]

The equivalence principle is developed by considering an actual radiating source, which electrically is represented by current densities \bar{J}_1 and \bar{M}_1 , as shown in Figure 2.1. The source radiates fields \bar{E}_1 and \bar{H}_1 everywhere. A closed surface S is chosen, which encloses the current densities \bar{J}_1 and \bar{M}_1 . The original sources \bar{J}_1 and \bar{M}_1 are removed,

and we assume that there exist fields \vec{E} and \vec{H} inside S and fields outside of S . For these fields to exist within and outside S , they must satisfy the boundary conditions on the tangential electric and magnetic field components. Thus on the imaginary surface S there must exist the equivalent sources

$$\vec{J}_s = \hat{n} \times [\vec{H}_1 - \vec{H}] \quad (2-1)$$

$$\vec{M}_s = -\hat{n} \times [\vec{E}_1 - \vec{E}]. \quad (2-2)$$

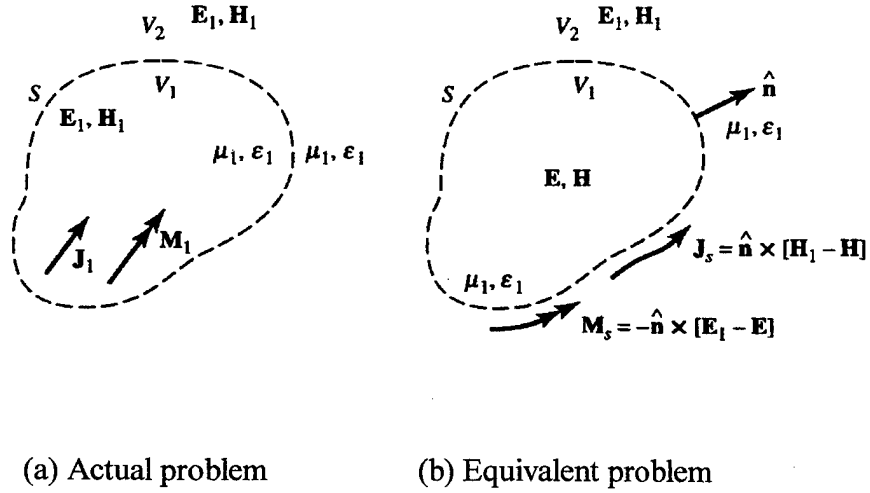


Figure 2.1: Actual and equivalent problem models [Ref. 5].

Since the fields \vec{E}, \vec{H} within S can be anything, it can be assumed that they are zero.

Then, the equivalent current densities being equal to

$$\vec{J}_s = \hat{n} \times [\vec{H}_1 - \vec{H}]_{\vec{H}=0} = \hat{n} \times \vec{H}_1 \quad (2-3)$$

$$\vec{M}_s = -\hat{n} \times [\vec{E}_1 - \vec{E}]_{\vec{E}=0} = -\hat{n} \times \vec{E}_1. \quad (2-4)$$

Rectangular Aperture

In practice, the rectangular aperture is probably the most common microwave antenna. A uniform distribution on an infinite ground plane is going to be examined first. A rectangular aperture, of dimensions a along x -axis and b along y -axis and located in the $z = 0$ plane, is shown in Figure 2.2.

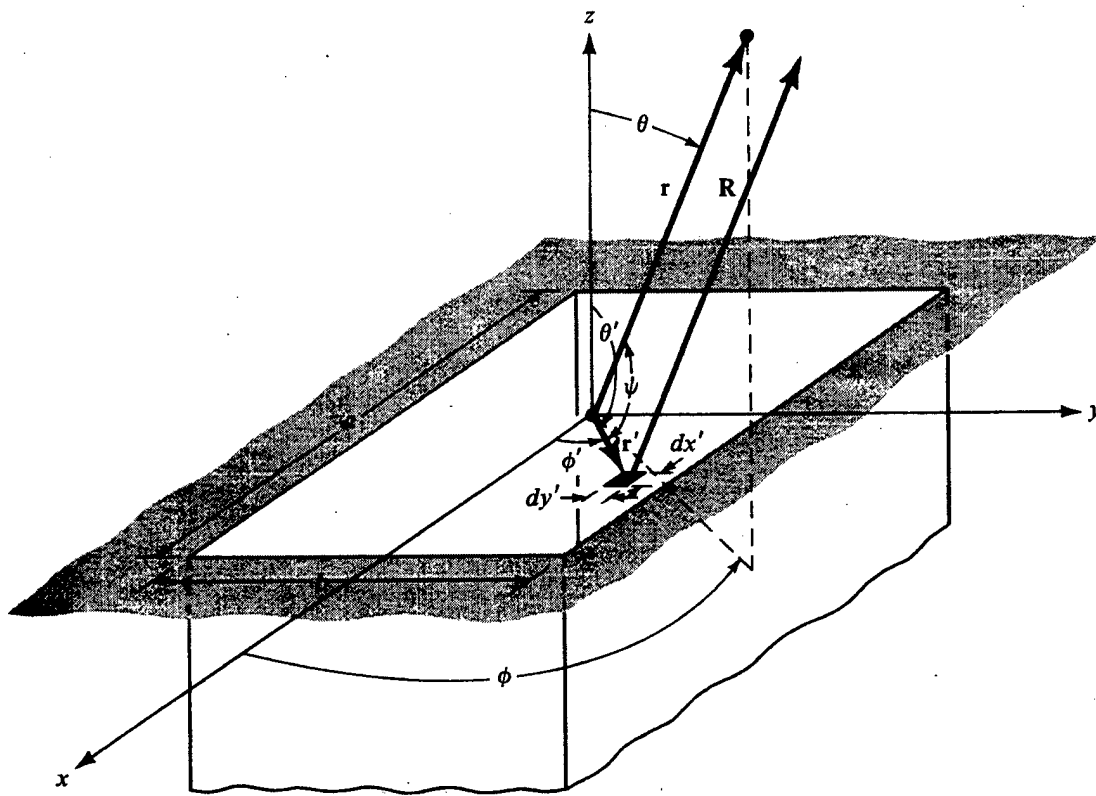


Figure 2.2: Rectangular aperture on an infinite electric ground plane [Ref. 5].

To reduce the mathematical complexities, the field over the opening (in the aperture) is assumed to be uniform and given by

$$\begin{aligned} \vec{E}_a &= E_o \cos\left(\frac{\pi x'}{a}\right) \hat{a}_y, & |x'| \leq \frac{a}{2}, & |y'| \leq \frac{b}{2} \\ &= 0, & \text{otherwise} \end{aligned} \quad (2-5)$$

where E_a is the electric field in the aperture, as shown in Figure 2-3 and E_o is a constant. In order to find the field the equivalent principle has to be applied and some approximations for the far-zone have to be determined.

Using the equivalent of Figure 2.3,

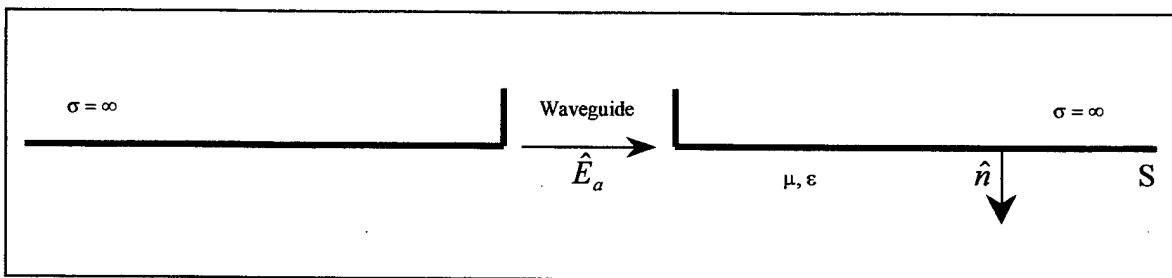


Figure 2.3: Equivalent model for waveguide aperture mounted on an infinite flat electric ground plane.

$$\left. \begin{aligned} \vec{M}_s &= -2\hat{n} \times \vec{E}_a = -2\hat{a}_z \times \hat{a}_y \cos\left(\frac{\pi x'}{a}\right) E_o = +\hat{a}_x 2 \cos\left(\frac{\pi x'}{a}\right) E_o, & |x'| \leq \frac{a}{2} \\ & & , |y'| \leq \frac{b}{2} \\ &= 0, & \text{elsewhere} \\ \vec{J}_s &= 0, & \text{everywhere.} \end{aligned} \right\} \quad (2-6)$$

For Far-Field observations R can be approximated by

$$R \approx r - r' \cos \psi \quad \text{for phase variations} \quad (2-7a)$$

$$R \approx r \quad \text{for amplitude variations,} \quad (2-7b)$$

where ψ is the angle between the vectors \bar{r} and \bar{r}' , as shown in Figure 2.2. The primed coordinates $(x', y', z'$, or $r', \theta', \phi')$ indicate the space occupied by the sources \bar{J}_s and \bar{M}_s , over which integration must be performed. The unprimed coordinates $(x, y, z$, or $r, \theta, \phi)$ represent the observation point. Geometrically the approximation of (2-7a) assumes that the vectors \bar{R} and \bar{r} are parallel, as shown in Figures 2.2 and 2.4.

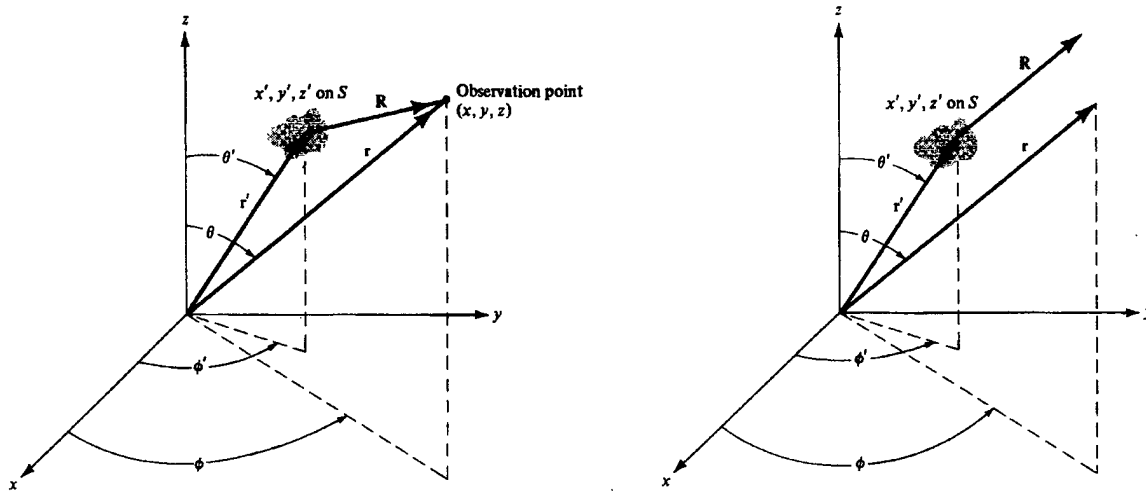


Figure 2.4: Aperture antenna analysis,

where the right graph illustrates the far-field case [Ref. 11].

The vector potential \vec{A} for an electric current source \vec{J} , and the vector potential \vec{F} for a magnetic source \vec{M} are given by the following expressions:

$$\vec{A} = \frac{\mu}{4\pi} \iiint_V \vec{J} \frac{e^{-jkR}}{R} dv' \quad (2-8)$$

$$\vec{F} = \frac{\varepsilon}{4\pi} \iiint_V \vec{M} \frac{e^{-jkR}}{R} dv' \quad \text{for } k^2 = \omega^2 \mu \varepsilon, \quad (2-9)$$

where the total fields are then given by

$$\vec{E} = \vec{E}_A + \vec{E}_F = -j\omega\vec{A} - j\frac{1}{\omega\mu\varepsilon}\nabla(\nabla \cdot \vec{A}) - \frac{1}{\varepsilon}\nabla \times \vec{F} \quad (2-10)$$

$$\vec{H} = \vec{H}_A + \vec{H}_F = \frac{1}{\mu}\nabla \times \vec{A} - j\omega\vec{F} - j\frac{1}{\omega\mu\varepsilon}\nabla(\nabla \cdot \vec{F}). \quad (2-11)$$

Since in our case $dz' = 0$, and due to equations (2-7a) and (2-7b) the equations (2-8) and (2-9) can be written as

$$\vec{A} = \frac{\mu}{4\pi} \iint_S \vec{J}_s \frac{e^{-jkR}}{R} ds' \approx \frac{\mu e^{-jkr}}{4\pi r} \iint_S \vec{J}_s e^{jkr' \cos \psi} ds' \quad (2-12)$$

$$\vec{F} = \frac{\varepsilon}{4\pi} \iint_S \vec{M}_s \frac{e^{-jkR}}{R} ds' \approx \frac{\varepsilon e^{-jkr}}{4\pi r} \iint_S \vec{M}_s e^{jkr' \cos \psi} ds'. \quad (2-13)$$

In the far field only the θ and ϕ components of the \vec{E} and \vec{H} fields are dominant. Although the radial components are not necessarily zero, they are negligible compared to θ and ϕ components. Combining the above equations the total \vec{E} and \vec{H} fields can be written as

$$E_r \approx 0 \quad (2-14a)$$

$$E_\theta \approx -\frac{jke^{-jkr}}{4\pi r}(L_\phi + \eta N_\theta) \quad (2-14b)$$

$$E_\phi \approx +\frac{jke^{-jkr}}{4\pi r}(L_\theta - \eta N_\phi) \quad (2-14c)$$

$$H_r \approx 0 \quad (2-14d)$$

$$H_\theta \approx \frac{jke^{-jkr}}{4\pi r}\left(N_\phi - \frac{L_\theta}{\eta}\right) \quad (2-14e)$$

$$H_\phi \approx -\frac{jke^{-jkr}}{4\pi r}\left(N_\theta + \frac{L_\phi}{\eta}\right), \quad (2-14f)$$

where $N_\theta, N_\phi, L_\theta, L_\phi$ are given by

$$N_\theta = \iint_S [J_x \cos\theta \cos\phi + J_y \cos\theta \sin\phi - J_z \sin\theta] e^{+jkr' \cos\psi} ds' \quad (2-15a)$$

$$N_\phi = \iint_S [-J_x \sin\phi + J_y \cos\phi] e^{+jkr' \cos\psi} ds' \quad (2-15b)$$

$$L_\theta = \iint_S [M_x \cos\theta \cos\phi + M_y \cos\theta \sin\phi - M_z \sin\theta] e^{+jkr' \cos\psi} ds' \quad (2-15c)$$

$$L_\phi = \iint_S [-M_x \sin \phi + M_y \cos \phi] e^{+jkr' \cos \psi} ds' . \quad (2-15d)$$

By combining the equations (2-6), (2-14), (2-15), and the expressions giving the differential path, as follows

$$\begin{aligned} r' \cos \psi &= \bar{r}' \cdot \hat{a}_r = (\hat{a}_x x' + \hat{a}_y y') \cdot (\hat{a}_x \sin \theta \cos \phi + \hat{a}_y \sin \theta \sin \phi + \hat{a}_z \cos \theta) \\ r' \cos \psi &= x' \sin \theta \cos \phi + y' \sin \theta \sin \phi, \end{aligned} \quad (2-16)$$

and the differential area ds' given by

$$ds' = dx' dy' , \quad (2-17)$$

the integrals $N_\theta, N_\phi, L_\theta, L_\phi$ become

$$N_\theta = N_\phi = 0 \quad (2-18)$$

$$\begin{aligned} L_\theta &= \int_{-b/2}^{+b/2} \int_{-a/2}^{+a/2} [M_x \cos \theta \cos \phi] e^{jk(x' \sin \theta \cos \phi + y' \sin \theta \sin \phi)} dx' dy' \\ L_\theta &= \cos \theta \cos \phi \left[\int_{-b/2}^{+b/2} \int_{-a/2}^{+a/2} M_x e^{jk(x' \sin \theta \cos \phi + y' \sin \theta \sin \phi)} dx' dy' \right]. \end{aligned} \quad (2-19)$$

By solving the above integrals and by substituting them into (2-14a-f), the fields radiated (or received) by the aperture can be written as

$$E_r = 0 \quad (2-20a)$$

$$E_\theta = j \frac{abkE_o e^{-jkr}}{r} \left[\sin \phi \left(\frac{\cos X}{\pi^2 - (2X)^2} \right) \left(\frac{\sin Y}{Y} \right) \right] \quad (2-20b)$$

$$E_\phi = j \frac{abkE_o e^{-jkr}}{r} \left[\cos \theta \cos \phi \left(\frac{\cos X}{\pi^2 - (2X)^2} \right) \left(\frac{\sin Y}{Y} \right) \right] \quad (2-20c)$$

$$H_r = 0 \quad (2-20d)$$

$$H_\theta = -\frac{E_\phi}{\eta} \quad (2-20e)$$

$$H_\phi = +\frac{E_\theta}{\eta}, \quad (2-20f)$$

where $X = k \frac{a}{2} \sin \theta \cos \phi$

$Y = k \frac{b}{2} \sin \theta \sin \phi.$

Above equations (2-20a)-(2-20f) represent the three-dimensional distributions of the far-zone fields radiated by the open-ended waveguides. [Ref. 11]

C. TWO-ELEMENT ARRAY ANTENNA

The total field of the array is determined by the vector addition of the fields radiated by the individual elements. Let us restrict our investigation in 1D arrays (linear array). Let us start the analysis assuming that the antenna under investigation is an array of two infinitesimal horizontal dipoles positioned along the z-axis, as shown in Figure 2.5(a).

The total field radiated by the two elements, assuming no coupling between them is equal to the sum of the two individual elements and is given by

$$\vec{E}_t = \vec{E}_1 + \vec{E}_2 = \hat{a}_\theta j\eta \frac{kI_o l}{4\pi} \left\{ \frac{e^{-j[kr_1 - (\beta/2)]}}{r_1} |\cos\theta_1| + \frac{e^{-j[kr_2 + (\beta/2)]}}{r_2} |\cos\theta_2| \right\}, \quad (2-21)$$

where $\eta = \sqrt{\frac{\mu}{\epsilon}} \equiv$ intrinsic impedance of the medium

$$k = \frac{2\pi}{\lambda} \equiv \text{wave number}$$

$I_o \equiv$ current (constant)

$l \equiv$ largest dimension of the antenna element

$\beta \equiv$ difference in phase excitation between the elements. [Ref. 11]

The magnitude excitation of the radiators is identical. Assuming far-field observations, as shown in Figure 2.5(b):

$$\theta_1 \approx \theta_2 \approx \theta \quad (2-22a)$$

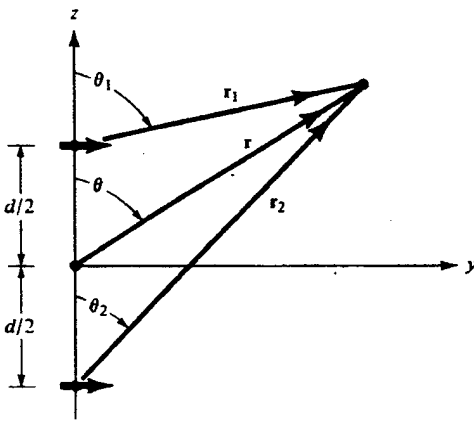
$$\left. \begin{aligned} r_1 &\approx r - \frac{d}{2} \cos\theta \\ r_2 &\approx r + \frac{d}{2} \cos\theta \end{aligned} \right\} \text{for phase variations} \quad (2-22b)$$

$$\left. \begin{aligned} r_1 &\approx r_2 \approx r \end{aligned} \right\} \text{for amplitude variations,} \quad (2-22c)$$

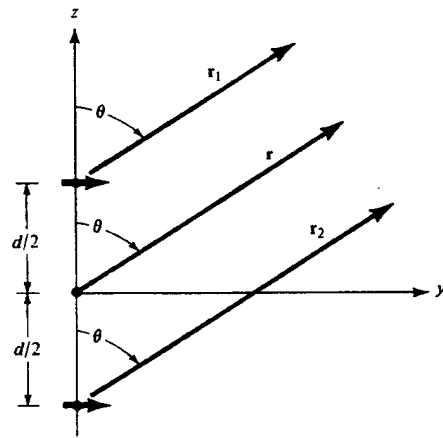
the equation (2-21) becomes

$$\vec{E}_t = \hat{a}_\theta j\eta \frac{kI_o l e^{-jkr}}{4\pi r} |\cos\theta| \left[e^{+j(kd \cos\theta + \beta)/2} + e^{-j(kd \cos\theta + \beta)/2} \right]$$

$$\vec{E}_t = \hat{a}_\theta j\eta \frac{kI_o l e^{-jkr}}{4\pi r} |\cos\theta| 2 \cos \left[\frac{1}{2} (kd \cos\theta + \beta) \right]. \quad (2-23)$$



(a) Two infinitesimal dipoles



(b) Far-field observations

Figure 2.5: Geometry of a two-element linear array [Ref. 11].

The total field of the array is equal to the field of a single element at the origin multiplied by a factor, which is widely referred to as the *array factor* (AF). Thus for the two-element array of constant amplitude, the array factor is

$$AF = 2 \cos \left[\frac{1}{2} (kd \cos\theta + \beta) \right]. \quad (2-24)$$

The array factor is a function of the geometry of the array and the excitation phase. By varying the separation d and /or the phase β between the elements, the characteristics of the array factor and of the total field of the array can be controlled.

The electric field pattern (far-field), of a uniform two-element array of identical elements, is equal to the product of the field of a single element (the element factor (EF)), at a selected reference point (usually at the origin), and the electric pattern of an array of isotropic point sources with the same locations, relative amplitudes and phases as the original array (the array factor (AF)) [Ref. 11], i.e.:

$$\vec{E}_{total}(\theta, \phi) = EF(\theta, \phi) \cdot AF(\theta), \quad (2-25)$$

where $\vec{E}_{total}(\theta, \phi) \equiv$ total radiated (or received) electric field intensity in the direction (θ, ϕ) .

This is referred to as *pattern multiplication* for arrays of identical elements. Each array has its own AF, which is a function of:

- * The number of elements
- * Their geometrical arrangement
- * Their relative magnitudes
- * Their relative phases

* Their spacing.

Although it has been illustrated only for an array of two elements, it is also valid for arrays with any number (N) of identical elements, which do not necessarily have identical magnitudes, phases, and/or spacing between them. Since the array factor does not depend on the directional characteristics of the radiating elements themselves, it can be formulated by replacing the actual elements with isotropic, point sources. [Ref. 11]

D. N-ELEMENT LINEAR ARRAY ANTENNA

After discussing the simple two-element array, it is useful to generalize the method to include N elements. A typical linear array composed of N similar element antennas is shown in Figure 2.6. Referring to the geometry of this Figure, let us assume, for convenience, that each antenna element is excited with the same constant amplitude $C=I_0$. However, there is a progressive phase change $\beta=\alpha d$ from element to element, so that $\alpha_n=n\alpha d$. The term, $\beta=\alpha d$, represents the phase by which the current in each element leads the current of the preceding element. Also, the pattern of each element leads to a response that varies with the angle of arrival of the incoming plane wave.

The array factor can be obtained by considering the elements to be point sources. If the actual elements are not isotropic sources, the total field can be formed by multiplying the array factor of the isotropic sources by the field of a single element. This is the pattern multiplication rule, and it applies only for arrays of identical elements. The radiation fields of a point source at the origin of a spherical coordinate system are

proportional to $I_o \frac{e^{-jkr}}{4\pi r}$, where I_o is the current of the point source, $k = \frac{2\pi}{\lambda}$ is the wave number, and r is the radius of the sphere.

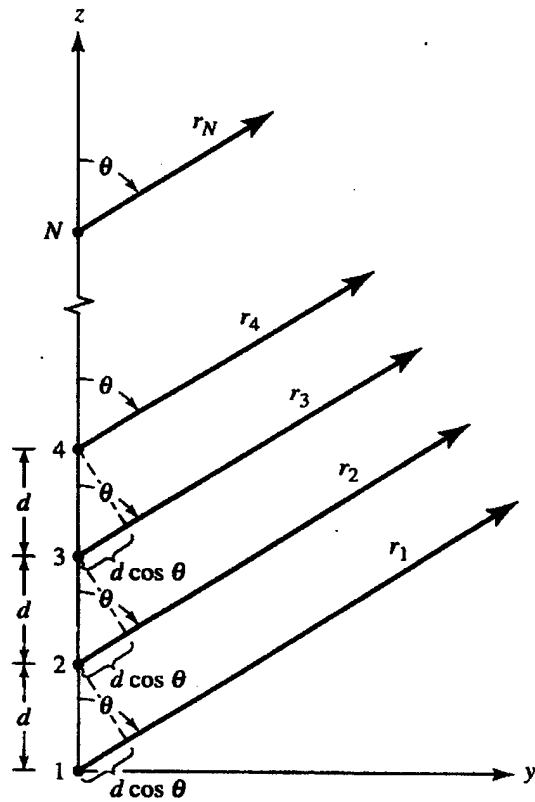


Figure 2.6: Far-field geometry of N -element linear array of isotropic sources [Ref. 11].

The far-field pattern is obtained from the angular dependence of the radiation fields. The array factor for the receiving array is the sum of the point source response $e^{j\psi_m}$

each weighted by the amplitude and phase shift I_n introduced in the transmission line connected to each n^{th} element. The phase difference between adjacent elements is defined as $\psi = kdcos\theta + \beta$. The array factor of the array shown in the Figure 2.6 is given by:

$$AF = I_0 + I_1 e^{+jkd \cos \theta} + I_2 e^{+j2kd \cos \theta} + \dots + I_{N-1} e^{+j(N-1)kd \cos \theta}$$

$$AF = \sum_{n=0}^{N-1} I_n e^{jnkd \cos \theta} \quad (2-26)$$

If we can say that the current has a linear phase progression (i.e., the relative phase between adjacent elements is the same), the phase can be separated as

$$I_n = A_n e^{jn\beta} \quad (2-27)$$

where one can realize that the $n+1$ element leads the n^{th} element in phase by β . Then the equation (2-26) can be written as

$$AF = \sum_{n=0}^{N-1} A_n e^{jn(kd \cos \theta + \beta)} \quad (2-28)$$

From the previous analysis, ψ_n is the phase of an incoming plane wave at the n^{th} element location. Then we can write the equation (2-28) as

$$AF = \sum_{n=0}^{N-1} A_n e^{jn\psi} . \quad (2-29)$$

An array of identical elements, all of identical magnitude, and each with a progressive phase, is referred to as a uniform array. Since it is a uniformly excited array, all the elements have identical current amplitudes, so that:

$$A_0 = A_1 = A_2 = \dots = A_{N-1} . \quad (2-30)$$

If we define the current amplitude to be equal with the unity, the array factor from equation (2-29) is then

$$AF = \sum_{n=0}^{N-1} e^{jn\psi} \quad (2-31)$$

$$AF = 1 + e^{j\psi} + e^{j2\psi} + \dots + e^{j(N-1)\psi} .$$

The amplitude and phase of the AF can be controlled in uniform arrays by properly selecting the relative phase ψ between the elements; in non-uniform arrays, the amplitude as well as the phase can be used to control the formation and distribution of the total array factor.

The array factor of equation (2-31) can also be expressed in an alternate (compact) form. After multiplying both sides, of the above equation, by $e^{j\psi}$ and subtracting one equation from the other, we end up with a compact form

$$AF = \left[\frac{e^{jN\psi} - 1}{e^{j\psi} - 1} \right] = e^{j[(N-1)/2]\psi} \left[\frac{e^{j(N/2)\psi} - e^{-j(N/2)\psi}}{e^{j(1/2)\psi} - e^{-j(1/2)\psi}} \right]$$

$$AF = e^{j[(N-1)/2]\psi} \left[\frac{\sin\left(\frac{N}{2}\psi\right)}{\sin\left(\frac{1}{2}\psi\right)} \right]. \quad (2-32)$$

If the reference point is the physical center of the array, the phase factor of the array $e^{j[(N-1)/2]\psi}$ can be neglected and the array factor reduces to

$$AF = \left[\frac{\sin\left(\frac{N}{2}\psi\right)}{\sin\left(\frac{1}{2}\psi\right)} \right]. \quad (2-33)$$

The maximum value of the array factor is equal to N and occurs when $\psi=0$:

$$AF_{\max} = N.$$

To normalize the array factors so that the maximum value of each is equal to unity, the equation (2-33) is written in normalized form as

$$(AF)_{normalized} = \frac{1}{N} \left[\frac{\sin\left(\frac{N}{2}\psi\right)}{\sin\left(\frac{1}{2}\psi\right)} \right] \quad (2-34)$$

and for small values of ψ , the above expressions for the array factors become

$$AF \approx \left[\frac{\sin\left(\frac{N}{2}\psi\right)}{\frac{\psi}{2}} \right] \quad (2-35)$$

$$(AF)_{normalized} \approx \left[\frac{\sin\left(\frac{N}{2}\psi\right)}{\frac{N\psi}{2}} \right]. \quad (2-36)$$

The maximum values of equation (2-35) occur when $\psi = kd\cos\theta + \beta$.

$$\left. \left(\frac{\psi}{2} = \frac{1}{2}(kd \cos\theta + \beta) \right) \right|_{\theta=\theta_m} = \pm m\pi, \text{ i.e. when}$$

$$\theta_m = \cos^{-1} \left[\frac{\lambda}{2\pi d} (-\beta \pm 2m\pi) \right] \quad \text{for } m=0,1,2,\dots \quad (2-37)$$

The array factor of equation (2-36) has only one maximum value and occurs when $m=0$, in equation (2-37). That is

$$\theta_m = \cos^{-1} \left(\frac{\lambda}{2\pi d} \beta \right) \quad (2-38)$$

which is the observation angle that makes $\psi=0$. [Ref. 11]

In this Chapter the antenna (element – array) theory has been presented. In the next Chapter the theory of linear antenna is going to be used for deriving the phase difference between the antenna elements and determining the DOA.

III. PHASE SAMPLED LINEAR INTERFEROMETER DIRECTION FINDING (DF) ANTENNA

Radio direction finding is a class of direction finding by which the direction to a radio source is determined by means of a radio direction finder (RDF). A radio direction finder is a passive device that determines the DOA of radio frequency energy. A RDF is a receiving system that operates on the energy extracted from the passing electromagnetic radio wave to obtain DOA information. [Ref. 2]

A radio direction finding system consists of four essential functional elements, as shown in Figure 3.1. The antenna extracts the electromagnetic energy and converts it to a signal containing direction-of-arrival information. The receiver down converts, amplifies, and processes the antenna signal to intermediate frequencies (IF) or baseband. The post-receiver processor further processes the signal to obtain the DOA information. The DF information processing-read-out-display unit prepares the basic DOA data for transmission to users of the DF information. The antenna is the key subsystem in a RDF. It extracts energy from the incident electromagnetic field and provides output signals containing the incident energy DOA information. [Ref. 2]

The primary function of radio direction finding system is to determine the direction of arrival of an incident electromagnetic wave as received at the RDF site. A representative direction finding spatial coordinate system with the DF located at the origin.

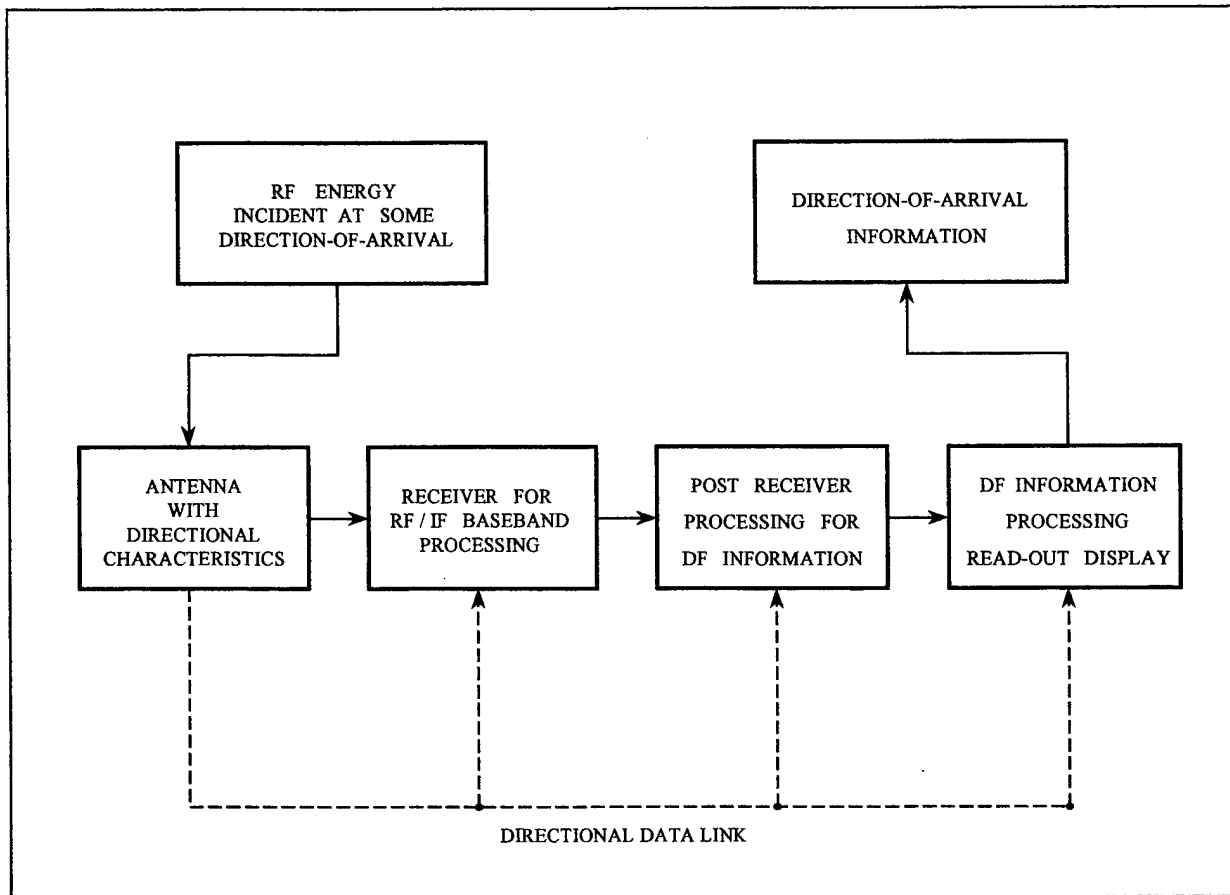


Figure 3.1: Functional Elements of the direction finding process [Ref. 2].

At microwave frequencies, antennas have aperture sizes of several wavelengths. Small aperture RDFs determine direction-of-arrival information by one for the following three measurement methods [Ref. 2]:

1. Amplitude response,
2. Phase difference,
3. Time delay.

More specifically, small aperture DF systems may be separated into four functional categories based on the fundamental measurement methods presented above. The four (4) basic categories are as follows [Ref. 2]:

Category I: Systems using either direct or comparative amplitude response of the antenna subsystem for DOA information.

Category II: Systems using the phase difference between disposed antenna elements with the phase differential converted to amplitude DOA information.

Category III: Systems using the phase difference between disposed antenna elements for DOA information.

Category IV: Systems using the time-of-arrival difference between disposed antenna elements for DOA information.

Each category may be subdivided into system classes based on antenna type, receiver channelization level, and DOA acquisition technique. [Ref. 2]

A. PHASE COMPARISON SYSTEM

Phase comparison DF systems determine DOA information by direct phase comparison of the subject signal received by separate, disposed antennas. Bearing measurements using phase difference require at least two separated antennas. A plane wave, arriving at an angle other than normal to the baseline, arrives at one element earlier than the other. The time lag produces a RF phase delay or a differential RF phase between the antenna element outputs. Figure 3.2 illustrates the basic phase difference technique. An incident plane wave arrives at an incident angle ϕ at antenna 1 inducing a voltage

$V_1 = e^{j\omega t}$. After propagating the distance $d \sin \phi$, the incident plane wave induces a voltage $V_2 = e^{(j\omega t - \delta)}$ in antenna 2, where δ is the phase difference between the two elements given by

$$\delta = \frac{2\pi}{\lambda} d \sin \phi. \quad (3-1)$$

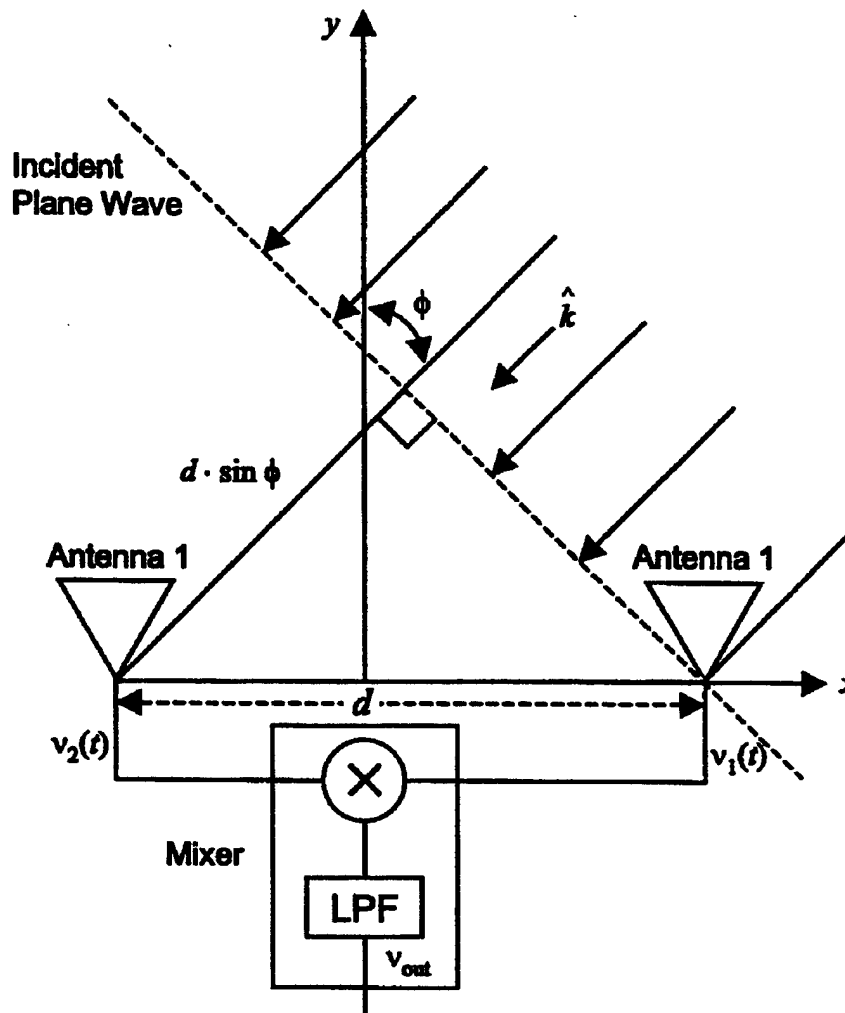


Figure 3.2: Basic Phase difference technique.

Therefore, the bearing angle ϕ is encoded as a function of the measured phase delay δ and computed by using the above equation. Phase difference techniques experience phase and bearing ambiguities if $d > \lambda/2$. For small aperture DF applications however, phase ambiguities are not a problem.

B. MATHEMATICAL APPROACH FOR DETERMINING THE DOA

By using the geometry for two disposed antenna elements, as shown in Figure 3.4, we can determine the DOA from the phase difference between the elements. In Figure 3.3, there are two antenna elements with baseline spacing d and an incident signal at an angle ϕ relative to the bore-sight z-y plane. The incident angle ϕ takes values from $-\pi/2$ to $\pi/2$. The elevation angle is θ , in general, but since only waves arriving in the x-y plane have been considered the elevation angle is 90° .

The instantaneous electric field propagating toward the array in free space is given by

$$\bar{E}(t, k) = \hat{z} \cdot E_o \cdot e^{j\omega t - kr}, \quad (3-2)$$

where E_o is the maximum value of the electric field

$\omega = 2\pi f$ is the frequency

r is the distance traveled from source

$k = \frac{2\pi}{\lambda}$ is the magnitude of the unit vector of the direction of wave propagation

given by $\hat{k} = -(\hat{x} \cdot \sin\phi + \hat{y} \cdot \cos\phi)$ and $kr = -k(x\cos\phi + y\sin\phi)$.

The voltage received by antenna 1 may be expressed in exponential form, like the electric field, as follows

$$V_1 = Ve^{j\omega t - kr}, \quad (3-3)$$

where V is the initial transmitted signal amplitude

r, k are the same as above for electric field form,

and in a like manner at antenna 2

$$V_2 = Ve^{j\omega t - kr + d \sin\phi}, \quad (3-4)$$

where the term $d \sin\phi$ represents the additional path length to antenna 2 as referenced to antenna 1. Since we are interested in relative phase differences between the two received voltages, V_1 and V_2 , we can assume kr to be reference zero at antenna 1; then

$$V_1 = Ve^{j\omega t} = Ve^{j2\pi ft} \quad (3-5)$$

and

$$V_2 = Ve^{j\omega t + d \sin\phi} = Ve^{j2\pi ft + d \sin\phi}. \quad (3-6)$$

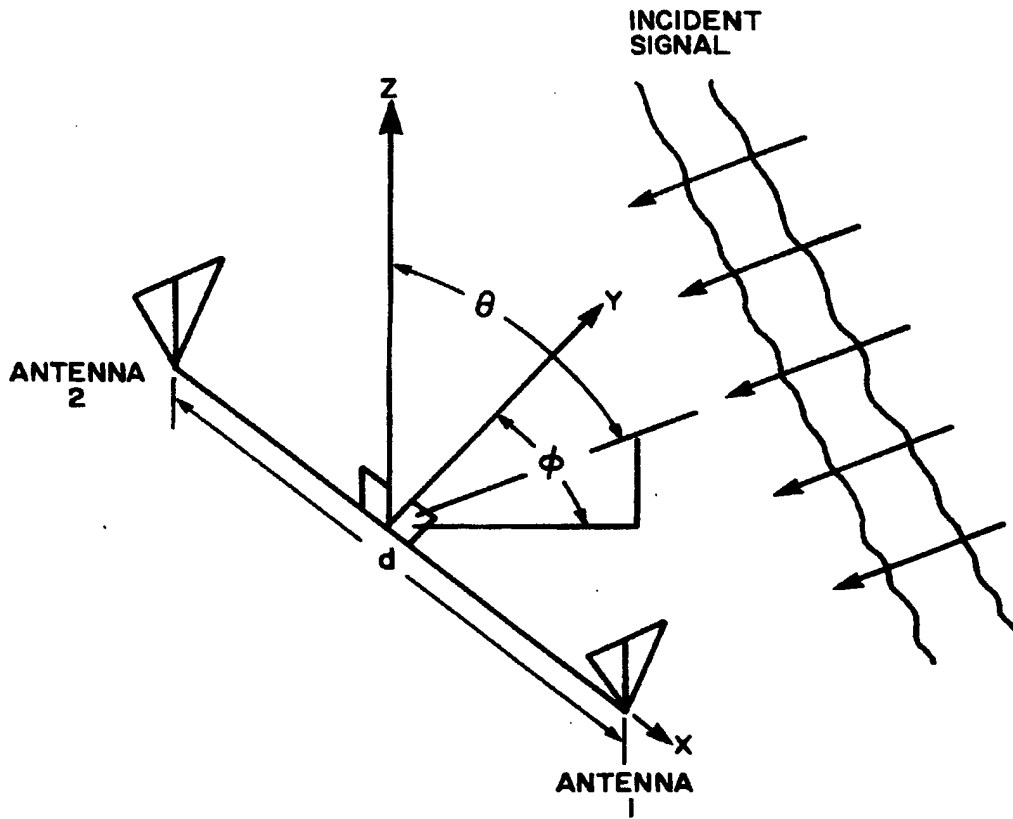


Figure 3.3: Geometry for two-disposed antenna elements [Ref. 2].

Without affecting the general case we can assume that the phase of the wave arriving at the first element at time t is $\delta_1 = 2\pi ft$. The wave arrives at antenna element 2 after travelling an additional distance of $d \sin \phi$. The phase of the wave arriving at the second

element is then $\delta_2 = 2\pi ft - \frac{2\pi}{\lambda} d \sin \phi$. The phase difference between the two elements is

$\delta = \delta_1 - \delta_2$ given by

$$\delta = \frac{2\pi}{\lambda} d \sin \phi. \quad (3-7)$$

The last equation represents the relationship between the angle of incidence ϕ of the electromagnetic wave, and the phase difference δ between the two antenna elements. If we would like to extract the angle of incidence ϕ in a straight manner we could transform the last expression by the following way

$$\phi = \sin^{-1} \left(\frac{\lambda}{2\pi d} \delta \right). \quad (3-8)$$

If, for example, the baseline d is half the wavelength λ or less, the phase difference is between $-\pi$ and π . For every value of phase difference there is only one unique angle of incidence. In this case no ambiguities exist. With distance between the two elements equal to one half the wavelength, the phase difference is $\delta = \pi \sin \phi$ and it is plotted in Figure 3.4.

The signals received by the antenna elements are fed to a mixer. The mixer multiplies its two input signals and passes the product through a low pass filter (LPF). The two signals at the mixer input, in this case, are two sinusoidal signals of the same frequency (8.5 GHz), but with different phases α_1 and α_2 . These input phases are not purely δ_1 and δ_2 , because of the phase delays due to the lengths of the wiring from the antenna to the mixer. Each branch introduces a constant phase shift, which is added to the

phase at the respective elements. The phase shifts generally are different, but their difference is constant δ_0 , which can be measured. Thus the phase difference α at the input of the mixer can be calculated from

$$\alpha = \delta + \delta_0. \quad (3-9)$$

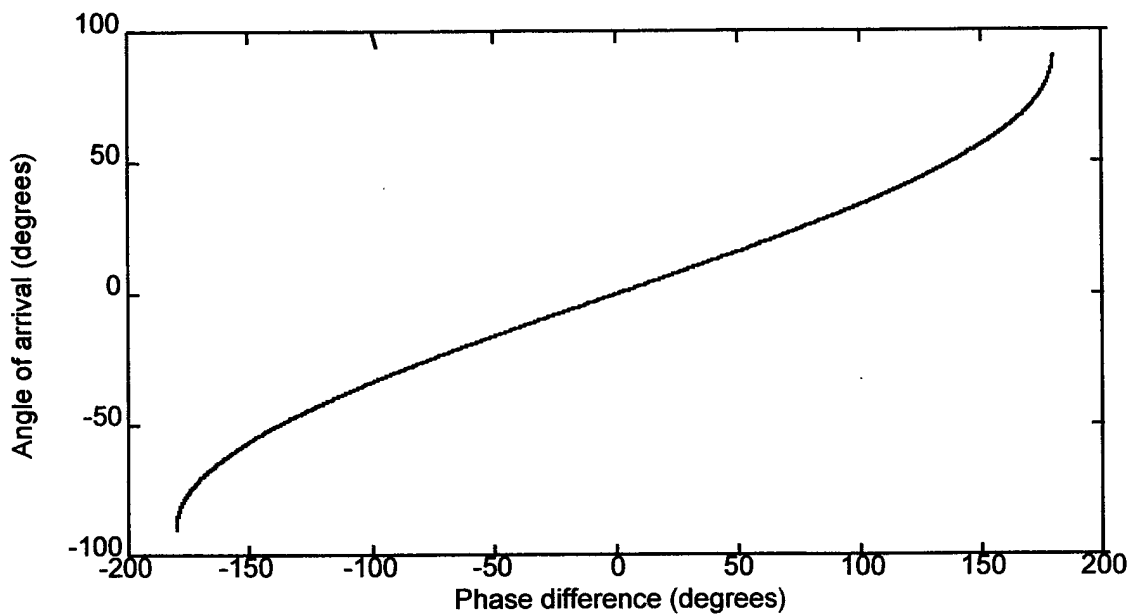


Figure 3.4: Angle of arrival vs phase difference at the elements for $d = \frac{\lambda}{2}$.

Alternately, if we choose the length of the cable to be equal for both branches, $\alpha = \delta$. The latter approach of equal paths is preferred, but sometimes is not possible to achieve because of the circuit layout constraints.

Let the signals from the two antenna elements be of the form

$$v_1 = V \cos(2\pi ft + \alpha_1) \quad (3-10)$$

$$v_2 = V \cos(2\pi ft + \alpha_2), \quad (3-11)$$

where, V is the maximum value of the voltage at the element terminals due to the incident wave, and f is the frequency of 8.5 GHz.

The mixer output voltage is

$$\begin{aligned} v_{out}|_{mixer} &= v_1 \cdot v_2 \\ v_{out}|_{mixer} &= [V \cos(2\pi ft + \alpha_1)] \cdot [V \cos(2\pi ft + \alpha_2)] \\ v_{out}|_{mixer} &= V^2 \cdot \cos(2\pi ft + \alpha_1) \cdot \cos(2\pi ft + \alpha_2) \\ v_{out}|_{mixer} &= \frac{V^2}{2} \cdot [\cos(4\pi ft + \alpha_1 + \alpha_2) + \cos(\alpha_1 - \alpha_2)]. \end{aligned} \quad (3-12)$$

The low pass filter removes the high frequency term on the right hand side of equation (3-12), leaving

$$v_{out}|_{LPF} = \frac{V^2}{2} \cdot \cos(\alpha_1 - \alpha_2)$$

or

$$v_{out}|_{LPF} = \frac{V^2}{2} \cdot \cos \alpha$$

and by combining it with (3-9) and assuming the relationship between the mixer voltage output v_{out} and the phase difference δ at the antenna elements is

$$v_{out}|_{LPF} = \frac{V^2}{2} \cdot \cos \delta. \quad (3-13)$$

A plot of the last expression for $d = \frac{\lambda}{2}$ is shown in Figure 3.5.

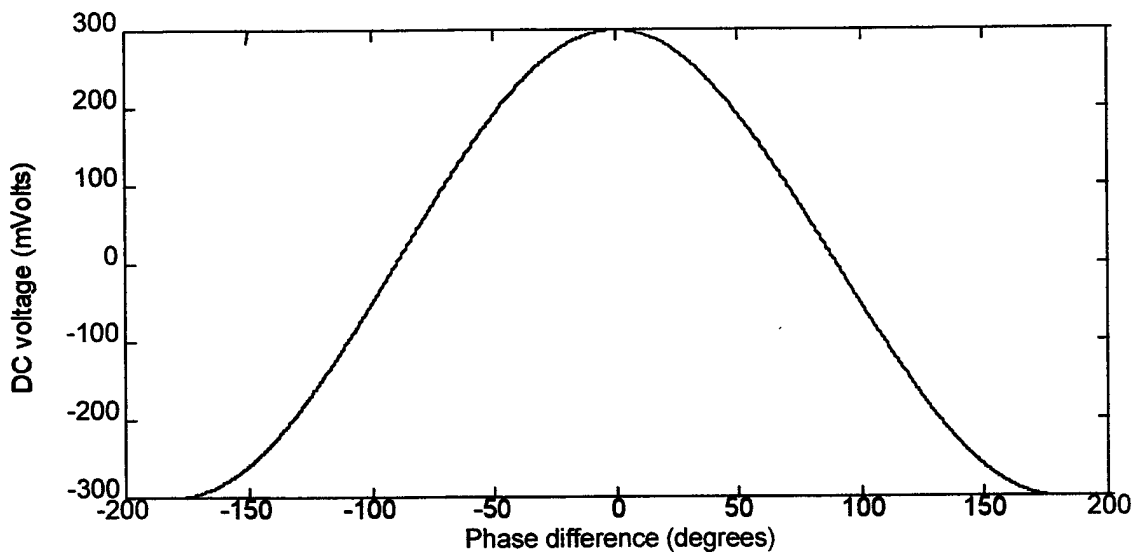


Figure 3.5: Phase difference at the elements vs mixer output voltage for $d = \frac{\lambda}{2}$.

For every voltage value there are two possible phase differences: ϕ and $-\phi$. Since, from

equation (3-7), $\delta = \frac{2\pi}{\lambda} d \sin \phi$, equation (3-13) becomes

$$v_{out}|_{LPF} = \frac{V^2}{2} \cdot \cos\left(\frac{2\pi}{\lambda} d \sin \phi\right), \quad (3-14)$$

which represents the relationship between the mixer voltage output v_{out} and the angle of incidence ϕ of the electromagnetic wave. The angle of incidence vs mixer output voltage for $d = \lambda/2$ is shown in Figure 3.6, and is a direct combination of the curves in Figures 3.4 and 3.5.

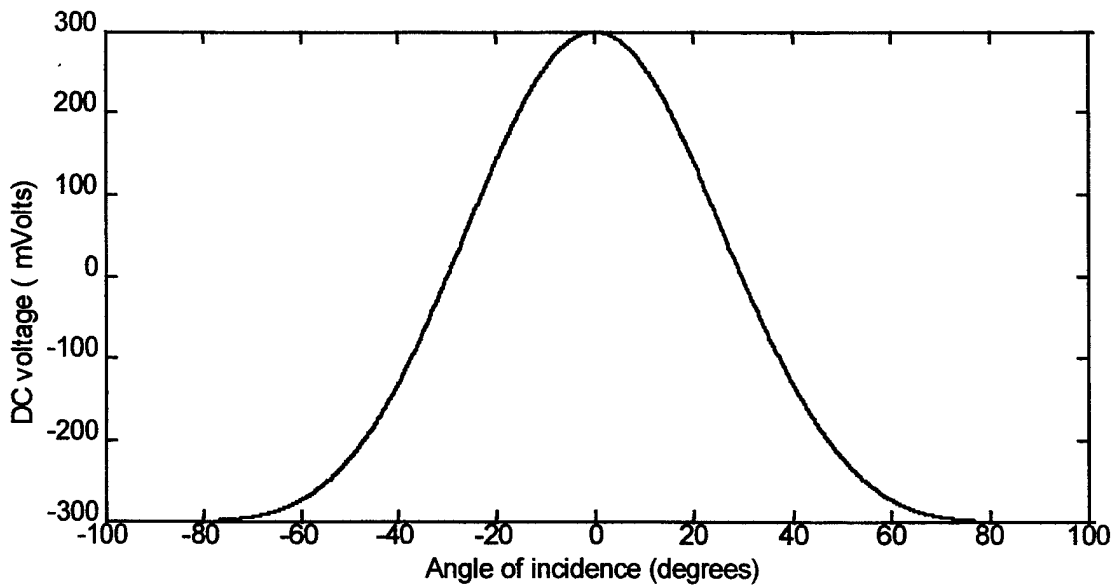


Figure 3.6: Angle of incidence vs mixer output voltage for $d = \frac{\lambda}{2}$.

From equation (3-14), the expression for the angle of incidence ϕ is given by

$$\phi = \sin^{-1} \left\{ \frac{\lambda}{2\pi d} \cos^{-1} \left(\frac{2V_{out}|_{LPF}}{V^2} \right) \right\}. \quad (3-14a)$$

For every value of voltage we have only two possible values of angle of incidence. This ambiguity can be eliminated by using a second array with a baseline that is not an integer multiple of the first.

If the baselines are greater than one half the wavelength, additional ambiguities exist, since the phase difference takes on multiple values outside of the interval $-\pi$ to π . The rapid change in voltage with phase difference allows higher resolution AOA estimates. The tradeoff is that the voltage is highly ambiguous. The number of periods n that occur when an emitter is swept from $-90^\circ \leq \theta \leq 90^\circ$ increases with the distance between the elements as

$$n = \frac{2d}{\lambda}. \quad (3-15)$$

Figure 3.7 shows this result and illustrates that the voltage period is not constant when plotted as a function of angle. The period increases with the increase of DOA from the array broadside ($\phi = 0^\circ$), because of the $\sin\phi$ dependence in Equation (3-7).

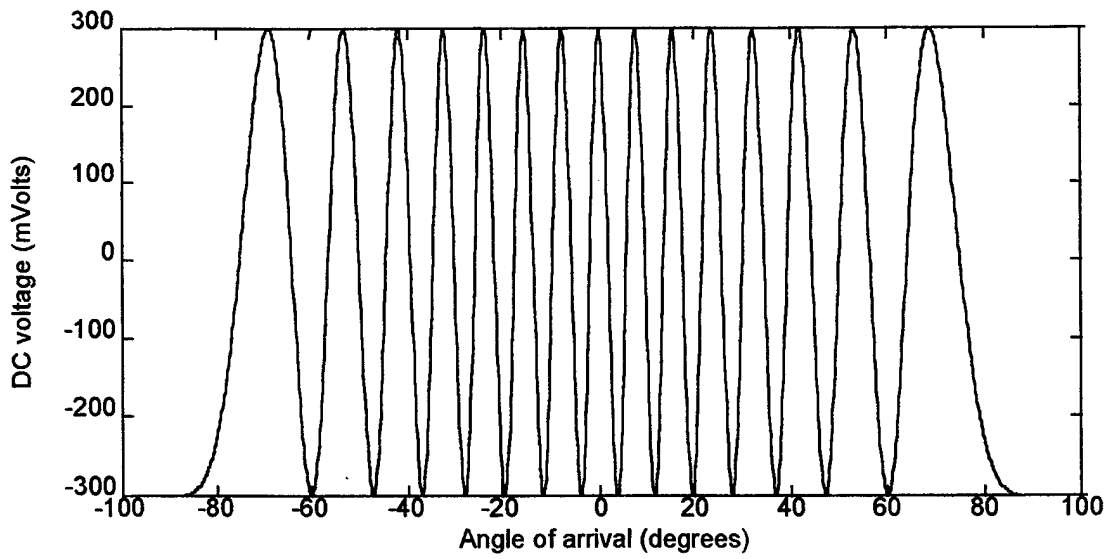


Figure 3.7: Angle of arrival vs mixer output voltage for $d = 7.5\lambda$.

The sinusoidal output voltage, shown in Figure 3.7, is a symmetrical folding waveform. In the next section, an encoding scheme, the Optimum Symmetrical Number System (OSNS), is presented that can resolve the angle of arrival ambiguities exactly.

IV. OPTIMUM SYMMETRICAL NUMBER SYSTEM (OSNS)

A. OSNS PREPROCESSING

The optimum SNS encoding scheme is composed of a number of pairwise relatively prime (PRP) moduli m_i . The integers within each SNS modulus are representative of a symmetrically folded waveform simulation to those shown in Figure 3.7 with the period of the waveform equal to twice the PRP modulus, i.e., $2m_i$ [Ref. 6]. For m given, the row vector gives the integer values within twice the individual modulus

$$\bar{x}_m = [0, 1, \dots, m-1, m-1, \dots, 1, 0]. \quad (4-1)$$

From this expression, the required number of comparators, or the required number of threshold levels for each channel to sample the phase waveforms is $m_i - 1$.

Due to the presence of ambiguities, the integers within the vector do not form a complete system of length $2m$ by themselves. The ambiguities that arise within the modulus are resolved by considering the paired values from all channels together. If N channels (pairs of elements or the number of PRP moduli) are used, the Dynamic Range (the number of spatial quantization cells) of this scheme is [Ref. 6,7]

$$M = \prod_{i=1}^N m_i. \quad (4-2)$$

This dynamic range is also the position of the first repetitive moduli vector. For the example of $m_1 = 3$, $m_2 = 4$, and $m_3 = 5$ the first repetitive moduli vector occurs at an input equal to 60, and the number of quantization levels without ambiguities is also 60 (0 to 59).

Table 4.1 illustrates the possible comparator states (number of comparators on) that a sampled phase waveform produces for the OSNS moduli set (3,4,5). That is, the integers within each column represent the number of comparators on due to the phase voltage exceeding the comparator matching threshold voltage. If they are viewed as sets of integers, the first 60 of them are unambiguous. That is, no set appears twice for a normalized input in the range [0,59].

Normalized Input	Moduli		
	$m_1 = 3$	$m_2 = 4$	$m_3 = 5$
0	0	0	0
1	1	1	1
2	2	2	2
3	2	3	3
4	1	3	4
5	0	2	4
6	0	1	3
7	1	0	2
8	2	0	1
9	2	1	0
10	1	2	0
11	0	3	1
.	.	.	.
.	.	.	.
.	.	.	.
56	2	0	3
57	2	1	2
58	1	2	1
59	0	3	0

Table 4.1. Quantization of OSNS waveforms using moduli set $m_1=3$, $m_2=4$, and $m_3=5$.

Figure 4.1 shows part of the optimum SNS folding waveforms and the comparator states for $m_1=3$, $m_2=4$, and $m_3=5$.

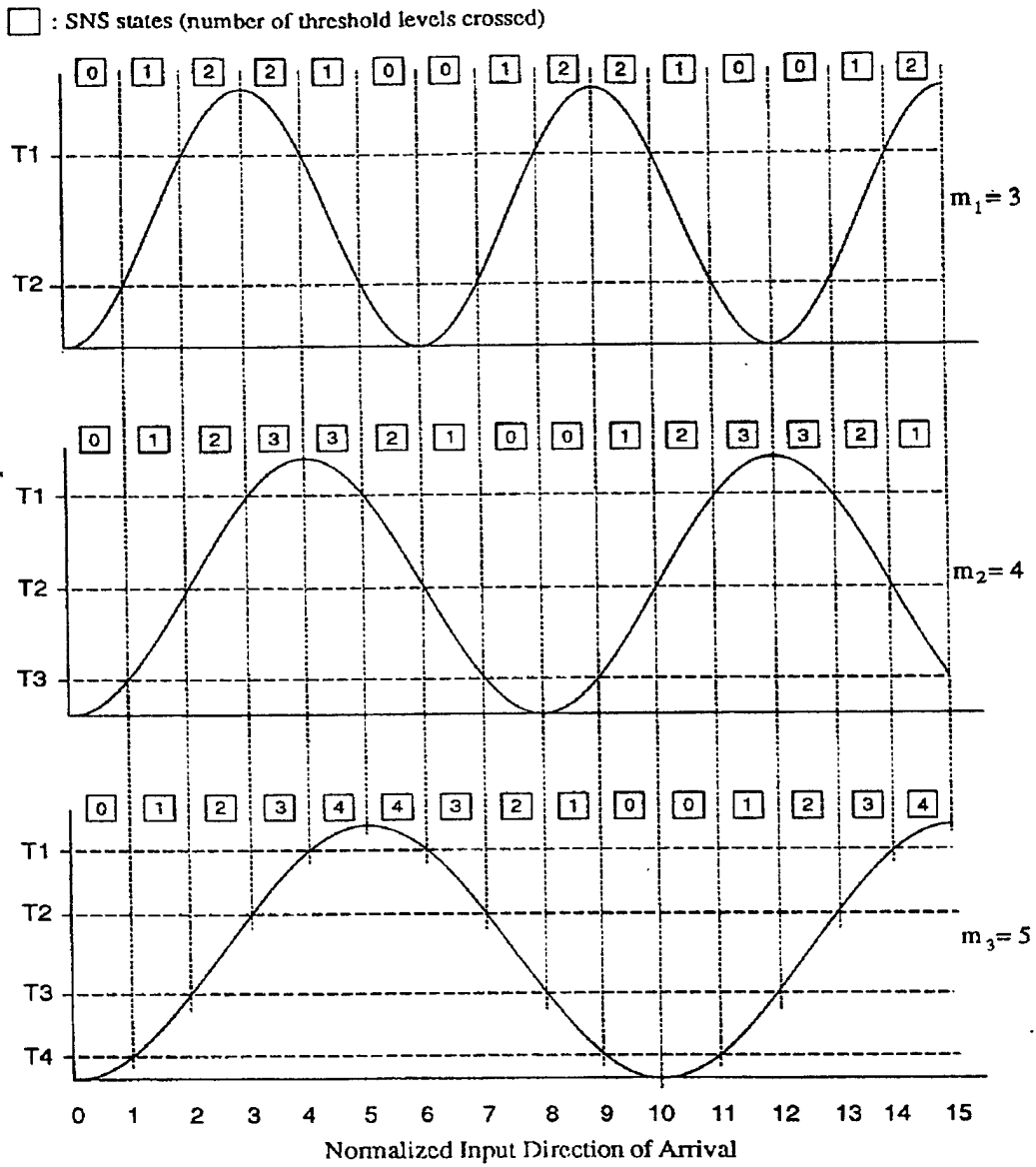


Figure 4.1: OSNS folding waveforms and output codes

for $m_1=3$ and $m_2=4$, and $m_3=5$ [Ref. 12].

The horizontal axis represents the normalized input voltage. The “T” values along the vertical axis represent predetermined comparator threshold voltage levels (reference levels). The numbers in squares at the top of the figure represent the number of comparators that are turned on for the given input voltage. For the $m = 4$ channel, we observe from the figure that as the normalized input voltage increases from 0 to 4 volts, the folded output swings from its minimum to its maximum value, or half of a complete fold. The period of one complete fold is equal to twice the modulus, or 8 volts. The output of the $m=3$, or $m= 5$ channel obey the same relationship.

B. OSNS ANTENNA ARCHITECTURE

The ambiguity problem observed in Figure 3.7 can be eliminated by the simultaneous use of more than one pair of antenna elements with differing baselines of several wavelengths with each pair forming a separate receive channel. Figure 4.2 shows a schematic representation of the OSNS antenna architecture for instantaneous direction finding. The array consists of four elements, three (3) channels. All of the channels can share a common element. Element 1 is combined with elements 2, 3, and 4. The three pairs of elements (1, 4), (1, 3), and (1, 2) form a three-baseline modular interferometer array with $m_1 = 3$, $m_2 = 4$, and $m_3 = 5$.

The distance between each pair of elements must be determined in order to obtain the correct number of folds needed to cover the entire field of view (from -90° to 90°) for the chosen moduli set. The distance between each pair of elements must be derived as a

function of the PRP modulus, m_i , so that the corresponding phase response has the correct number of folds.

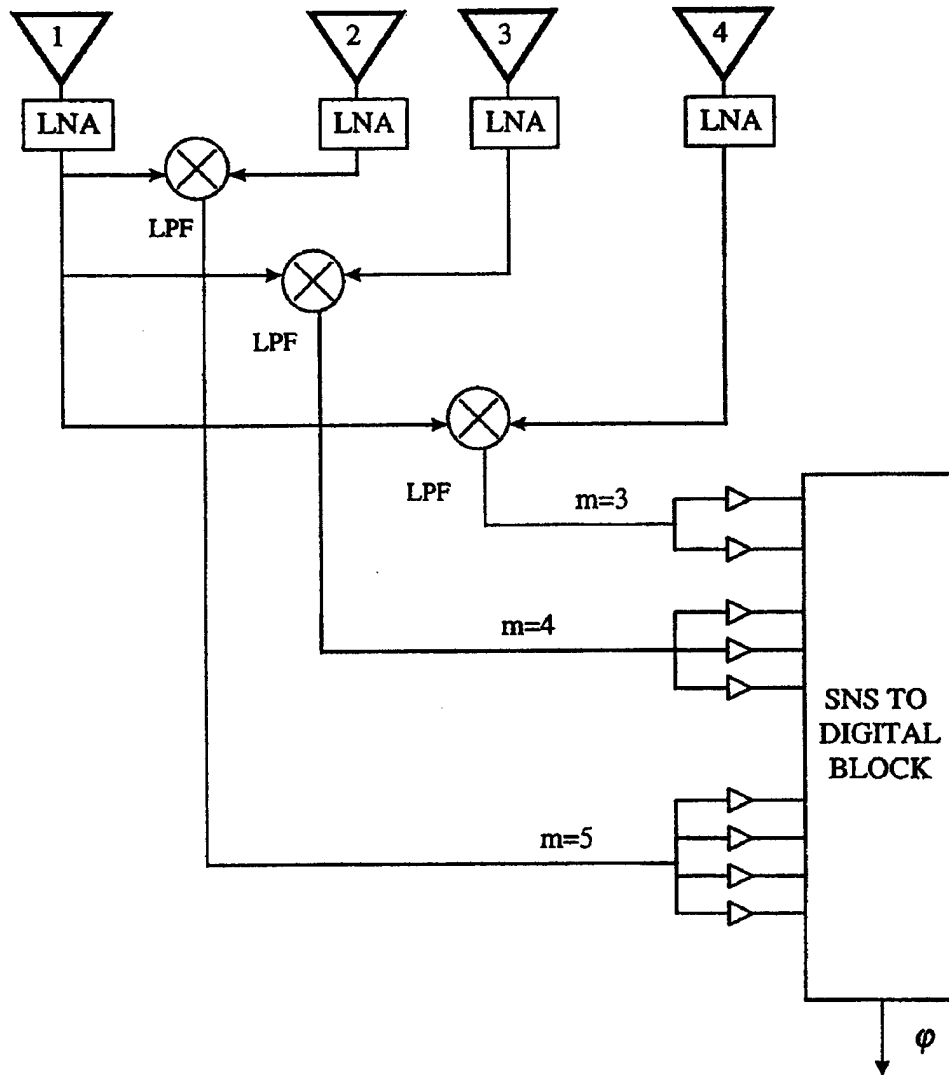


Figure 4.2: Schematic representation of the OSNS antenna architecture for instantaneous direction finding.

To derive the correct distance between the elements we consider the number of folds needed to cover the Dynamic Range, for a given modulus m_i , $n_i = \frac{M}{2m_i}$, and the normalized array factor from (2-34)

$$(AF)_{normalized} = \frac{1}{N} \left[\frac{\sin\left(\frac{N}{2}\psi\right)}{\sin\left(\frac{1}{2}\psi\right)} \right]$$

The normalized array factor, for a two element interferometer ($N=2$), becomes

$$(AF)_{normalized} = \frac{1}{2} \left[\frac{\sin(\psi)}{\sin\left(\frac{\psi}{2}\right)} \right] \quad (4-3)$$

Using the trigonometric identity $\sin(2\psi) = 2 \sin \psi \cos \psi$, the normalized array factor becomes

$$(AF)_{normalized} = \frac{\sin(\psi / 2) \cos(\psi / 2)}{\sin(\psi / 2)},$$

and finally

$$(AF)_{normalized} = \cos(\psi / 2) \quad (4-4)$$

The argument $\frac{\psi}{2} = \frac{1}{2}kd \sin \phi = \frac{\pi}{\lambda}d \sin \phi$, for different values of ϕ , becomes

$$\left. \frac{\psi}{2} \right|_{\phi=0^\circ} = 0 \quad (4-5a)$$

$$\left. \frac{\psi}{2} \right|_{\phi=90^\circ} = \frac{\pi d}{\lambda} \quad (4-5b)$$

$$\left. \frac{\psi}{2} \right|_{\phi=-90^\circ} = -\frac{\pi d}{\lambda}. \quad (4-5c)$$

That is, each fold of the array factor corresponds to a change in phase of π , for the new design theory, which implies

$$\left. \frac{\psi}{2} \right|_{90^\circ} - \left. \frac{\psi}{2} \right|_{-90^\circ} = \pi$$

and

$$\left(\frac{\pi d}{\lambda} \right) - \left(-\frac{\pi d}{\lambda} \right) = \pi \Rightarrow \frac{2\pi d}{\lambda} = \pi$$

and finally

$$d = \frac{\lambda}{2}. \quad (4-6)$$

Therefore, the required spacing between the reference element and the respective element of channel i is given by

$$d_i = n_i \frac{\lambda}{2} = \left(\frac{M}{2m_i} \right) \frac{\lambda}{2}. \quad (4-7)$$

For the example with moduli $m_1=3$, $m_2=4$, and $m_3=5$, assuming a center frequency

$$f_o=8.5GHz, \text{ with DR of } M = \prod_{i=1}^N m_i = m_1 \cdot m_2 \cdot m_3 = 3 \cdot 4 \cdot 5 = 60,$$

the inter element spacings are

$$d_1 = n_1 \frac{\lambda}{2} = \left(\frac{M}{2m_1} \right) \frac{\lambda}{2} = 5\lambda = \left(\frac{60}{2 \cdot 3} \right) (1.765cm) = 17.65cm \quad (m_1=3)$$

$$d_2 = n_2 \frac{\lambda}{2} = \left(\frac{M}{2m_2} \right) \frac{\lambda}{2} = 3.75\lambda = 13.24cm \quad (m_2=4)$$

$$d_3 = n_3 \frac{\lambda}{2} = \left(\frac{M}{2m_3} \right) \frac{\lambda}{2} = 3\lambda = 10.59cm \quad (m_3=5).$$

The spatial resolution near boresight is given by

$$r = \frac{FOV}{M} \quad (4-8)$$

where FOV is the field of view determined by the receiving element pattern. Ideally the FOV can be 180° . In this example ($r=3^\circ$) we note that the spatial resolution is not uniform over the range of $-\pi$ to π , i.e. it increases with angle off boresight ($\theta = 0^\circ$),

because of the $\sin\phi$ dependence. Resolution is a tradeoff between number of element pairs (moduli) and number of quantization levels (comparators).

The number of folding periods within the DR is given by the following equation

$$n_i = \frac{M}{2m_i}.$$

For this example, the number of folds for each channel is given by

$$n_1 = \frac{M}{2m_1} = \frac{60}{2 \cdot 3} = 10$$

$$n_2 = \frac{M}{2m_2} = \frac{60}{2 \cdot 4} = 7.5$$

$$n_3 = \frac{M}{2m_3} = \frac{60}{2 \cdot 5} = 6.$$

With the correct distances between elements, the amplitude response from each channel is quantized using m_i-1 comparators. The function of the comparators is to generate the integers within each modulus by quantizing the amplitude response according to the modulus m_i with which it is associated.

In some applications element placement at certain locations on a platform may be prohibited, in which case an alternate OSNS design could be used to provide the same

unambiguous DOA resolution, using e.g., a different number of comparators, as shown in Table 4.2.

When the channels are recombined the result is a high accuracy unambiguous estimate of the DOA. In the next section the ability of the comparators to amplitude analyze the phase response is considered in more detail.

OSNS Moduli	Element Spacings	Comparators Required
$m_1 = 3, m_2 = 20$	$d_1 = 5\lambda, d_2 = 0.75\lambda$	21
$m_1 = 4, m_2 = 15$	$d_1 = 3.75\lambda, d_2 = 1\lambda$	17
$m_1 = 5, m_2 = 12$	$d_1 = 3\lambda, d_2 = 1.25\lambda$	15
$m_1 = 3, m_2 = 4, m_3 = 5$	$d_1 = 5\lambda, d_2 = 3.75\lambda, d_3 = 3\lambda$	9

Table 4.2: Several OSNS arrays having the same Spatial Resolution ($M = 60$).

V. ANALOG TO DIGITAL CONVERSION (ADC)

The process of converting a continuous-time (analog) signal to a digital sequence that can be processed by a digital system requires that we quantize the sampled values to a finite number of levels and represent each level by a number of bits. The electronic device that performs this conversion from an analog signal to a digital sequence is called an *analog-to-digital (A/D) converter* (ADC) [Ref. 13]. Figure 5.1 shows a block diagram of the basic elements of an A/D converter.

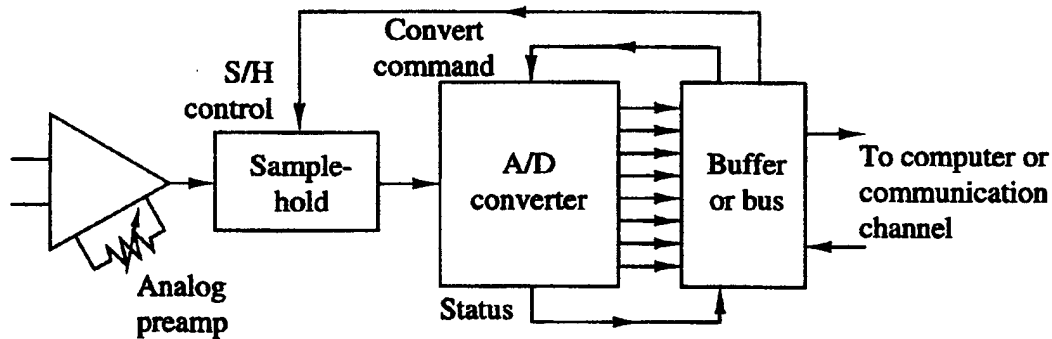


Figure 5.1: Block diagram of the basic elements of an A/D converter [Ref. 13].

In order to quantize an input signal at a certain instant of time, the signal should be held constant at that instant. If the input signal changes rapidly and the digitizing process is slow, the accuracy of the output data will be poor.

One approach is to place a sample-and-hold (S/H) circuit in front of the quantizer. The held signal is then quantized and converted to digital form. Usually, the S/H is

integrated into the A/D converter. The S/H is a digitally controlled analog circuit that can create a very narrow aperture window, which will take the input at the desired instant and keep the voltage constant for a relatively long period of time, such that the digitizing circuit can operate properly.

Figure 5.2 shows the time-domain response of an ideal S/H circuit (i.e., a S/H that responds instantaneously and accurately). It is apparent that the S/H tracks the analog input signal during the sample mode, and then holds it fixed during the hold mode to the instantaneous value of the signal at the time the system is switched from the sample mode to the hold mode.

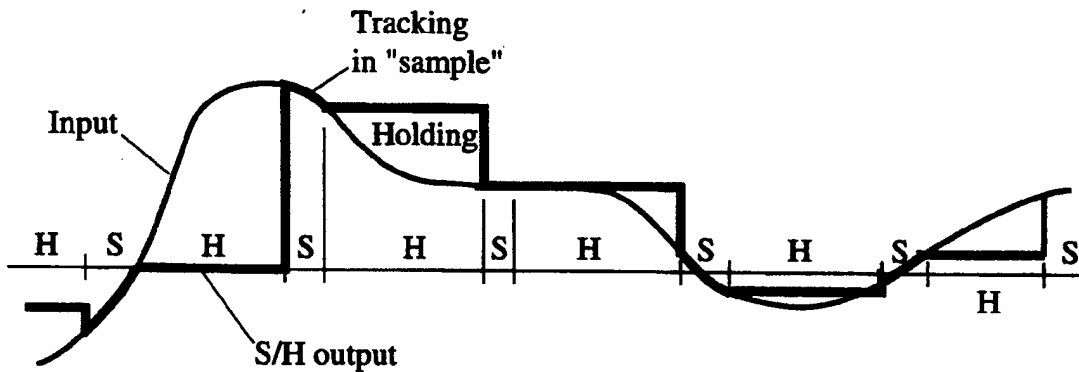


Figure 5.2: Time-domain response of an ideal S/H circuit [Ref. 13].

The goal of the S/H is to continuously sample the input signal and then to hold that value constant as long as it takes for the A/D converter to obtain its digital representation. The use of an S/H allows the A/D converter to operate more slowly compared to the time

actually used to acquire the sample. In the absence of a S/H, the input signal must not change by more than one-half (1/2) of the quantization step during the conversion, which may be an impractical constraint. Consequently, the S/H is crucial in high-resolution (12 bits per sample or higher) digital conversion of signals that have large bandwidths (i.e., they change very rapidly). An ideal S/H introduces no distortion in the conversion process and is accurately modeled as an ideal sampler. However, time-related degradations such as errors in the periodicity of the sampling process (“jitter”), nonlinear variations in the duration of the sampling aperture, and changes in the voltage held during conversion do occur in practical devices. [Ref. 13]

The A/D converter begins the conversion after it receives a convert command. The time required to complete the conversion should be less than the duration of the hold mode of the S/H. Furthermore, the sampling period T should be larger than the duration of the sample mode and the hold mode.

The basic task of the A/D converter is to convert a continuous range of input amplitudes into discrete output levels, which can be represented by a set of digital (binary) code words. This conversion involves the process of *quantization* and *coding*. Quantization is a nonlinear and noninvertible process that maps a given amplitude $x(n)=x(nT)$ at time $t=nT$ into an amplitude x_k , taken from a finite set of values. The procedure is shown in Figure 5.3, where the signal amplitude range is divided into L intervals

$$I_k = \{x_k < x(n) \leq x_{k+1}\} \quad k = 1, 2, \dots, L \quad (5-1)$$

by the $L+1$ decision levels $x_1, x_2, x_L, \dots, x_{L+1}$. The possible outputs of the quantizer (quantization levels) are denoted as $\hat{x}_1, \hat{x}_2, \dots, \hat{x}_L$. [Ref. 13]

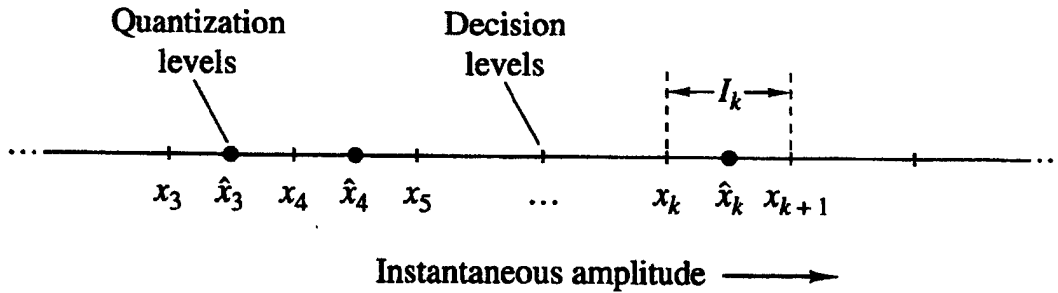


Figure 5.3: Quantization Process [Ref. 13].

In most digital signal processing operations the mapping is independent of n . Furthermore, in signal processing we often use *uniform* or *linear quantizers* defined by

$$\hat{x}_{k+1} - \hat{x}_k = \Delta \quad k = 1, 2, \dots, L-1 \quad (5-2a)$$

$$x_{k+1} - x_k = \Delta \quad \text{for finite } x_k, x_{k+1} \quad (5-2b)$$

where Δ is the *quantizer step size*. Uniform quantization is usually a requirement if the resulting signal is to be processed by a digital system. [Ref. 13]

Figure 5.4 shows the transfer characteristic of an ideal ADC. If the input increases linearly with respect to time, the output and the quantization error are as shown in this Figure. It is obvious that the quantization process is a nonlinear one, making it difficult to

analyze mathematically. In a practical ADC, it is also difficult to make the quantization level uniform; thus the quantization error is worse than in the ideal case.

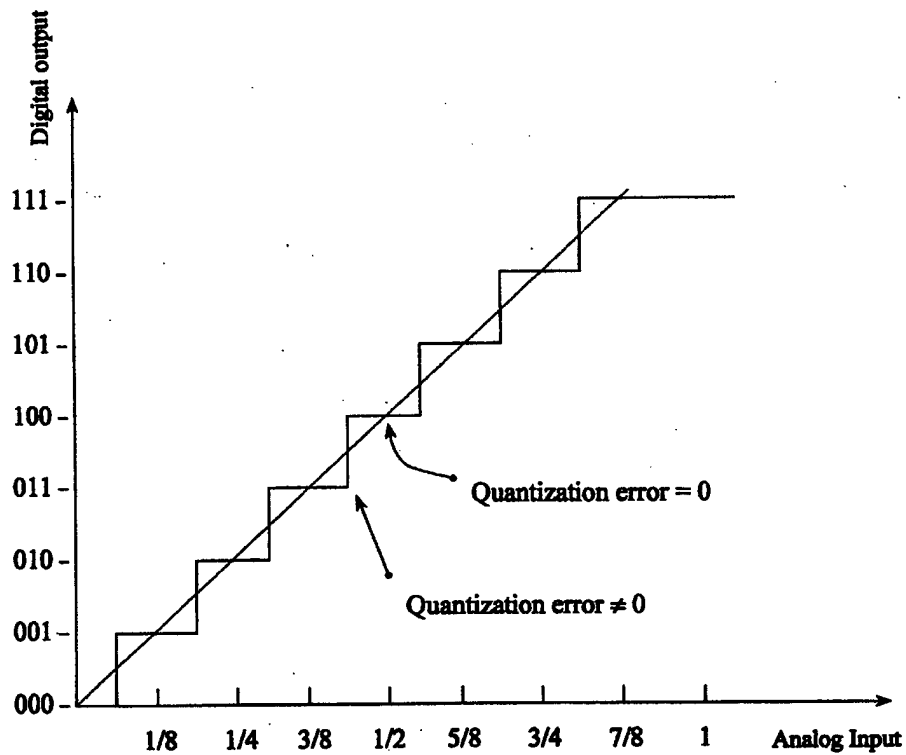


Figure 5.4: Transfer characteristic of an ideal ADC.

The *coding* process in an A/D converter assigns a unique binary number to each quantization level. If we have L levels, we need at least L different binary numbers. With a word length of $b+1$ bits we can represent 2^{b+1} distinct binary numbers. Hence we should have $2^{b+1} \geq L$ or, equivalently, $b+1 \geq \log_2 L$.

The maximum signal to an ADC is often defined as a sine wave with amplitude that matches the highest level of the ADC. The maximum level is often used to determine the upper limit of the Dynamic Range. If there is no noise and the input voltage matches the maximum range of the ADC, the voltage V_{max} is [Ref. 14]

$$2V_{max} = 2^b Q \quad \text{or} \quad V_{max} = 2^{b-1} Q \quad (5-3)$$

where Q is the voltage per quantization level. This equation shows that the sine wave reaches the top of the highest as well as the bottom of the lowest quantization levels.

A sine wave with amplitude matching this maximum voltage has a power [Ref. 14]

$$P_{max} = \frac{V_{max}^2}{2} = \frac{2^{2b} Q^2}{8} \quad (5-4)$$

Also, if there is no noise, the minimum signal is considered as the voltage that can cause in the LSB. Otherwise, the ADC cannot detect the signal. Under this condition, the minimum voltage V_{min} is equal to one quantization level, or

$$2V_{min} = Q \quad (5-5)$$

The corresponding power level is

$$P_{\min} = \frac{V_{\min}^2}{2} = \frac{Q^2}{8}. \quad (5-6)$$

The Dynamic Range can be defined as the ratio of P_{\max} to P_{\min} , which can be written as

$$DR = \frac{P_{\max}}{P_{\min}} = 2^{2b} \quad (5-7)$$

which is often expressed in logarithmic form as

$$DR = 10 \log \left(\frac{P_{\max}}{P_{\min}} \right) = 20b \log(2) \approx 6bdB. \quad (5-8)$$

This is the reason that the dynamic range of an ADC is often referred to as 6dB/bit.

[Ref.13]

Practical A/D converters differ from ideal converters in several ways. Various degradations are usually encountered in practice. Practical A/D converters may have *offset* error (the first transition may not occur at exactly $+\frac{1}{2} LSB$), *scale-factor* (or gain) error slope not equal to one, and differential *linearity* error (the differences between transition values are not all equal or uniformly changing). If the *differential linearity* error is large enough, it is possible for one or more words to be missed. In the next section the design and fabrication of a prototype array in hardware is described.

VI. DESIGN AND FABRICATION

A. ARRAY ANTENNA

In this chapter we'll discuss the design procedure that must be followed in order to transfer from the abstract antenna theory to the practical and tangible reality. In order to do that, we are going to use the results of the derivations from previous analysis and apply them to the given data.

To start, the first step is to design the array antenna. The design of the array is a trade off among the desired angular resolution for the DOA, the number of comparators that is going to be used for digitizing the phase signal, and the physical size of the ground plane of the array (for several applications).

Figure 6.1 illustrates the block diagram of the prototype two-channel DF array beamforming network and signal processor. This figure illustrates the various parts of the entire OSNS DF antenna architecture. The components used for constructing each channel of the antenna part of the DF architecture are listed as follows

- Ground plane
- Waveguides
- Low Noise Amplifiers (LNA)
- Power splitter
- Phase adjuster
- Attenuator
- SMA mode barrel adapters

- Rigid coax cable
- SMA rigid coax connectors
- Mixer

1. Design of the Array and Ground Plane

The array consists of three antenna elements and two open-ended waveguides (dummy load). By combining these elements we form two separate two-element arrays that sample the incident wavefront and mix the signals from the two branches. An array based on the moduli $m_1 = 6$ and $m_2 = 11$ was designed, fabricated and tested at a frequency 8.5 GHz. The first antenna element plays the role of the reference, and is shared by all elements to form the two separate interferometers (channels). The dynamic range of the moduli is $M=66$, and the possible values that a folding phase waveform produces at the output of the comparator ladder for each interferometer is shown in the Table 6.1 (folding period $2m_i$).

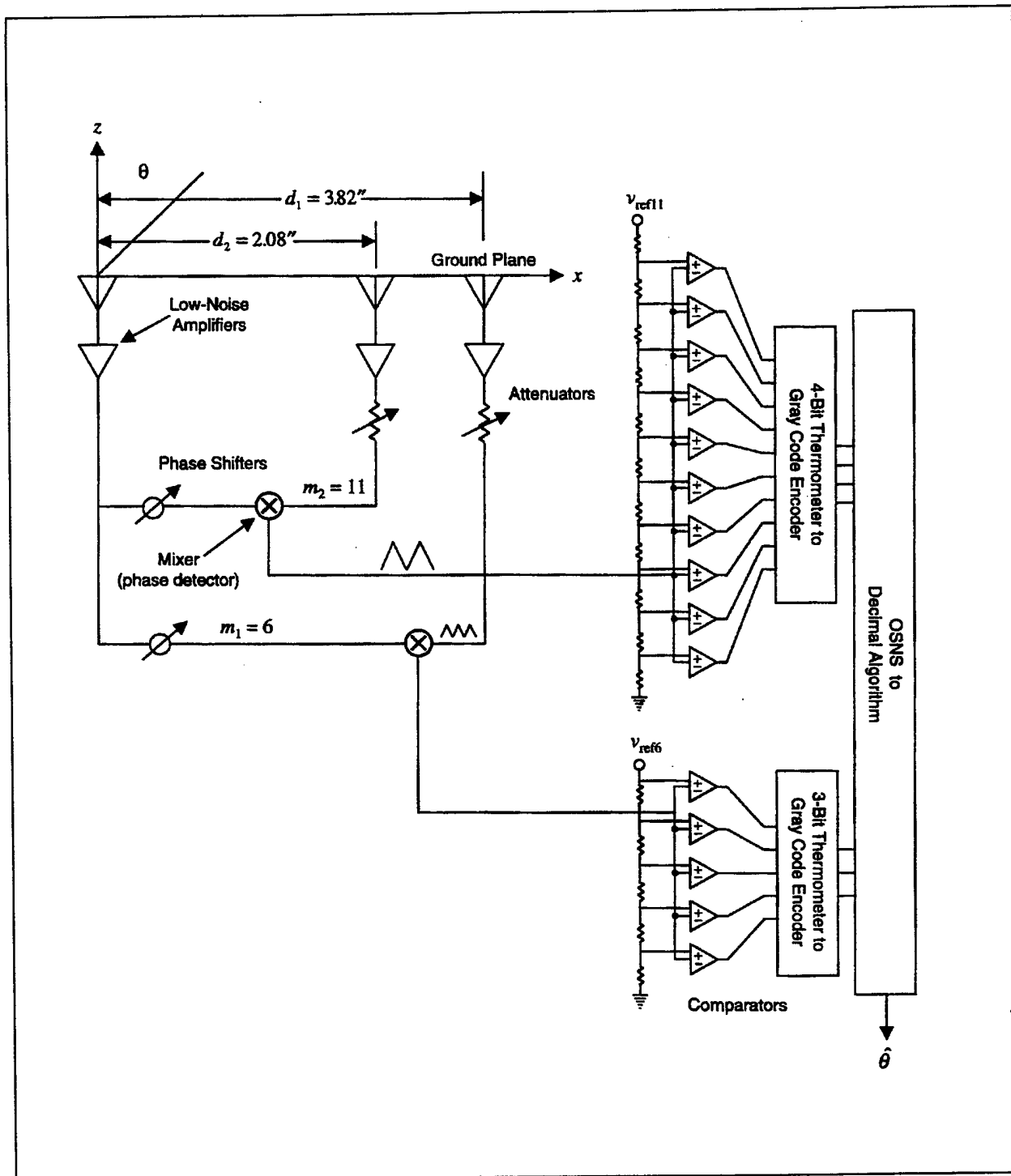


Figure 6.1: Block diagram of the OSNS phase-sampled DF array antenna based on the moduli $m_1 = 6$ and $m_2 = 11$.

<i>Normalized Input</i>	<i>mod 11</i>	<i>mod 6</i>
	11 digits 10 reference levels	6 digits 5 reference levels
0	0	0
1	1	1
2	2	2
3	3	3
4	4	4
5	5	5
6	6	5
7	7	4
8	8	3
9	9	2
10	10	1
11	10	0
12	9	0
13	8	1
14	7	2
15	6	3
16	5	4
17	4	5
18	3	5
19	2	4
20	1	3
21	0	2
22	0	1
23	1	0
24	2	0
25	3	1
26	4	2
27	5	3
28	6	4
29	7	5
30	8	5
31	9	4
32	10	3
33	10	2
34	9	1
35	8	0
36	7	0
37	6	1
38	5	2
39	4	3
40	3	4
41	2	5
42	1	5
43	0	4

44	0	3
45	1	2
46	2	1
47	3	0
48	4	0
49	5	1
50	6	2
51	7	3
52	8	4
53	9	5
54	10	5
55	10	4
56	9	3
57	8	2
58	7	1
59	6	0
60	5	0
61	4	1
62	3	2
63	2	3
64	1	4
65	0	5
66	0	5

Ambiguity

Table 6.1. OSNS Dynamic Range using moduli set $m_1 = 6$ and $m_2 = 11$.

$$(M = 66)$$

If within the dynamic range covers 180 degrees, then each table entry corresponds to a 2.72 degrees interval.

In this prototype design, the first task in designing the array is to calculate the individual distances between the element pairs. The required spacing between the reference element and the second element of each channel, for the unambiguous DOA estimates, is given by

$$d_i = n_i \frac{\lambda}{2} = \frac{M \lambda}{2m_i} = \frac{M}{4m_i} \lambda \quad (6-1)$$

which for moduli $m_1 = 6$ and $m_2 = 11$ are

$$d_1 = n_1 \frac{\lambda}{2} = \frac{M \lambda}{2m_1} = \frac{66 \lambda}{2 \cdot 6} = 2.75\lambda = 3.82in$$

$$d_2 = n_2 \frac{\lambda}{2} = \frac{M \lambda}{2m_2} = \frac{66 \lambda}{2 \cdot 11} = 0.75\lambda = 2.08in.$$

Figure 6.2 shows a schematic diagram of the ground plane of the array, giving the distances and the aperture sizes in detail. Within the dynamic range, the number of folding periods is given by

$$n_i = \frac{M}{2m_i} \quad (6-2)$$

and for each modulus

$$n_1 = \frac{M}{2m_1} = \frac{66}{2 \cdot 6} = \frac{11}{2} = 5.5$$

$$n_2 = \frac{M}{2m_2} = \frac{66}{2 \cdot 11} = \frac{6}{2} = 3.$$

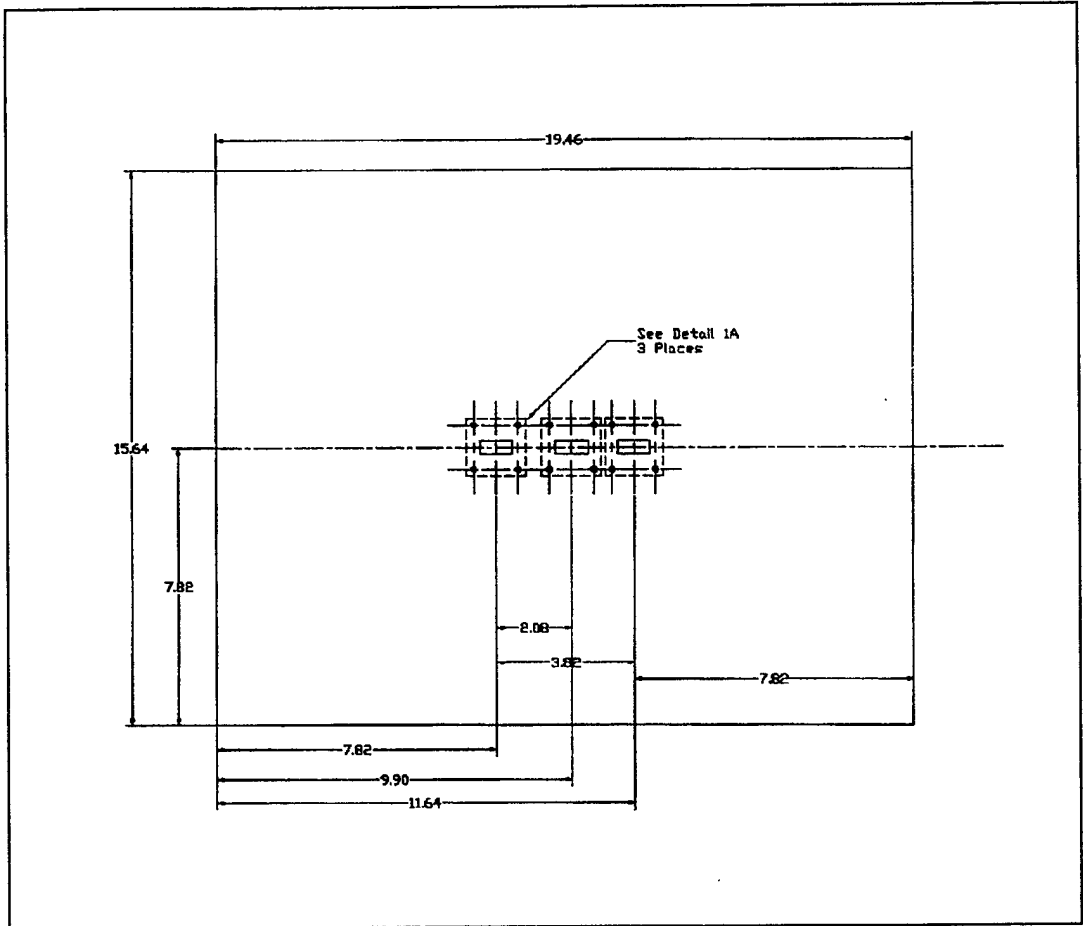


Figure 6.2: Directional Finding Array Antenna Ground Plane Cutout.

Figure 6.3 illustrates the physical dimensions of the rectangular aperture.

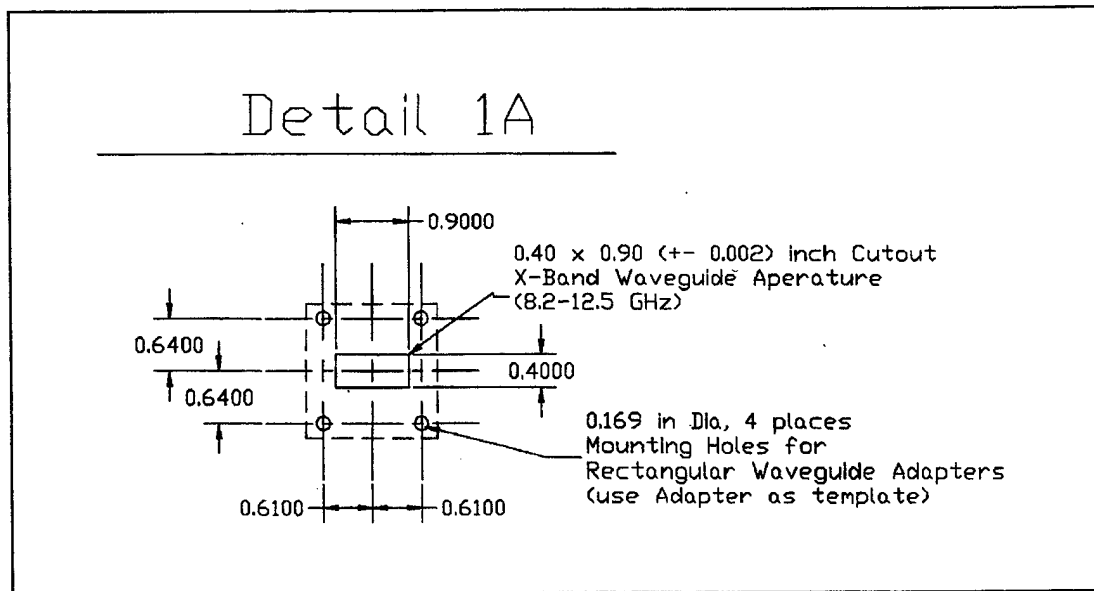


Figure 6.3: Rectangular aperture antenna element.

The rectangular aperture antenna elements are open-ended waveguides. Open-ended waveguides are commonly used as radiating or receiving elements in applications, like radar, where microwave power is present and where low losses are required. It is a hollow conducting “pipe” which propagates electromagnetic waves bounded by the walls of the guide. Waveguides can have many configurations. The most commonly used type in radars is TE_{10} rectangular guide, as in our case. It is the smallest possible guide for a given frequency. Its cross-section has two dimensions, universally called “a” (the longer dimension) and “b” (the shorter). The TE in its name stands for transverse electric, meaning that no component of the electric fields is in the direction of propagation. The lack of “M” in the name indicates that magnetic field components are found in the direction of

propagation. The subscript 10 indicates that in the "a" direction there is one half-wave of the electric field, and in the "b" there is no electric field variation. Figure 6.4 shows the cross-section of a TE₁₀ rectangular waveguide with the net electric fields. [Ref. 15]

Propagation through the waveguide is shown in Figure 6.5. Electric fields arrange themselves at an angle across the waveguide such that the waveguide in the dielectric (often air) is as shown in the figure. Propagation, at the velocity of the dielectric, is at right angles to the fields. Where the field touches the sidewall, it reflects as a field of the opposite polarity. The angles are a function of the frequency (wavelength). Part (a) of Figure 6.5 shows a lower frequency (longer wavelength) of each frequency band and part (b) shows a higher frequency. The waveguides that are used in our case cover the range of frequencies from 8.2 to 12.4 GHz, which is the X frequency Radar band. [Ref. 15]

Figure 6.5 also shows that the shortest wavelength, which can be supported, is where one-half wavelength in the dielectric is the "a" width of the waveguide. The wavelength in the waveguide (λ_g) is the distance between two positive nodes along the guide, where λ_d is the dielectric wavelength. [Ref. 15]

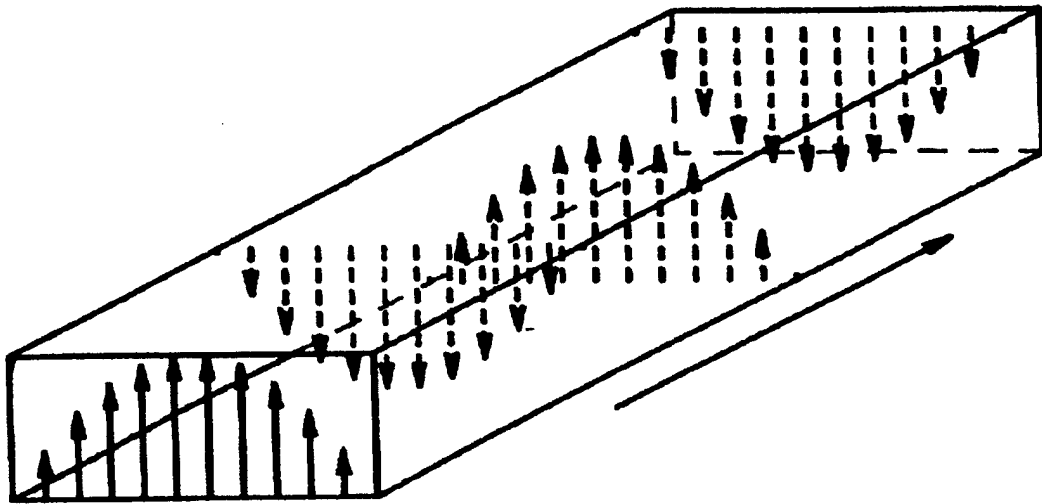
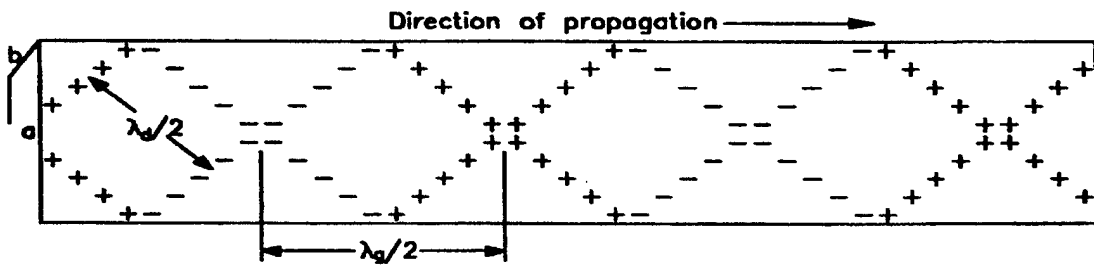
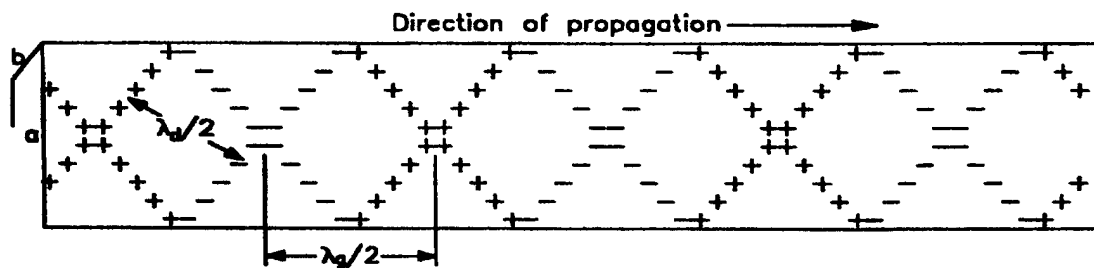


Figure 6.4: TE_{10} waveguide cross-section with net electric fields.



a. Lower frequency (longer wavelength)



b. Higher frequency (shorter wavelength)

Figure 6.5: TE_{10} propagation electric fields.

2. Low Noise Amplifiers (LNA)

The need for amplification arises because the incoming signal to the antenna elements is “weak” (microvolt (μV) range). Such signals are too small for reliable processing, and processing is much easier if the signal magnitude is made larger. The functional block that accomplishes this task is the signal amplifier. The type of amplifier we need is primary intended to operate on very small input signals. Its purpose is to make the signal magnitude larger and therefore is thought of as voltage amplifier.

There is another point we have to focus on. Beyond the voltage amplification, it is essential to receive an input signal giving the best possible signal-to-noise ratio (SNR). The antenna elements receive both signals and noise. Also, every component in each of the receiving channels produces thermal noise, where the worst of them are the mixers having a high noise figure F , where $F = \frac{SNR_{in}}{SNR_{out}}$. To provide an adequate amount of signal to noise, a low-noise amplifier (LNA) is included at the output of each interferometer element. A low noise amplifier is one having a low noise temperature. It usually has high gain, wide bandwidth, and a large dynamic range. Low noise amplifiers are used in a lot of applications (radar, DF antennas) to increase the signal level without introducing any significant noise. By increasing the signal power they improve the signal-to-noise ratio (SNR). In radar applications, low noise amplifiers are used as the first stage in receivers and are often mounted near the antenna feed. Another purpose of the low noise amplifiers (LNAs) is to boost the incident signal up to the operational range of the mixers.

It is appropriate at this point to discuss the need for linearity in low noise amplifiers. When amplifying a signal, care must be exercised so that the information contained in the signal is not changed and no new information is introduced. Thus when feeding a signal to an amplifier, we want the output signal of the amplifier to be an exact replica of that at the input, except of course for having larger magnitude. Any change in waveform is considered to be distortion and is obviously undesirable.

Low noise amplifiers can introduce signal distortions if the ratio of the power input to the power output is not linear. Also, the phase shift vs frequency can be different for every low noise amplifier. This differentiation from one amplifier to another and depends on its construction and has to be measured. The response of each individual amplifier and a cascade of them in pairs are important to be known for proper operation of the antenna.

The voltage level at the output of the mixer depends not only the phase difference between the two elements in each channel, but also on the maximum voltage level of the mixer's input signal. Without including the amplifiers between the antenna elements and the mixer, the maximum voltage level at the output of the mixer drops off with angle off boresight due to the EF. Sources at different angles create different voltage levels at the output of the mixer, even if they are at the same range. A solution to this problem is to insert a cascade of two LNAs, between the antenna elements and the mixer in each channel, operating in the saturation region. The amplifiers will operate in the saturation region so that the output power level remains constant for the expected variation in input signal.

The response of each individual amplifier, or the cascade of them in pairs, must be measured. In order to measure the response of the LNAs, a power generator, providing the input power to the low noise amplifiers (in dB) and two power meters, measuring the input and the output power of the LNA, were used. Attenuators were used to keep the input power between specific limits in order to get the desired results and prevent any damage to the LNAs and the power meters.

A problem that we faced was that two of the six amplifiers were much bigger than the other ones (i.e., the length of the coax cable had to be different in each channel). Also the DC supplying voltage was different (12V instead of 15V). For the measurements of the amplifier response the input power was increased and the output power recorded, either for each amplifier individually, and for the cascade of them in pairs. By recording the input and the output power and by using Matlab, we got the amplifiers responses, individually, as they appear in Figure 6.6. The individual transfer functions of the six amplifiers being used have a positive slope. These plots represent the input power vs the output power for the six LNAs. There is a slight difference in transfer function between the big amplifiers (001-002) and the smaller ones (450873 - 450874 - 450875 - 451376). The transfer function of each one has almost the same slope, but the difference between them is that the small amplifiers reach the saturation region faster than the bigger ones.

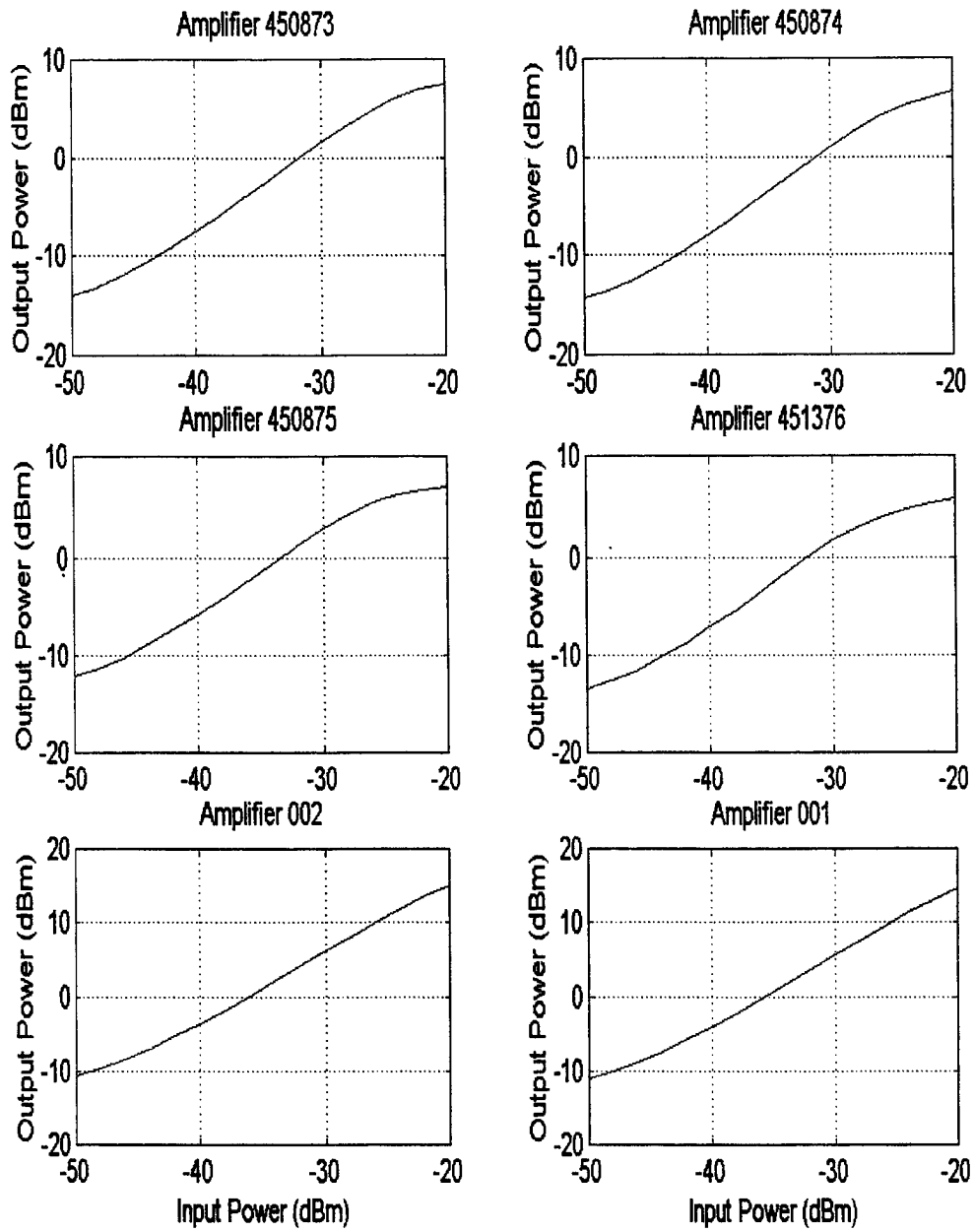


Figure 6.6: Transfer functions of the six low noise amplifiers.

To insure that the response remains constant over a large range of input power, a matched pair of amplifiers is cascaded together with a 30dB attenuator. In Figure 6.7, the transfer functions of the cascade of the low noise amplifiers, in pairs, are illustrated along with the individual transfer functions of them. We can see that they both, small and big ones, reach the saturation region very quickly (they actually are in the saturation region from the beginning) obtaining the desired flat response.

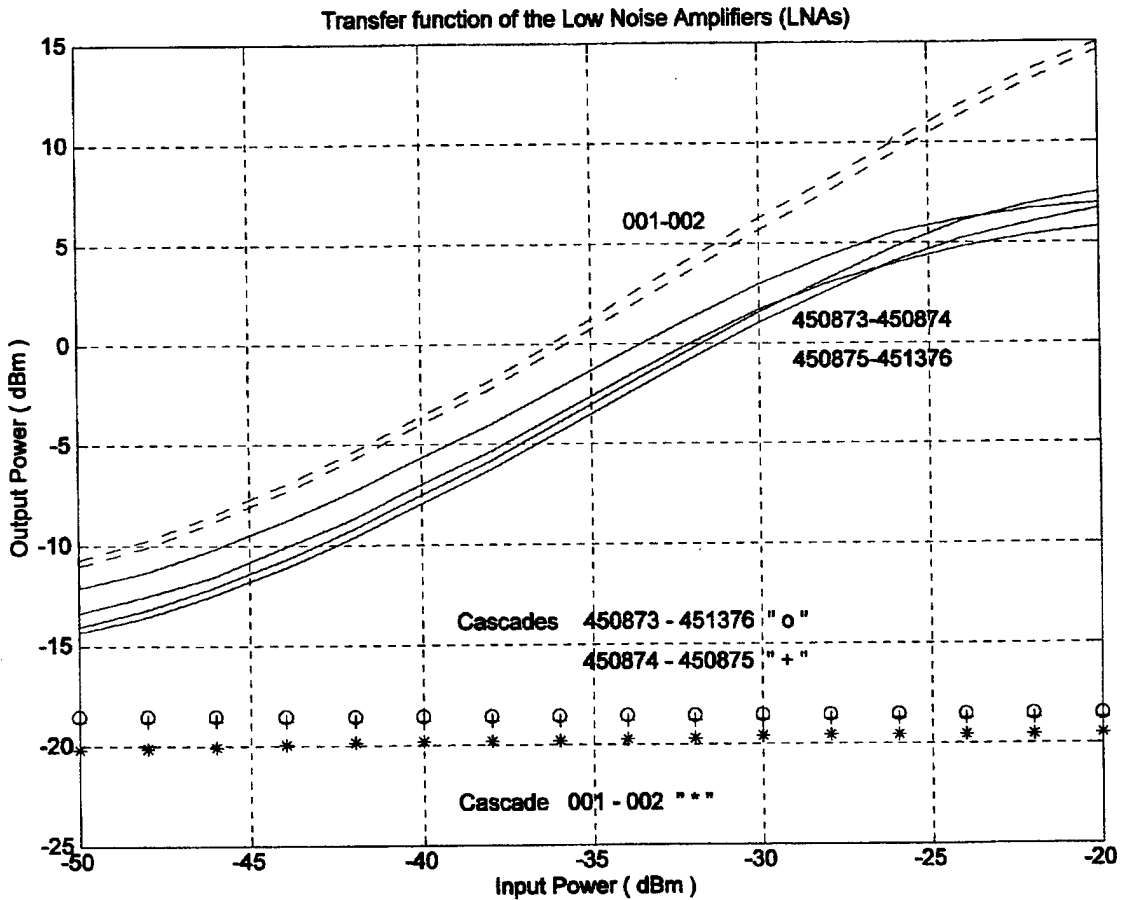


Figure 6.7: Transfer function of the six amplifiers (individually – in cascade).

3. Phase shift alignment

The output of the antenna elements, consisting a channel, differs in phase from each other in proportion to the extra time it takes a plane wave signal to travel the difference in distance between the two antenna elements. Since, the measurement of the phase difference can give the incoming angle with respect to boresight, the phase difference between the two branches in each channel has to be zero. In other words, it is very critical to use each branch component in such a manner as to give no difference in phase between the two different paths the incoming signal has to follow from the elements to the mixer.

The first factor that needs to be taken into account is that the common element has to be used by both of the channels. A power splitter is used to split the signal into two (2) paths. By inserting a power splitter into one of the branches of each channel, the power of the signal between these two paths will be different. The use of an attenuator, in the other branch of the same channel, reduces the power (equal power to the mixer).

The phase shift, for each array spacing, is also determined by adjusting the cable lengths. The construction of the cables is important in the development of the direction finder, which uses the phase delay method to determine DOA. Since direction is calculated from phase difference, variations in phase from the ideal introduce AOA errors. Cable length is a critical parameter especially for signals at 8.5 GHz, where the wavelength is 3.53 cm. Thus a moderate error in the length can affect the DOA estimate significantly. Other factors that also introduce phase shifts are the bends in the cable, the loose

connections, and the adapters. All of the phase variations between the array channels must be measured, and adjusted.

A fixed phase shifter is also included in one branch of each interferometer so that the symmetrically folded phase response waveforms from each mixer may be aligned. The alignment insures that the comparators in the digital processor properly sample the phase waveform and encode it in the OSNS.

An issue that needed to be taken care of was the alignment of the two-channel voltage outputs so that they have a minimum value at $\phi = -90^\circ$. This was the original thought, but since there was a nonlinearity in the voltage output between the channels at the edges ($\phi = -90^\circ$, $\phi = 90^\circ$) it was decided to align the two channel output voltage at another value (-50°). The importance of the alignment is shown in Table 6.1, where the digits must start at the values (0,0). We can control the location of the voltage minima by introducing the appropriate phase shifts to the signals at a point between the elements and the mixer.

4. Mixer

A critical part of each channel is extracting the phase difference between the two antenna elements, and is the function of the mixer. The mixer is used to achieve frequency conversion. Although a mixer is a nonlinear device, the mixing process is often considered as a linear process in the sense of input/output superposition. The information contained in the input signal does not change, only the frequency is shifted. In an amplifier chain, a mixer can be treated as an amplifier. A mixer has a gain, a noise figure (relatively high), and a third-order intercept point. Its gain is usually less than unity (negative in decibels or

a loss), although in some mixers the gain might be positive. The noise figure may often be taken as equal to the loss of the mixer unless another value is given by the manufacturer.

There are many frequencies at the output of a mixer besides the desired one. The high frequency terms (the term giving the sum of the input frequencies) will be neglected because in actual design these terms will be filtered out through a low pass filter.

In Chapter III, the operation of a mixer was presented and the expression giving the mixer's output voltage as a function of the phase difference of its inputs was derived. Equation (3-13) relates its output voltage to the phase difference, and the equation (3-14) relates its output voltage to the angle of incidence of the incoming wave. These expressions represent the ideal case of a mixer, but in an actual mixer the results will deviate from this.

The only term, which survives out of the low pass filter, is the DC term. But, there will be variations in this DC output level for similar signals at their inputs, because the mixers are not identical. Therefore, it is necessary to test the individual mixers and record the differences in performance so that they may be accounted for in the design. The approach is to create a signal of 8.5 GHz and send phase-shifted versions of it through cables to both inputs of the mixers. Phase differences can be obtained with phase shifters in one branch, thus simulating a plane wave excitation at the mixer input. The test setup includes a network analyzer with its signal generator, a power splitter, two phase-shifters, and a voltmeter. The comparison between the theoretical results and the measured ones show that the general behavior of these mixers were as expected.

5. Construction and testing of the antenna

Without phasing any significant problems and following the design, as described in previous analysis, the individual components are combined together into the antenna structure, as shown in the next Figures (6.8 – 6.12).

Figure 6.8 illustrates the antenna (front view), focused on the ground plane and the elements of the array antenna. Figure 6.9 illustrates the antenna, as shown from the backside of the ground plane. It shows the individual components of the construction focusing the waveguides, the low noise amplifiers, and the mixers. Figure 6.10 shows the antenna mounted on the pedestal in the anechoic chamber. Note the use of absorber to avoid any diffraction and reflection of the radiating wavefront. Also note the two dummy loads present.

In order to have a better understanding of the components, which are used to construct the antenna, Figure 6.11 illustrates a close view of the antenna elements. Figure 6.12 presents the waveguides and the Low Noise Amplifiers (LNAs) showing the difference between the big (a) and the small ones (b). Figure 6.13 shows the mixer used in each channel. In order to take the experimental results in the anechoic chamber a transmitting antenna was used to play the role of the radiating source, as shown in the Figure 6.14.

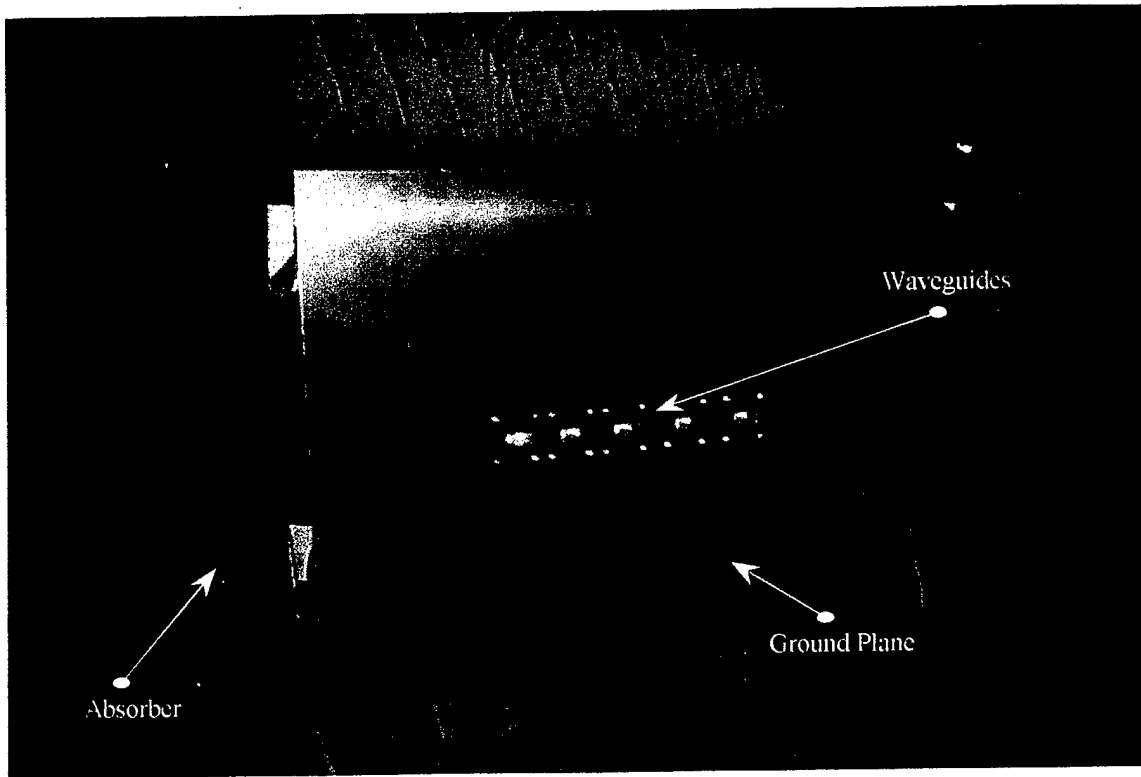


Figure 6.8: Built antenna (front view), surrounded by absorber for reducing the edge effects.

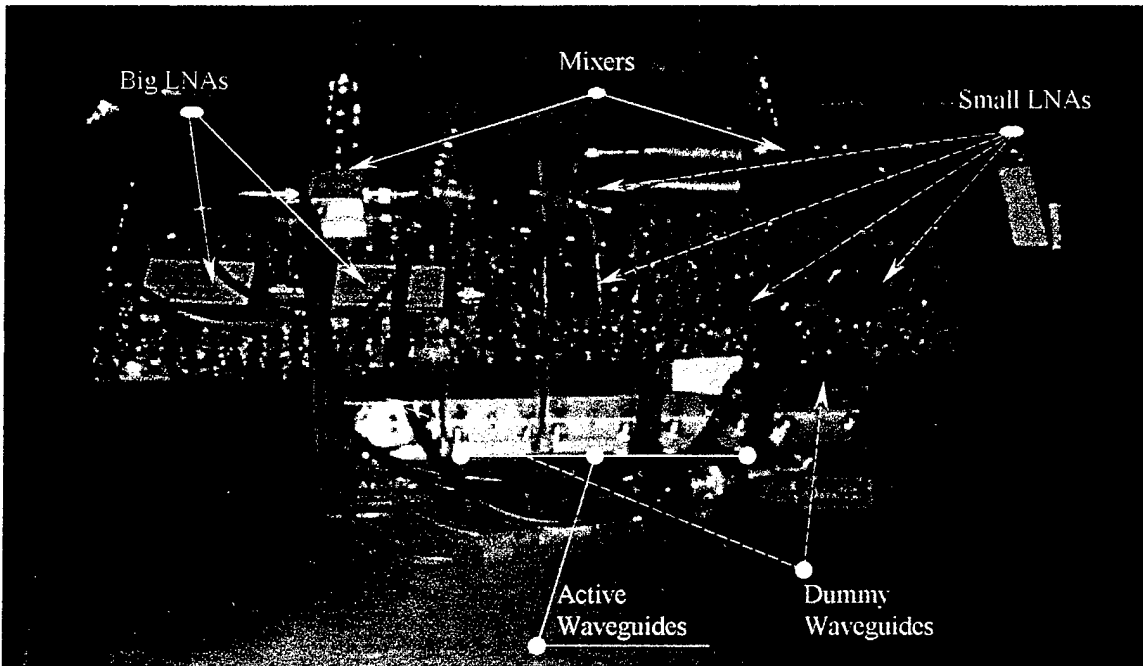


Figure 6.9: Built antenna (backside view), showing the parts of the construction.

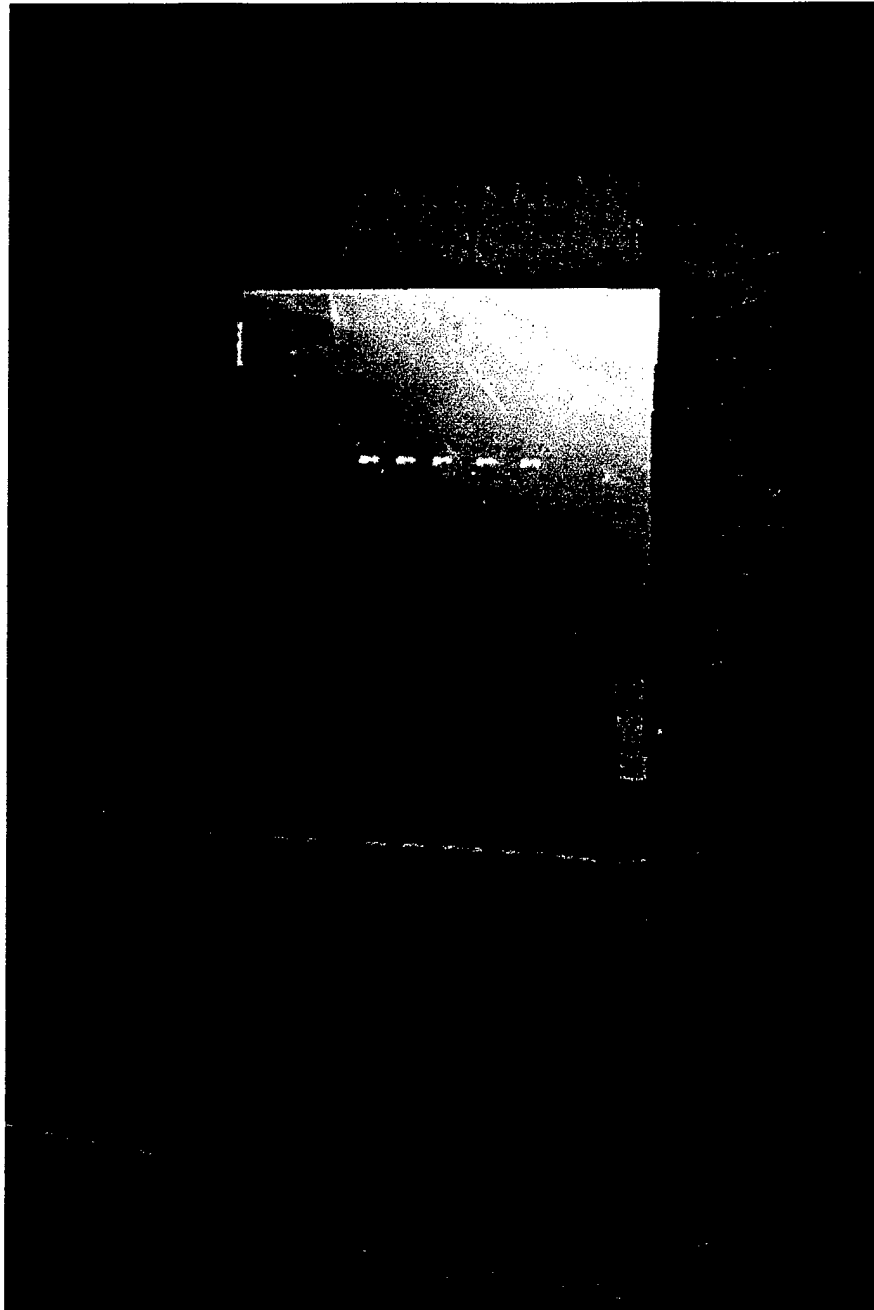


Figure 6.10: Antenna mounted on the pedestal, in the anechoic chamber.

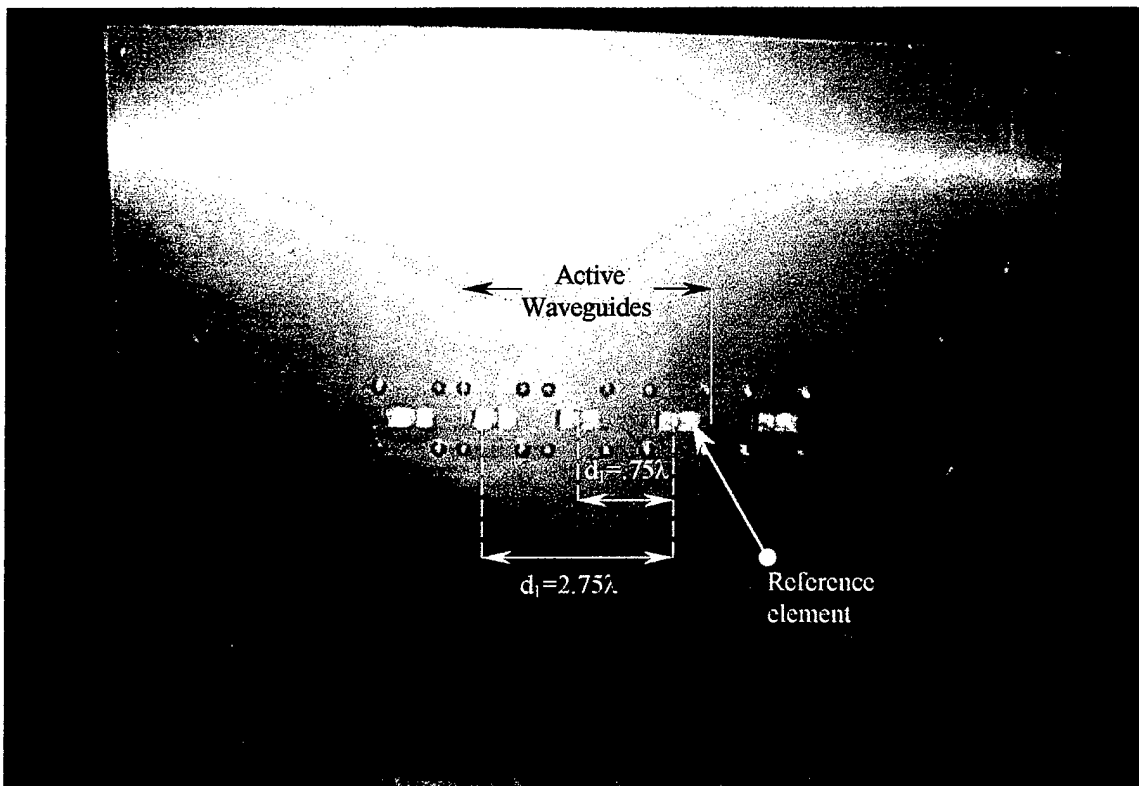


Figure 6.11: Ground plane with the antenna elements in detail.

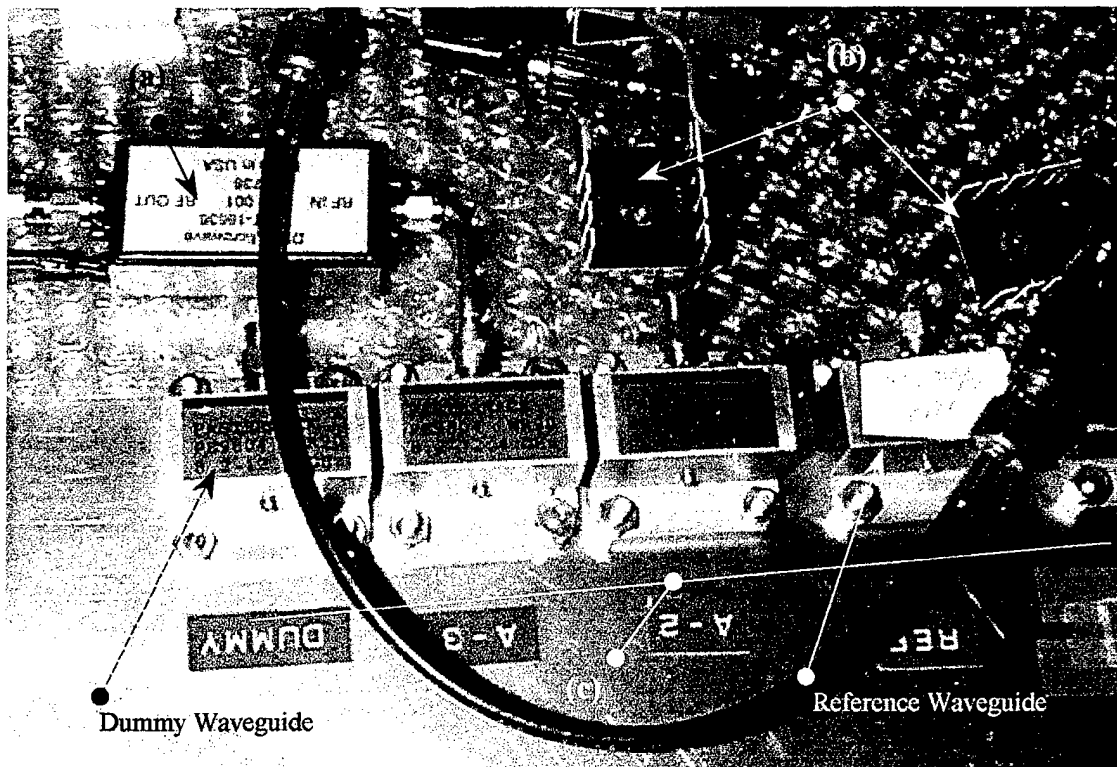


Figure 6.12: A focus on some components of the antenna:

- (a) Big Low Noise Amplifiers (LNAs),
- (b) Small Low Noise Amplifiers (LNAs),
- (c) Waveguides.

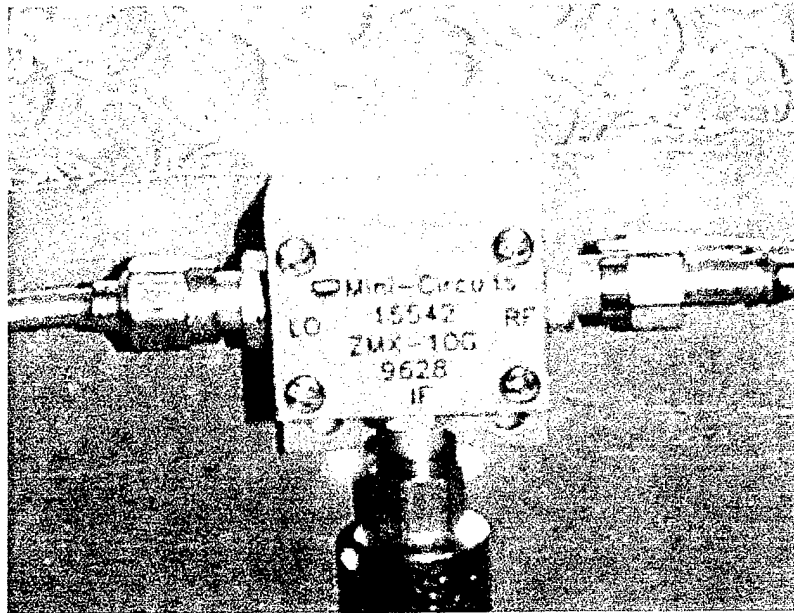


Figure 6.13: A mixer connected at the system.

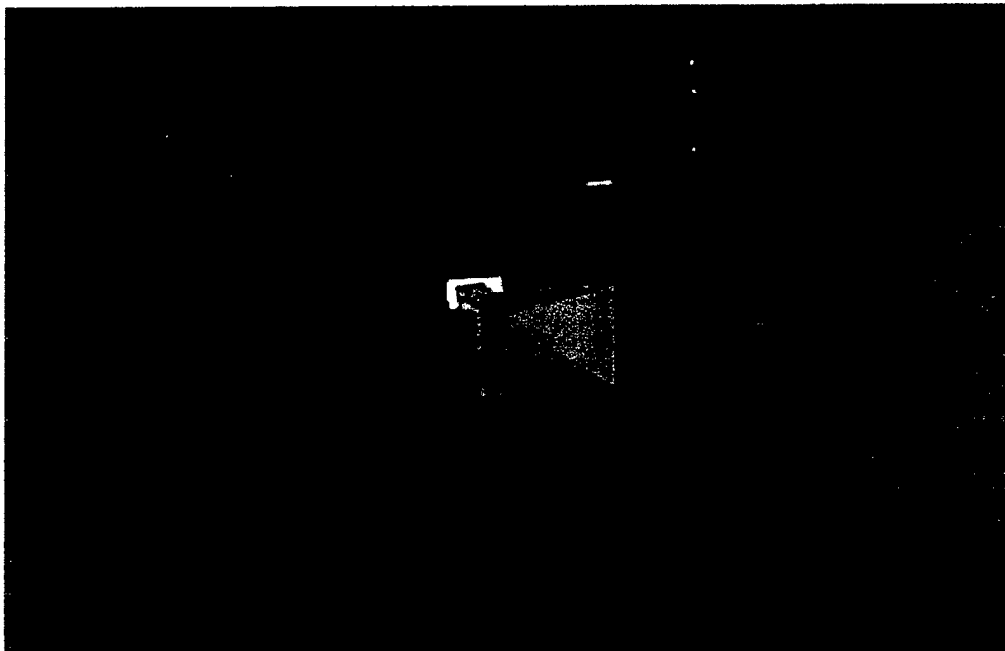


Figure 6.14: Transmitting horn antenna in the anechoic chamber.

6. Labview program for reading the mixer output voltage

The anechoic chamber facility at the Naval Postgraduate School is used for the antenna pattern measurements of the H-field (taken for each pair of elements). The mixer output voltage values are read, using a multimeter, and recorded. To automate this process, LabVIEW (Laboratory Virtual Instrument Engineering Workbench) was used to create a program for giving the appropriate commands to read the data and send them to a device for storage. This program is very useful, since it gives the user the chance to read the data faster and with better accuracy.

LabVIEW is a powerful and flexible instrumentation and analysis software system. LabVIEW departs from the sequential nature of the traditional programming languages and features a graphical programming environment and all the tools needed for data acquisition, analysis, and presentation. With this graphical programming language, called "G", we can program using a block diagram approach. After we create a block diagram program, LabVIEW compiles it into machine code.

LabVIEW programs are called Virtual Instruments (VIs). A VI consists of a front panel and a block diagram. The front panel specifies the inputs and outputs and features the user interface for interactive operation. Behind the front panel is the block diagram, which is the actual executable program. The components of a block diagram, icons, represent lower-level instruments and program control structures. We "wire" the icons together to indicate data flow in the block diagram.

LabVIEW integrates data acquisition, analysis, and presentation in one system. An instrument library with drivers for hundreds of popular instruments simplifies instrument

control applications. Because LabVIEW is graphical in nature, it is inherently a data presentation package. Output appears in the form of charts, graphs, and user-defined graphics. The LabVIEW program is shown in Appendix B.

B. SUMMING AMPLIFYING CIRCUIT

A DC bias and amplifying circuit is designed and fabricated in order to provide the desired DC input voltage to the comparator stage that follows this circuit.

The circuit in Figure 6.15 is the basic inverting summing circuit. The value and polarity of the output voltage V_o is determined by the sum of the input voltages $V_1, V_2, V_3, \dots, V_n$ and by the values of the externally wired resistors $R_1, R_2, R_3, \dots, R_n$ connected to the inverting terminal of the Op Amp. Since the noninverting input is at ground potential, the inverting input and the right sides of input resistors R_1 through R_n are virtually grounded too. There is a resistance R_f in the negative-feedback path. The currents $I_1, I_2, I_3, \dots, I_n$ in the input resistors can be shown, by Ohm's law, as

$$I_1 \cong \frac{V_1}{R_1}, \quad I_2 \cong \frac{V_2}{R_2}, \quad I_3 \cong \frac{V_3}{R_3}, \quad \dots, \quad I_n \cong \frac{V_n}{R_n}.$$

Similarly, the current in R_f is given by

$$I_f \cong \frac{-V_o}{R_f},$$

where the negative sign indicates that V_o is out of phase with the net voltage at the inverting input.

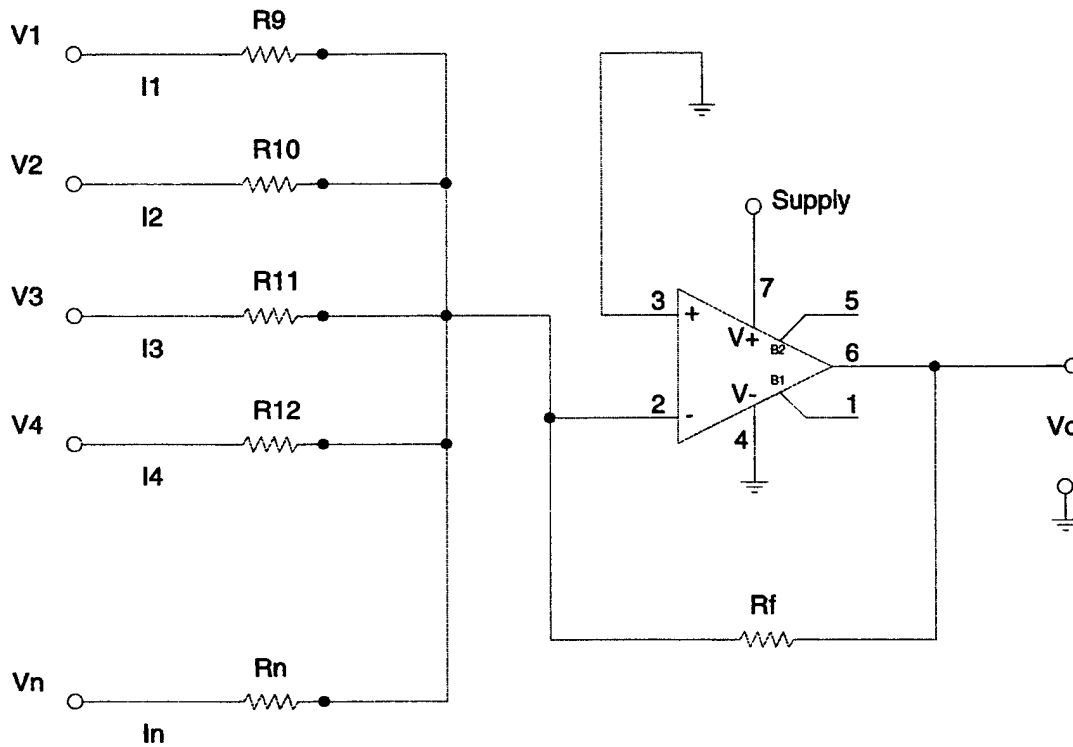


Figure 6.15: Basic Inverting Summing Circuit.

Since the sum of the input currents is equal to the feedback current, assuming that the Op Amp is ideal, it can be shown that

$$I_f \cong I_1 + I_2 + I_3 + \dots + I_n \quad \text{or}$$

$$\frac{-V_o}{R_f} \cong \frac{V_1}{R_1} + \frac{V_2}{R_2} + \frac{V_3}{R_3} + \dots + \frac{V_n}{R_n}.$$

Multiplying both sides of the previous equation by $-R_f$ shows that, generally, the output voltage is given by

$$V_o \cong -R_f \left(\frac{V_1}{R_1} + \frac{V_2}{R_2} + \frac{V_3}{R_3} + \dots + \frac{V_n}{R_n} \right). \quad (6-3)$$

That is, the output voltage is a weighted sum of the input signals $V_1, V_2, V_3, \dots, V_n$. This circuit is therefore called a **weighted summer**. Note that each summing coefficient may be independently adjusted by adjusting the corresponding “feed-in” resistor (R_1 to R_n). This nice property, which greatly simplifies circuit adjustment, is a direct consequence of the virtual ground that exists at the inverting Op Amp terminal. [Ref. 16]

The original thought was to use another kind of weighted summer, where instead of using the virtual ground, we could substitute it by another set of input voltages Applied to the non-inverting terminal of the Op Amp. This configuration gave a shifting to the voltage level, but because of the obtained resolution of the comparators a decision made to change the summer to a summing amplifier. This configuration amplifies the input signal and spreads the threshold voltages in order to avoid any interactions between them. By using the circuit shown in Figure 6.16, the objective is obtained to shift and amplify the input signal in order to have a better separation between the reference voltages to the comparator section.

As we see in equation (6-3) the output voltage is a linear sum (with negative coefficients) of the inputs. But the need for having positive output voltage, given by equation (6-4), orders the insertion of an inverting amplifier, as shown in Figure 6.16.

$$V_o = \frac{R_f}{R_2} V_x + \frac{R_f}{R_1} V_{\sin} \quad (6-4)$$

Also, the need for having small input resistance to the summing amplifier dictates the insertion of a buffer to the input of the summing amplifier. There are some other advantages of using the buffer, like the opportunity to adjust the input voltage to the desired value of amplification and the opportunity of using just one power supply for all the components in the circuit and the input voltages.

The above circuit, for each individual channel, is constructed using three (3) Op Amps (LM 741CN) for the buffer, summing amplifier and inverter, a potentiometer and metal film fixed resistors. The specification data sheets of the LM 741CN are shown in Appendix E. As the schematic in Figure 6.14 shows, 10K and 1.74K resistors, and 5K potentiometer (1.507K used resistance), were used. In order to have the desired amplification the following relationships are required,

$$V_x = 1.78V ,$$

$$\frac{R_f}{R_1} = 5.547.$$

For the components of the circuit, having the above values, the output voltage becomes

$$V_o \cong 1.78V + 5.747V_{\sin} . \quad (6-5)$$

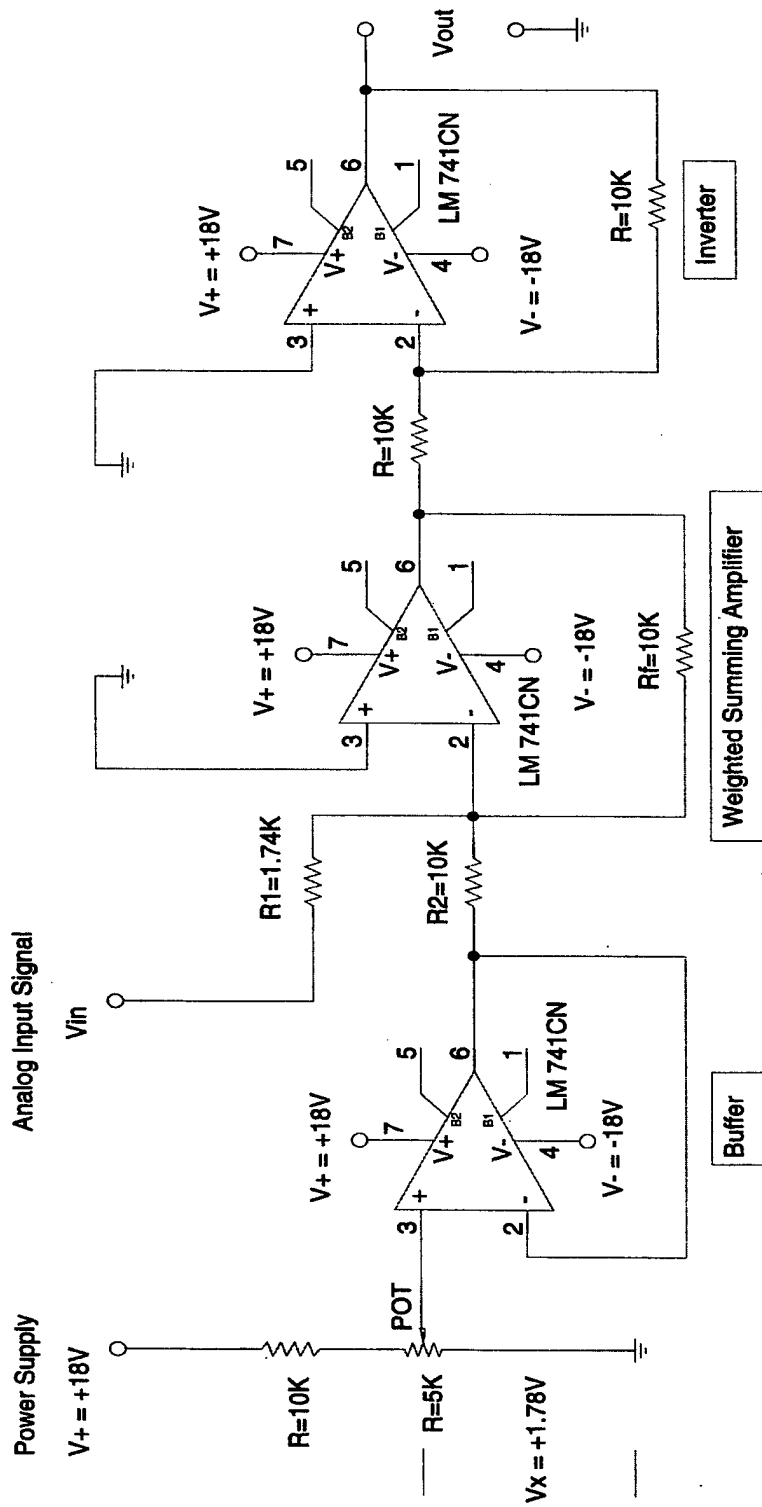


Figure 6.16: Weighted Summing Amplifier Circuit.

After the construction, this circuit was tested using the following devices

- PS 503 A (Dual Power Supply) for the Op Amps supply voltage +18V, -18V, and the Buffer,
- DM 502 A (Autoranging Digital Multimeter),
- WAVETEK 148 Generator for V_{sin} = input signal,
- Hp 3478A Multimeter for copying the output voltage from the Op Amp.

Using the results obtained from the multimeter, the response of the weighted summing amplifier is given by the Figure 6.17.

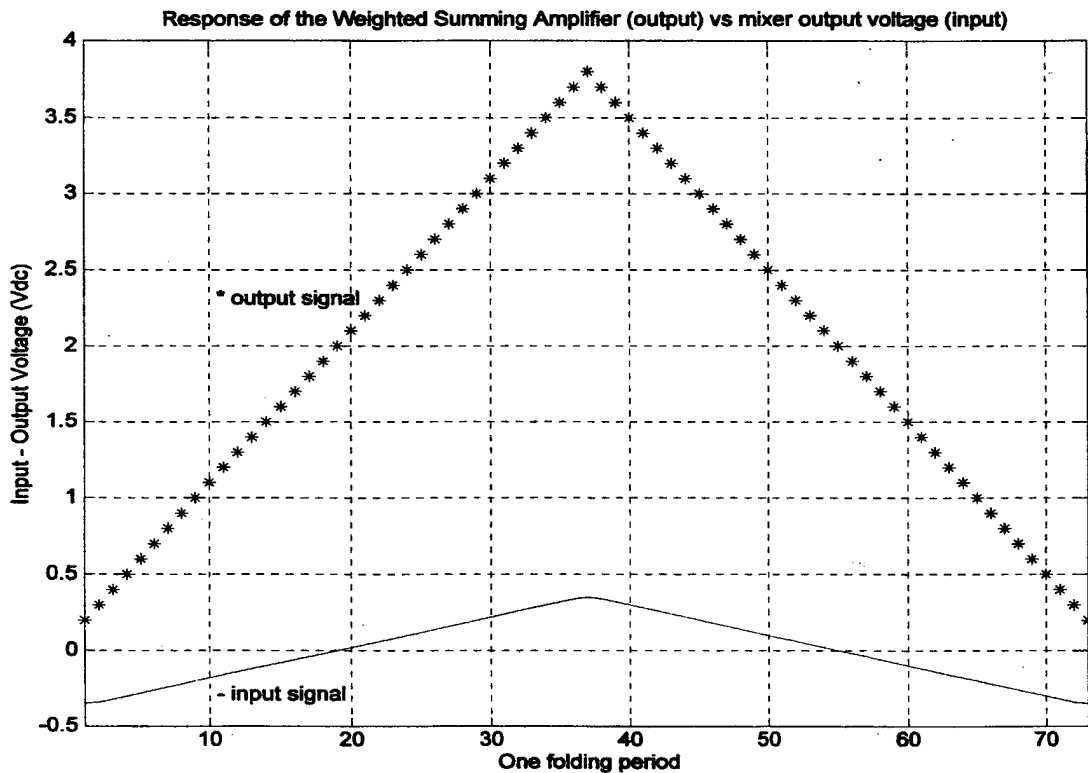


Figure 6.17: Response of the Weighted Summing Amplifier circuit.

C. A/D CONVERSION BOARD

The A/D conversion board is used to quantize the analog voltage signals coming from the summing amplifier circuit. There is one A/D conversion board containing two comparator boards, one for each channel. One comparator board for *mod11* and one for *mod6*. There is a section for the EEPROM, which is used to recombine both channels and map the Transfer Function of the OSNS antenna. There are two main subsections in each comparator board, the reference voltage generation subsection and the comparator subsection. A block diagram of the A/D conversion board, with DI/O board, and LabVIEW VI are shown in Figure 6.18. Schematic diagrams of the parts of the A/D conversion are shown in Figure 6.19, Figure 6.20, and Figure 6.21.

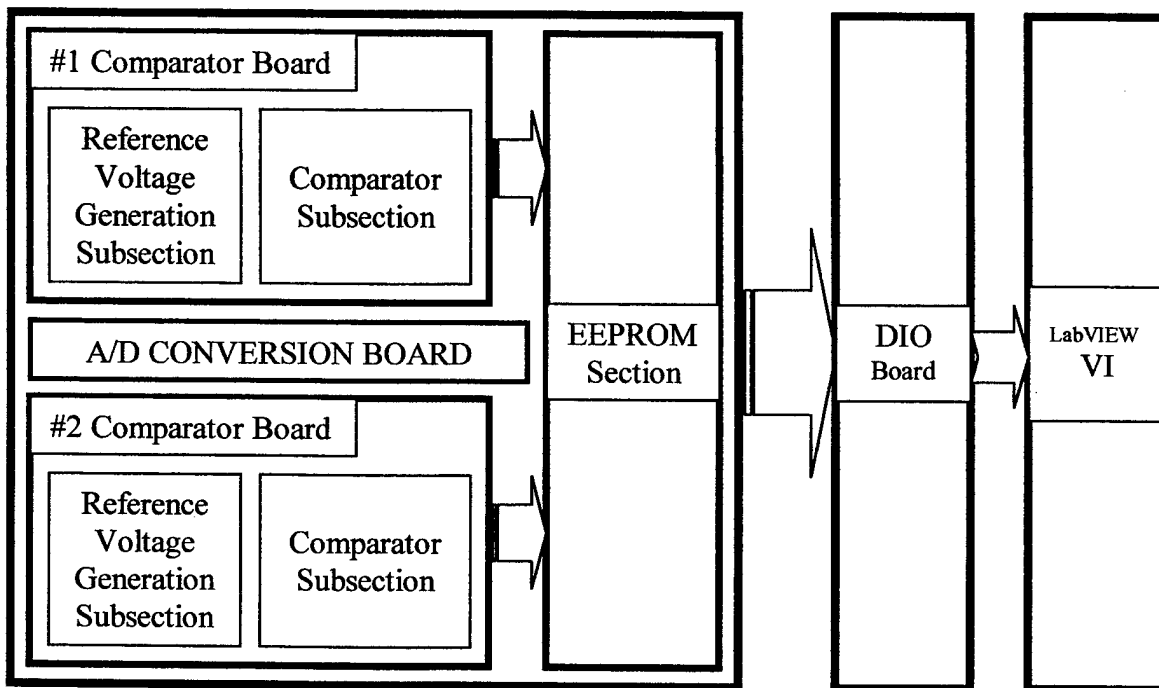


Figure 6.18: Block Diagram of the A/D Conversion Board, DI/O board and LabVIEW VI.

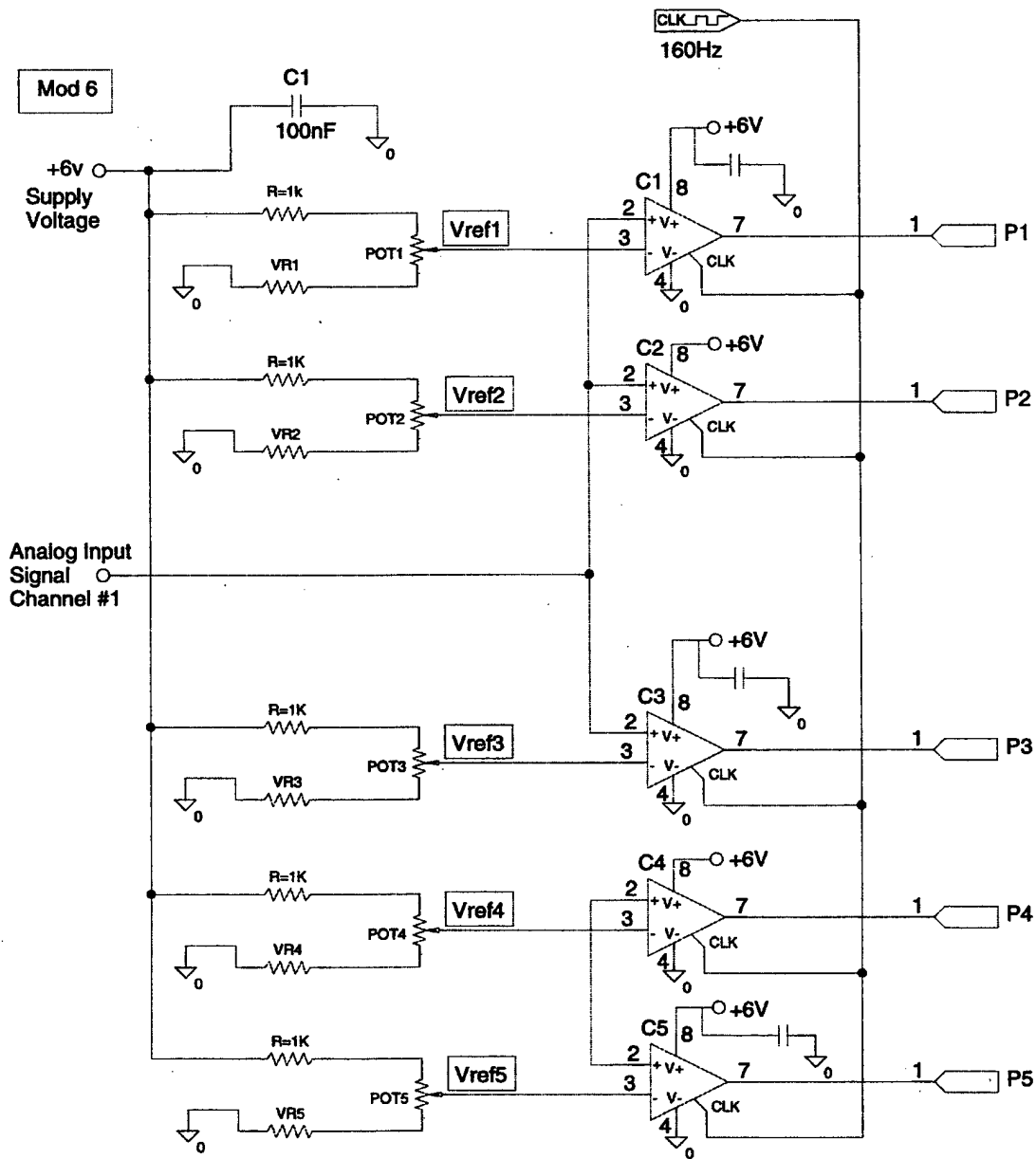


Figure 6.19: Schematic Diagram of the Comparator board for Channel #1 (mod 6).

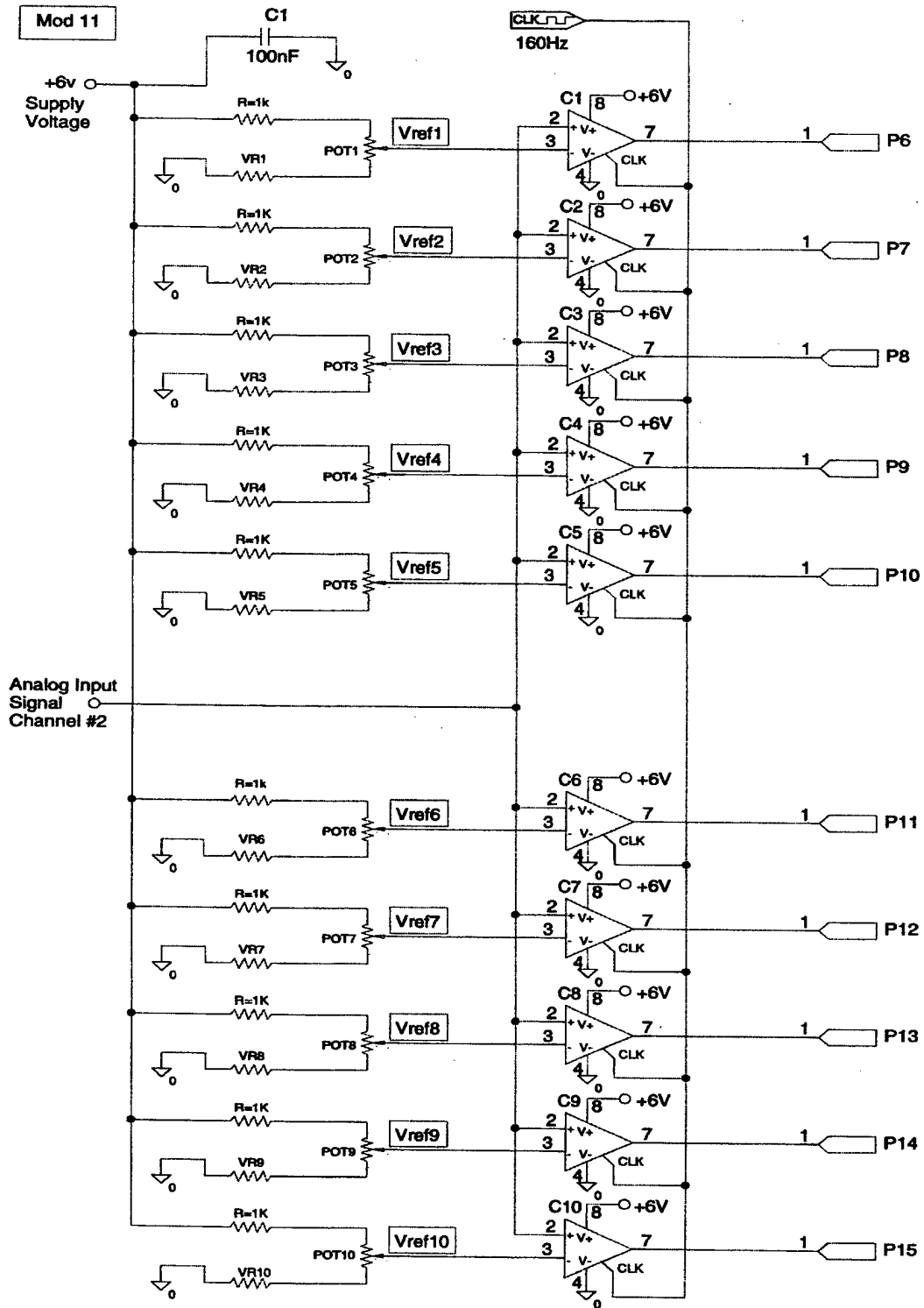


Figure 6.20: Schematic Diagram of the Comparator board for Channel #2 (mod 11).

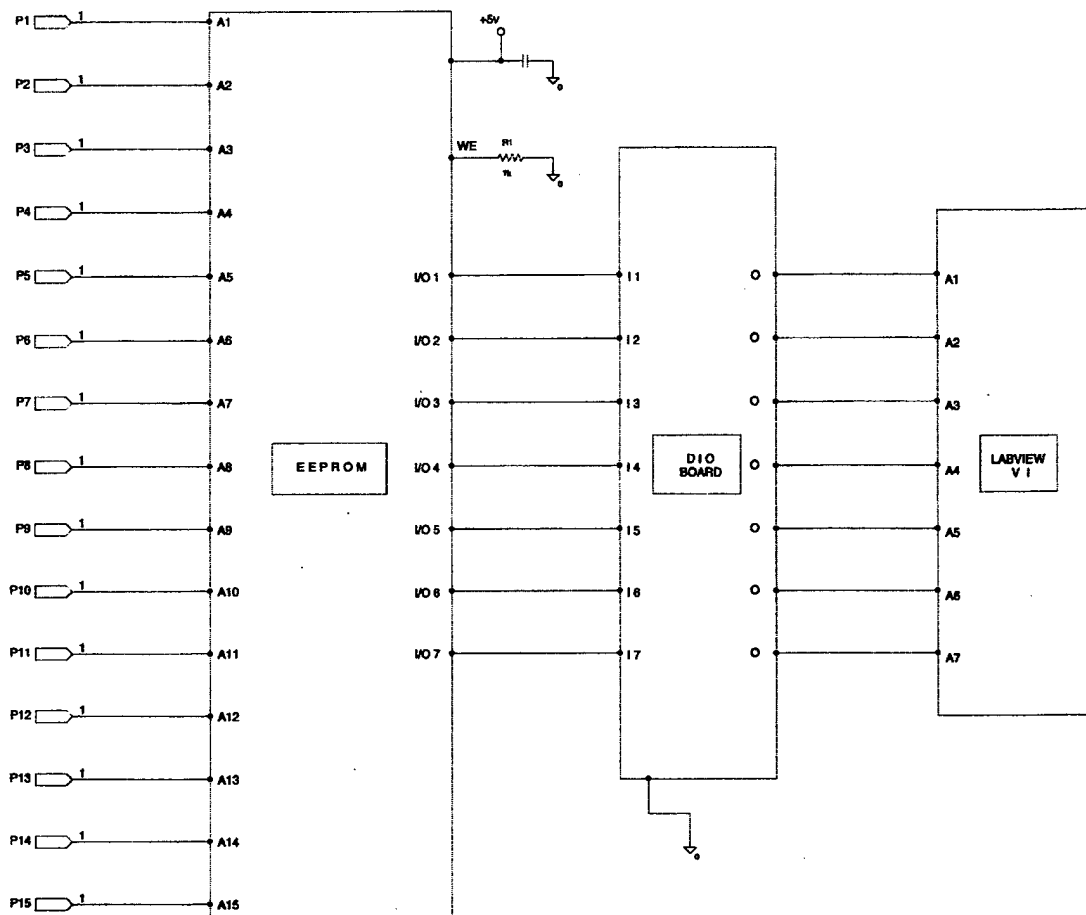


Figure 6.21: Schematic Diagram of the EEPROM section, DI/O board and LabVIEW VI.

1. Reference Voltage Generation Subsection

The reference voltage generation subsection is responsible for generating the reference voltages, or the comparator matching threshold values, in order to give the comparators the desired level above which they switch from the “ground” or “off” state (zero “0”) to the “upper” or “on” state (one “1”). The reference voltage, for each comparator, is generated using a set of metal film fixed resistors and a *cermet*

potentiometer of 50Ω (Digi Key 3296W-500-ND) or 100Ω (Digi Key 3296W-101-ND) variable resistance, depending on the level of accuracy we need for each comparator.

The following algorithm is used to obtain the desired thresholds for the comparators. Equation (6-6) gives the threshold width for the modulus m_i . Equation (6-7) gives the DOA, which corresponds to the threshold voltage level t_n . Equation (6-8) gives the threshold voltage t_n (in volts), which is going to be used for the n^{th} comparator state of each channel, using interpolation between the data coming from the measurements in the anechoic chamber. The threshold width for modulus m_i is

$$tw(m_i) = \frac{|(DOA)|_{V_{min}} - (DOA)|_{V_{max}}|}{m_i} \quad (6-6)$$

where $DOA|_{V_{min}}$ = direction of arrival corresponding to the minimum voltage of the folding period,

$DOA|_{V_{max}}$ = direction of arrival corresponding to the maximum voltage of the folding period.

The DOA corresponding to the threshold voltage level after interpolation, using the data out of the summer, is given by

$$DOA|_{t_n} = DOA|_{V_{min}} - n \cdot tw(m_i) \quad (6-7)$$

where $n =$ number of thresholds for each modulus ($n = 1, 2, 3, \dots, m_i - 1$).

The n^{th} threshold voltage level is given by

$$t_n = V|_{DOA|_{m_i}}. \quad (6-8)$$

The above equations for the moduli *mod11* become as follows

$$tw(\text{mod } 11) = \frac{|(DOA)|_{V_{\min}} - (DOA)|_{V_{\max}}|}{11}$$

and the DOA, for the 1st threshold, is given by

$$DOA|_{t_1} = DOA|_{V_{\min}} - 1 \cdot tw(\text{mod } 11)$$

where the threshold voltage t_1 is given by $t_1 = V|_{DOA|_{t_1}}$.

The number of comparators, for each modulus m_i , is given by $m_i - 1$. So, for the case of the moduli $m_1 = 6$ and $m_2 = 11$, the number of comparators are 5 and 10, respectively.

After a number of calculations and interpolations the threshold voltages, for *mod11* and *mod6*, are given in Table 6.2.

<i>Modulus</i>		$m_1 = 6$	$m_2 = 11$
<i>Elements</i>		(1,3)	(1,2)
<i>T</i>	T_1	0.481651	0.262528
<i>H</i>	T_2	1.069004	0.415797
<i>R</i>	T_3	2.048441	0.696651
<i>E</i>	T_4	2.938367	1.144543
<i>S</i>	T_5	3.468105	1.649503
<i>H</i>	T_6	-----	2.346490
<i>O</i>	T_7	-----	2.956342
<i>L</i>	T_8	-----	3.368175
<i>D</i>	T_9	-----	3.587586
<i>S</i>	T_{10}	-----	3.717819
<i>(V)</i>			

Table 6.2: Normalized Comparator Matching Threshold Values (Volts), for each pair of elements.

By using the supply voltage $V_{cc}=+6V$ for the circuit and the above desired threshold values (reference voltages), a procedure has been followed to set the exact reference voltage for each comparator. The designs in Figure 6.19, and Figure 6.20 have been captured and the section for generating the threshold voltages, for each channel, has been designed to keep the reference voltages constant. The capacitors, connecting the supply voltage and the ground, are placed to reduce the noise from the supply voltage. The capacitors at the comparators C6-...-C15, in the schematic diagram in Figure 6.20,

are not shown to avoid any further confusion. These capacitors are connected, in the real circuit, as the ones (C1-...-C5) shown in the schematic diagram in Figure 6.19.

The parallel construction of the reference voltages has been decided, makes it much easier to set each individual reference voltage without disturbing the reference voltage for the other comparators. The design in Figure 6.22 illustrates the reference voltage generation subsection and the comparator subsection for the i^{th} Comparator.

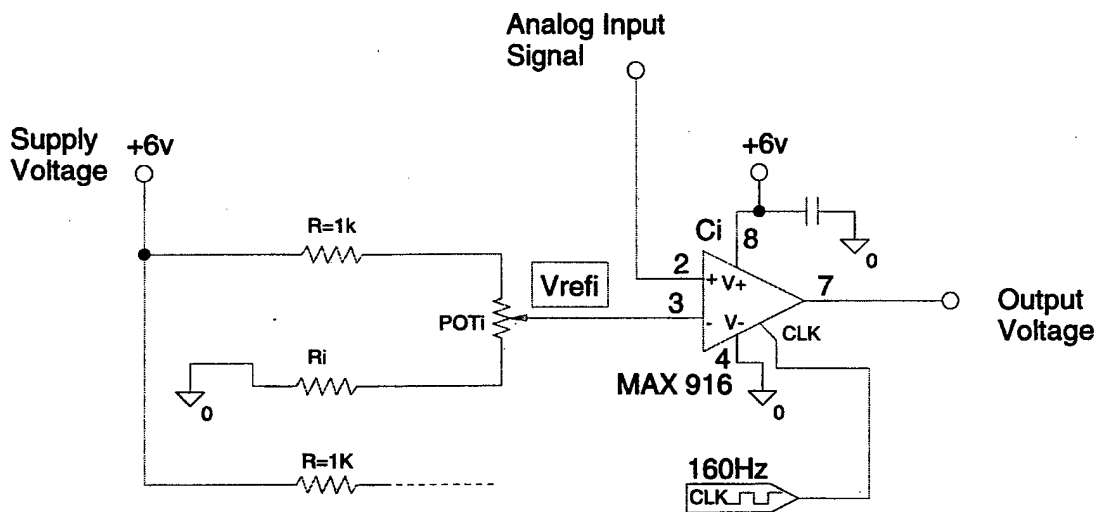


Figure 6.22: Schematic diagram illustrating the sub-circuit of resistors in series, with a potentiometer embedded, connected straight to each comparator subsection.

In the reference voltage generation subsection, the sub-circuit of the resistors in series with the potentiometer embedded, has been designed for two reasons. One reason is to obtain much better accuracy in the desired reference voltage, and the other one is to

change the reference voltage, for each comparator, by just changing the ratio of the potentiometer we desire to use. The comparator subsection is analyzed in next subsection.

The procedure that has been followed to set the exact reference voltage for each comparator is as follows:

- Calculate the required theoretical resistance R_{ref_i} concerning each desired reference voltage V_{ref_i} , for a constant resistance R , using the formula

$$R_{ref_i} = R \left[\frac{V_{ref_i}}{V_{cc} - V_{ref_i}} \right], \quad \text{for } i = 1, 2, 3, \dots, m_i-1, \quad (6-9)$$

where $R_{ref_i} = R_i + VR_i$,

V_{ref_i} = desired threshold as it is determined in the beginning of the section,

V_{cc} = +6V supply voltage,

R = 1K Ω .

- Find the closest available fixed metal resistance (smaller than the theoretical resistance R_{ref_i}).
- The rest of the theoretical resistance is going to be covered by the most appropriate valued potentiometer resistance VR_i of 50 Ω or 100 Ω .
- Measure the actual total resistance R_{T_i} , for each comparator resistor cascade.
- Calculate, the resistance R_{ref_i} , for the supply voltage of $V_{cc}=+6V$, using the following expression

$$R_{ref_i} = \frac{V_{ref_i}}{I_i} \quad (6-10)$$

where $I_i = \frac{V_{cc}}{R_{T_i}}$.

- Decide which potentiometer you want to use, in order to have the best accuracy, since each one of them have a range of resistance adjusted through a 25-turn adjustment.
- Adjust the potentiometer for this threshold value.

NOTE 1: For all these measurements, you have to wait a specific amount of time to get a constant output, approaching the desired accuracy. In order to get this accuracy the best thing to do is to use a multimeter giving four-digit accuracy. Also, for getting better accuracy use two terminals for each end of the resistor.

NOTE 2: In order to make these measurements, use each set of resistors separately, with no supply voltage connected.

After following the above theoretical procedure, the theoretical R_{ref_i} and the corresponding V_{ref_i} , for each channel, are given by Table 6.3.

<i>mod11</i>				<i>mod6</i>			
V_{ref_1}	0.262528V	R_{ref_1}	45.879 Ω	V_{ref_1}	0.481651V	R_{ref_1}	89.026 Ω
V_{ref_2}	0.415797V	R_{ref_2}	76.135 Ω	V_{ref_2}	1.069004V	R_{ref_2}	225.093 Ω
V_{ref_3}	0.696651V	R_{ref_3}	90.943 Ω	V_{ref_3}	2.048441V	R_{ref_3}	541.720 Ω
V_{ref_4}	1.144543V	R_{ref_4}	240.935 Ω	V_{ref_4}	2.938367V	R_{ref_4}	1,016.757 Ω
V_{ref_5}	1.649503V	R_{ref_5}	390.560 Ω	V_{ref_5}	3.468105V	R_{ref_5}	1,429.879 Ω
V_{ref_6}	2.346490V	R_{ref_6}	660.337 Ω	V_{ref_6}	-----	R_{ref_6}	-----
V_{ref_7}	2.956342V	R_{ref_7}	1,007.819 Ω	V_{ref_7}	-----	R_{ref_7}	-----
V_{ref_8}	3.368175V	R_{ref_8}	1,332.419 Ω	V_{ref_8}	-----	R_{ref_8}	-----
V_{ref_9}	3.587586V	R_{ref_9}	1,564.308 Ω	V_{ref_9}	-----	R_{ref_9}	-----
$V_{ref_{10}}$	3.717819V	$R_{ref_{10}}$	1,716.486 Ω	$V_{ref_{10}}$	-----	$R_{ref_{10}}$	-----

Table 6.3: Theoretical values for R_{ref_i} and the corresponding V_{ref_i} , for each channel.

By measuring the total resistance for the series resistors and following the procedure for the actual reference resistance, Table 6.4 has been generated. This Table provides the total resistance R_{T_i} for each comparator state, the current I_i , the actual R_{ref_i} corresponding to the desired V_{ref_i} , the fixed resistance R_i in series with the appropriate potentiometer VR_i , for each channel. Note the difference in V_{ref_i} between Tables 6.3 and 6.4. The threshold voltage, V_{ref_i} , in Table 6.4, is affected by the noise generated in each individual comparator.

Thresholds	R_T (Ω)	I_i (mA)	R_{ref_i} (Ω)	V_{ref_i} (V)	R_i (Ω)	VR_i (Ω)
Mod 6						
T_1	1,116.500	5.284	95.3616	0.513651	66.500	50
T_2	1,242.321	4.749	231.2197	1.108004	210.365	50
T_3	1,560.284	3.781	559.3784	2.116441	486.324	100
T_4	2,041.565	2.890	1,041.7817	3.010367	956.112	100
T_5	2,740.535	2.153	1,674.9365	3.606615	1,540.021	100
Mod 11						
T_1	1,081.254	5.457	61.490	0.335528	31.254	50
T_2	1,166.614	5.057	101.317	0.512397	66.514	100
T_3	1,168.079	4.844	147.9265	0.716510	118.080	100
T_4	1,291.212	4.569	272.3676	1.244543	241.212	50
T_5	1,419.236	4.157	409.053	1.700503	369.235	50
T_6	1,740.564	3.295	748.4527	2.466190	690.564	100
T_7	2,142.314	2.754	1,105.014	3.043242	1,042.314	100
T_8	2,512.366	2.348	1,498.978	3.520175	1,462.365	50
T_9	2,589.386	2.235	1,615.778	3.611861	1,539.385	100
T_{10}	2,840.254	2.077	1,820.082	3.780819	1,740.254	100

Table 6.4: Actual, measured values for the components included in each channel, for setting R_{ref_i} and the corresponding V_{ref_i} .

2. Comparator Subsection

The comparator, as a generalization, is an operational amplifier without any negative feedback. Op amps may be used as comparators, but a true comparator differs from an operational amplifier in several respects. A comparator has a slew rate as much as 100 times faster than that in an operational amplifier. It is not frequency-compensated and

thus would probably be unstable if negative feedback were applied. The output voltage of a comparator has only two states: positive saturation (high) and negative saturation (low).

The voltage comparator subsection is connected to the reference voltage generation subsection at the point where the negative input of the comparator is attached to the reference voltage V_{ref_i} . The sub-circuit for the voltage comparator is illustrated in Figure 6.22, in previous subsection. When the input voltage becomes greater than the reference voltage, the output slews to positive saturation (high); when the output becomes less than the reference voltage, the output slews to negative or ground saturation (low). The comparator subsection of each channel uses a set of MAX916 Ultra High-Speed, High-Resolution, Single-/Dual-Supply TTL Comparators made by Maxim Integrated Products.

The number of comparators needed in each channel is given by m_i-1 . So, for the modulus 11 channel, we need 10 comparators, and for the modulus 6 channel, we need 5 comparators. Each of the MAX916 contains 2 comparators. So, five of these MAX916 are installed on the mod11-channel comparator board, and three are installed on the mod6-channel comparator board. A block diagram of the MAX916 is shown in Figure 6.23. The MAX916 eliminates oscillation by separating the comparator input and output stages with a negative edge-triggered master/slave flip-flop.

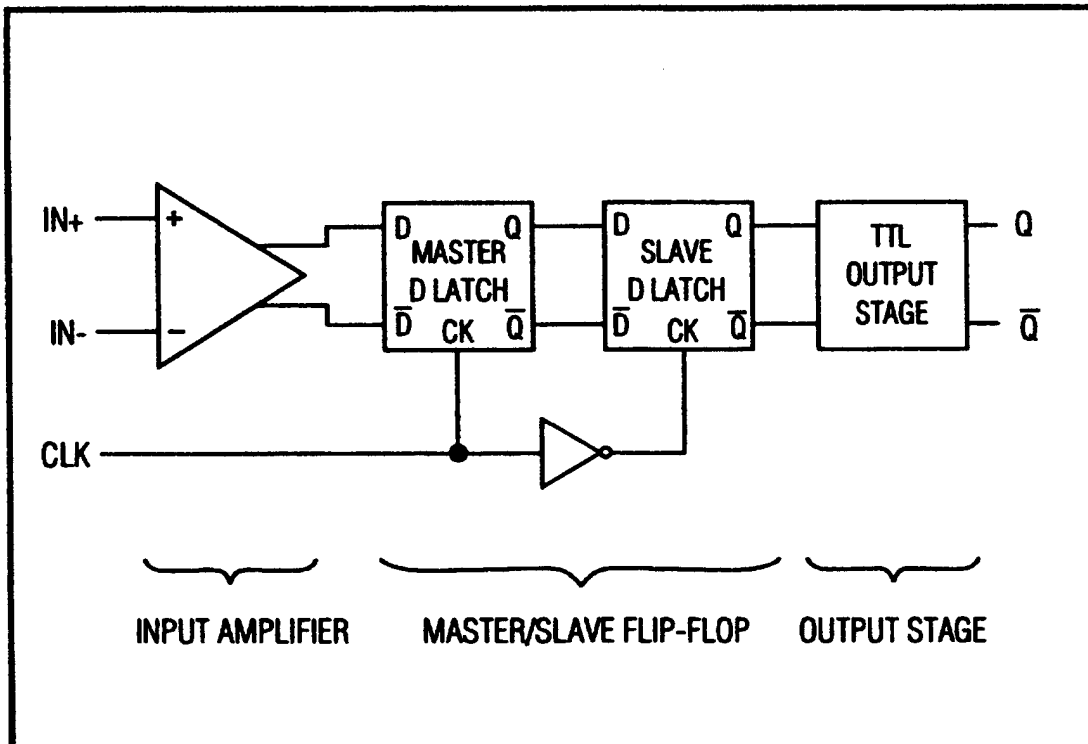


Figure 6.23: Block diagram of a MAX916 comparator [Ref. 17].

The comparator is divided into three stages, as shown in the Block Diagram:

1. Input Amplifier,
2. Master/Slave D Flip-Flop,
3. TTL Output Stage.

The input amplifier continuously monitors the input signal. The MAX916 can compare input signals as small as 2.4mV, which means the threshold voltages can be set with high accuracy to avoid unwanted “glitches”. The master latch samples the output of the input amplifier when the clock is high. The data is held by the master latch and is transferred to the slave latch only on the clock’s falling edge. The TTL outputs do not change on the

clock's rising edge. The master and slave latches are open on opposite phases of the clock, preventing a direct path from input to output at all times. This makes the MAX916 different from other comparators with simple output latches, and delivers high-speed performance without oscillations, even with slow-moving input signals. The timing diagram for the clock function is shown in Figure 6.24. Appendix D presents a detailed description of the MAX916 TTL comparator.

The timing clock for the comparators depends on the sampling rate we desire to have. The input signal is slow varying and is based on the rotation of the array antenna and the time that it takes the antenna system to take each sample, in the chamber. We require a resolution of one (1) sample of the incident signal, every 1/10-degree of angle. The specified rotation of the antenna is 5°/sec. The time, that the system requires to read each sample value and send it for storage, approaches ~6secs. Since the comparators we're using are made for ultra high frequency signals, and in order to avoid any undesirable oscillations about the threshold voltage we set the clocking frequency for the comparators at about 160Hz.

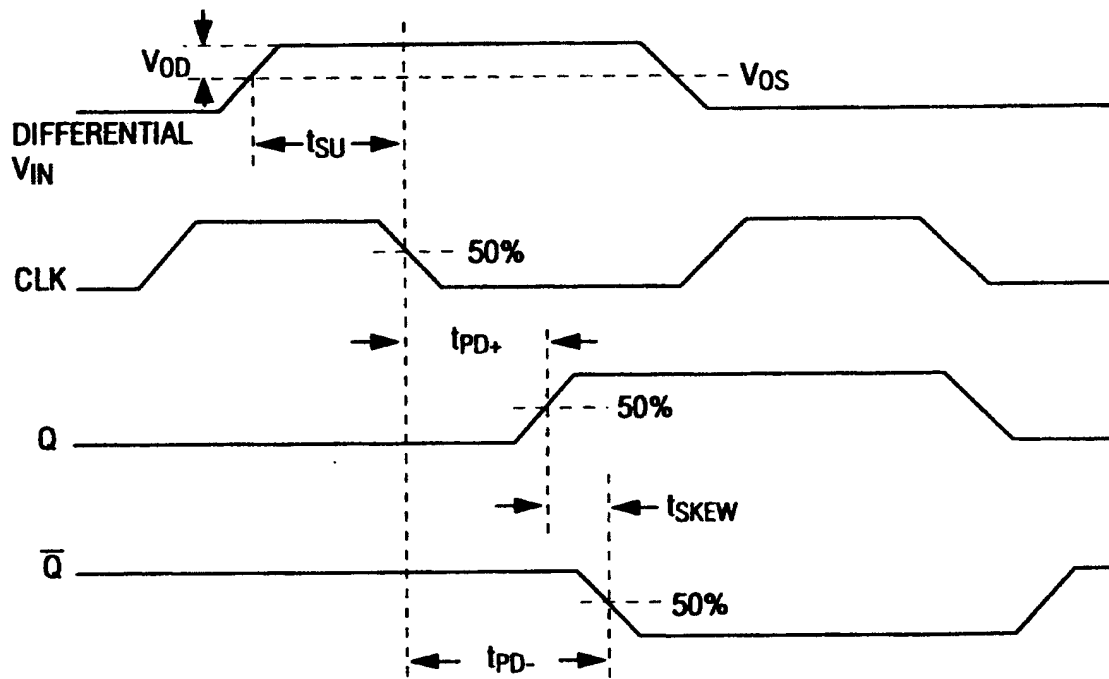


Figure 6.24: The timing diagram for the clock function [Ref. 17].

The procedure of comparing the input phase voltage with the comparator reference voltage, the set of comparators for each channel produces a thermometer-coded output. Then, the thermometer code is translated to a binary representation of the comparator state, as shown in Table 6.5.

mod 11				mod 6			
Thermometer Code T ₁₀ T ₉ T ₈ T ₇ T ₆ ... T ₅ T ₄ T ₃ T ₂ T ₁	Comparators "on" 11 digits 10 reference levels	Gray code	4-bit Binary code	Thermometer code T ₅ T ₄ T ₃ T ₂ T ₁	Comparators "on" 6 digits 5 reference levels	Gray code	3-bit Binary code
000000000	0	0000	0000	00000	0	000	000
000000001	1	0001	0001	00001	1	001	001
000000011	2	0011	0010	00011	2	011	010
000000111	3	0010	0011	00111	3	010	011
000001111	4	0110	0100	01111	4	110	100
000011111	5	0111	0101	11111	5	111	101
000011111	6	0101	0110	11111	5	111	101
000111111	7	0100	0111	01111	4	110	100
001111111	8	1100	1000	00111	3	010	011
011111111	9	1101	1001	00011	2	011	010
111111111	10	1111	1010	00001	1	001	001
111111111	10	1111	1010	00000	0	000	000
011111111	9	1101	1001	00000	0	000	000
001111111	8	1100	1000	00001	1	001	001
000111111	7	0100	0111	00011	2	011	010
000011111	6	0101	0110	00111	3	010	011
000001111	5	0111	0101	01111	4	110	100
000000111	4	0110	0100	11111	5	111	101
000000011	3	0010	0011	11111	5	111	101
000000001	2	0011	0010	01111	4	110	100
000000000	1	0001	0001	00111	3	010	011
000000000	0	0000	0000	00011	2	011	010
000000000	0	0000	0000	00001	1	001	001
000000001	1	0001	0001	00000	0	000	000
000000011	2	0011	0010	00000	0	000	000
000000111	3	0010	0011	00001	1	001	001
000001111	4	0110	0100	00011	2	011	010
000011111	5	0111	0101	00111	3	010	011
000011111	6	0101	0110	01111	4	110	100
000111111	7	0100	0111	11111	5	111	101
001111111	8	1100	1000	11111	5	111	101
011111111	9	1101	1001	01111	4	110	100
111111111	10	1111	1010	01111	4	110	100
111111111	10	1111	1010	00111	3	010	011
111111111	10	1111	1010	00011	2	011	010
011111111	9	1101	1001	00001	1	001	001
001111111	8	1100	1000	00000	0	000	000
000111111	7	0100	0111	00000	0	000	000
000011111	6	0101	0110	00001	1	001	001
000001111	5	0111	0101	00011	2	011	010
000000111	4	0110	0100	00111	3	010	011
000000011	3	0010	0011	01111	4	110	100
000000001	2	0011	0010	11111	5	111	101
000000000	1	0001	0001	11111	5	111	101
000000000	0	0000	0000	01111	4	110	100
000000000	0	0000	0000	00111	3	010	011
000000001	1	0001	0001	00011	2	011	010
000000011	2	0011	0010	00001	1	001	001

000000111	3	0010	0011	0000	0	000	000
000001111	4	0110	0100	0000	0	000	000
000011111	5	0111	0101	00001	1	001	001
000011111	6	0101	0110	00011	2	011	010
000111111	7	0100	0111	00111	3	010	011
001111111	8	1100	1000	01111	4	110	100
011111111	9	1101	1001	11111	5	111	101
111111111	10	1111	1010	11111	5	111	101
111111111	10	1111	1010	01111	4	110	100
011111111	9	1101	1001	00111	3	010	011
001111111	8	1100	1000	00011	2	011	010
000111111	7	0100	0111	00001	1	001	001
000011111	6	0101	0110	00000	0	000	000
000001111	5	0111	0101	00000	0	000	000
000000111	4	0110	0100	00001	1	001	001
000000011	3	0010	0011	00011	2	011	010
000000001	2	0011	0010	00111	3	010	011
000000000	1	0001	0001	01111	4	110	100
000000000	0	0000	0000	11111	5	111	101

Table 6.5: Translation of the thermometer code to a binary representation.

NOTE 1: In the second column, the decimal number represents comparator state.

NOTE 2: Gray code is very useful for high-speed signal.

3. EEPROM Section

This specific system, like any other one, requires memory for storing and program instructions (mapping). One important classification of memory is the read-only memory. Read-only memories (ROM) permit reading at the same high speeds as read/write (R/W) memories (or perhaps higher), but restrict the writing operation. ROM can be used to store a microprocessor operating system program. ROM is memory that contains fixed data patterns. A ROM can be viewed as a combinational logic circuit for which the input is

the collection of address bits of the ROM and the output is the set of data bits retrieved from the addressed location. This viewpoint leads to the application of ROMs in code conversion; that is, in changing the code of the signal from one system (e.g. binary) to another.

There are a lot of types of read-only memory, like fixed ROM; programmable ROM (PROM); and erasable programmable ROM (EPROM). The most useful of them is the erasable programmable ROM (EPROM), which is a ROM that can be erased and reprogrammed as many times as the user wishes. It is therefore the most versatile type of read-only memory. It should be noted, however, that the process of erasure and reprogramming is time-consuming and is intended to be performed only infrequently.

The erasure process can be accomplished by illuminating the memory cell, known as stacked-gate cell, with ultraviolet light of the correct wavelength ($\lambda \cong 250\text{nm}$) for a specified duration (10-30 min), depending on the strength of the UV lamp, using a quartz window (which is part of the EPROM chip). [Ref. 18]

A more versatile programmable ROM is the electrically erasable PROM (EEPROM). As the name implies, an EEPROM can be erased and reprogrammed electrically without the need for ultraviolet illumination. EEPROMs utilize a variant of the floating-gate MOSFET used as an EPROM cell, as shown in Figure 6.25.

An EEPROM is random access like a RAM in the sense that any address can be selected to be read. But the difference of the EPROM is that only one bit can be selectively erased with the electric erasure, which is an obvious advantage over UV erasure, which simultaneously erases the entire memory.

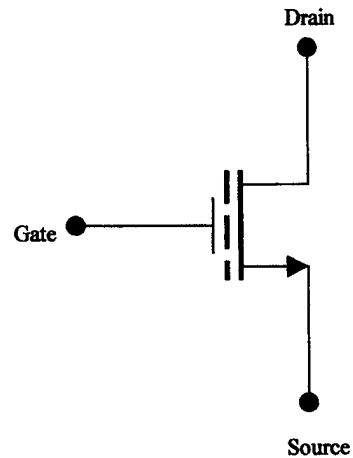


Figure 6.25: Circuit symbol of the floating-gate MOSFET used as an EPROM cell

[Ref.18].

The memory is organized into words, as shown in Appendix C. The cross section of each row with each column corresponds to a different address of the memory map, as shown in the respective Appendix. The programming of the EEPROM is made using a specific program MOD_EMUP made by Universal Programmer & Tester MODULAR CIRCUIT TECHNOLOGY.

The EEPROM we're using is the Xicor X28C256, which is a 262,144-bit CMOS EEPROM organized as 32K x 8. Before we use the memory map of the EEPROM, it is very useful to translate the binary digits of the comparator outputs into hexadecimal code since the EEPROM we're using needs input addresses in hexadecimal code and produces the output in binary after translating them first from hexadecimal.

Table 6.6 shows the transformation of the binary output of the comparators into hexadecimal code, as the addresses, and the hexadecimal output of the EEPROM into binary code. The results of the conversion board have been tested using a subsection containing a small circuit of LEDs and resistors. The inputs to this circuit are the binary outputs of the EEPROM. The LEDs turn on and off giving an optical representation of the binary output of the EEPROM.

Decimal	Comparator Outputs		EEPROM Inputs			EEPROM Outputs		
	Mod 11	Mod 6	Binary	Hex		Hex	Binary	Angle
0	000000000	00000	00000000000000	00000	E ² P R O M	00	0000000	00
1	000000001	00001	00000000100001	00021		01	0000001	01
2	0000000011	00011	000000001100011	00063		02	0000010	02
3	00000000111	00111	0000000011100111	000E7		03	0000011	03
4	0000001111	01111	000000111101111	001EF		04	0000100	04
5	0000011111	11111	000001111111111	003FF		05	0000101	05
6	0000111111	11111	000011111111111	007FF		06	0000110	06
7	0001111111	01111	000111111101111	00FEF		07	0000111	07
8	0011111111	00111	001111111100111	01FE7		08	0001000	08
9	0111111111	00011	011111111100011	03FE3		09	0001001	09
10	1111111111	00001	111111111100001	07FE1		0A	0001010	10
11	1111111111	00000	111111111100000	07FE0		0B	0001011	11
12	0111111111	00000	011111111100000	03FE0		0C	0001100	12
13	0011111111	00001	001111111100001	01FE1		0D	0001101	13
14	0001111111	00011	000111111100011	00FE3		0E	0001110	14
15	0000111111	00111	000011111100111	007E7		0F	0001111	15
16	0000011111	01111	000001111101111	003EF		10	0010000	16
17	0000001111	11111	000000111111111	001FF		11	0010001	17
18	0000000111	11111	000000011111111	000FF		12	0010010	18
19	0000000011	01111	000000001101111	0006F		13	0010011	19
20	0000000001	00111	000000000100111	00027		14	0010100	20
21	0000000000	00011	000000000000011	00003		15	0010101	21
22	0000000000	00001	000000000000001	00001		16	0010110	22
23	0000000001	00000	000000000100000	00020		17	0010111	23
24	0000000011	00000	000000001100000	00060		18	0011000	24
25	0000000111	00001	000000011100001	000E1		19	0011001	25
26	0000001111	00011	000000111100011	001E3		1A	0011010	26
27	0000011111	00111	000001111100111	003E7		1B	0011011	27
28	0000111111	01111	000011111101111	007EF		1C	0011100	28
29	0001111111	11111	000111111111111	00FFF		1D	0011101	29
30	0011111111	11111	001111111111111	01FFF	1E	0011110	30	

31	0111111111	01111	011111111101111	03FEF	E ² P R O M	1F	0011111	31
32	1111111111	00111	111111111100111	07FE7		20	0100000	32
33	1111111111	00011	111111111100011	07FE3		21	0100001	33
34	0111111111	00001	011111111100001	03FE1		22	0100010	34
35	0011111111	00000	001111111100000	01FE0		23	0100011	35
36	0001111111	00000	000111111100000	00FE0		24	0100100	36
37	0000111111	00001	000011111100001	007E1		25	0100101	37
38	0000011111	00011	000001111100011	003E3		26	0100110	38
39	0000001111	00111	000000111100111	001E7		27	0100111	39
40	0000000111	01111	000000011101111	000EF		28	0101000	40
41	0000000011	11111	000000001111111	0007F		29	0101001	41
42	0000000001	11111	000000000111111	0003F		2A	0101010	42
43	0000000000	01111	000000000001111	0000F		2B	0101011	43
44	0000000000	00111	000000000000111	00007		2C	0101100	44
45	0000000001	00011	000000000100011	00023		2D	0101101	45
46	0000000011	00001	00000000100001	00061		2E	0101110	46
47	0000000111	00000	00000001100000	000E0		2F	0101111	47
48	0000001111	00000	00000011100000	001E0		30	0110000	48
49	0000011111	00001	00000111100001	003E1		31	0110001	49
50	0000111111	00011	00001111100011	007E3		32	0110010	50
51	0001111111	00111	00011111100111	00FE7		33	0110011	51
52	0011111111	01111	00111111101111	01FEF		34	0110100	52
53	0111111111	11111	011111111111111	03FFF		35	0110101	53
54	1111111111	11111	111111111111111	07FFF		36	0110110	54
55	1111111111	01111	111111111011111	07FEF		37	0110111	55
56	0111111111	00111	011111111001111	03FE7		38	0111000	56
57	0011111111	00011	001111111000111	01FE3		39	0111001	57
58	0001111111	00001	000111111000011	00FE1		3A	0111010	58
59	0000111111	00000	000011111000000	007E0		3B	0111011	59
60	0000011111	00000	000001111000000	003E0		3C	0111100	60
61	0000001111	00001	000000111000001	001E1		3D	0111101	61
62	0000000111	00011	000000011000011	000E3		3E	0111110	62
63	0000000011	00111	000000001001111	00067		3F	0111111	63
64	0000000001	01111	000000000101111	0002F		40	1000000	64
65	0000000000	11111	000000000011111	0001F		41	1000001	65

Table 6.6: Transformation of binary to hexadecimal code and vice versa.

In this Chapter, the design and fabrication of each individual component of the antenna architecture has been presented. In the next Chapter, the simulation results are going to be analyzed.

VII. SIMULATION RESULTS

Before proceeding to take the experimental results of the array antenna response, it is not only useful but also necessary to estimate the ideal results of the array. The ideal case comes from the theory and needs to be compared to the experimental results as they are obtained in the chamber.

The waveform of the AF or that of the mixer output voltage couldn't be used directly by the OSNS code. It has to be processed through the quantization procedure. The mixer output voltage for each pair of elements $\{(1,3), (1,2)\}$ corresponding to modulus $m_1=6$ and $m_2=11$ respectively are shown in Figures 7.1 and 7.2. In the second plot of each figure we can observe the OSNS quantization code for each channel; i.e. the comparator states within each modulus.

The number of threshold levels (or the number of comparators in the "on" state) in each channel depends on the modulus m_i that is being considered and is given by m_i-1 . So, the number of comparators for *mod6* is five (5) and for *mod11* is ten (10), as shown in Figures 7.1 and 7.2. The output for each comparator state individually for $m_1=6$ is shown in Figure 7.3, and the comparator outputs for $m_2=11$ are given in Figures 7.4 and 7.5.

The instantaneous Resolved Direction of Arrival or the antenna transfer function is obtained if we combine the comparator states from each channel.

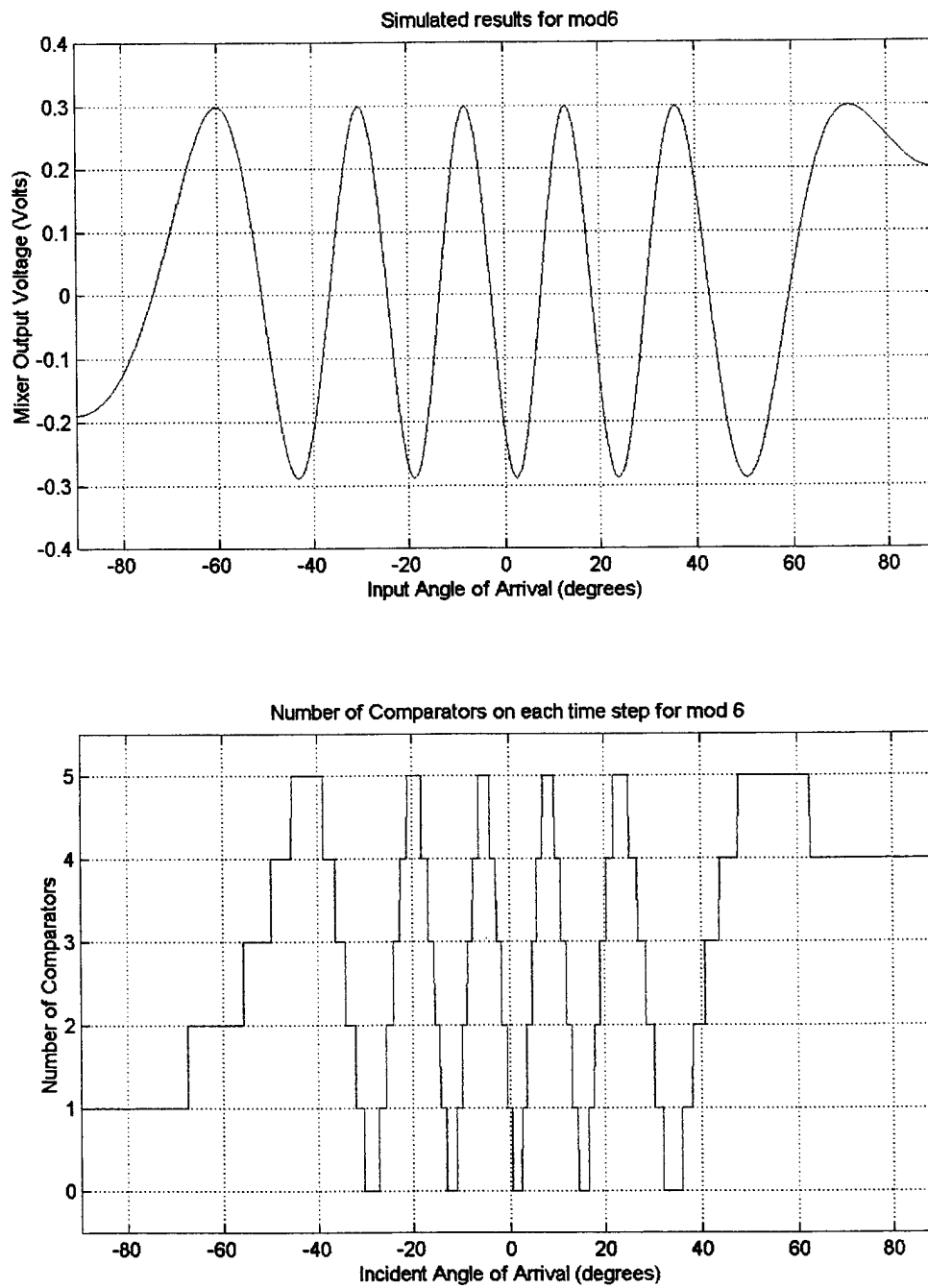


Figure 7.1: Mixer Output Voltage and the OSNS Quantization Code for the pair of elements (1,3) corresponding to modulus $m_l=6$.

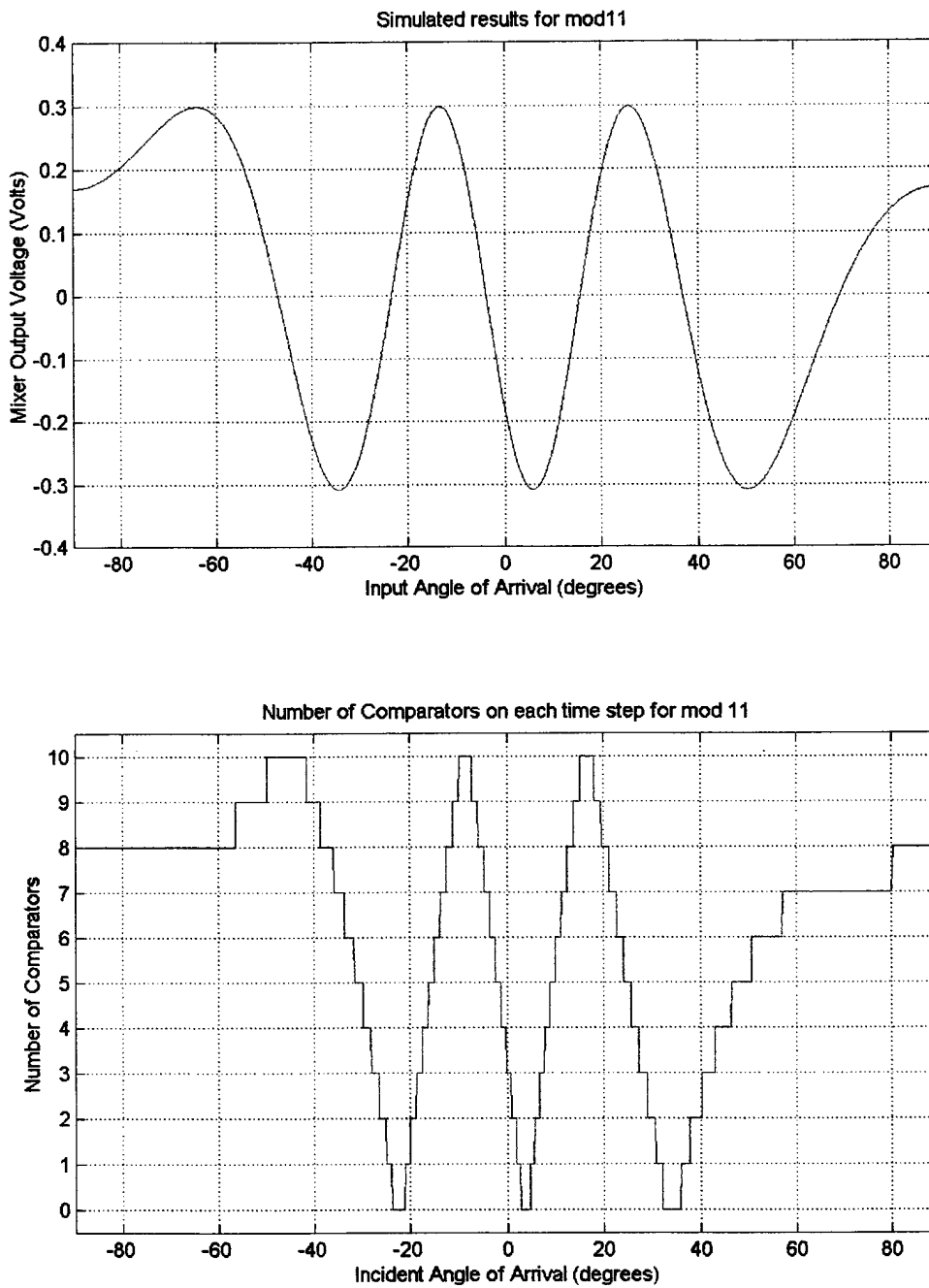


Figure 7.2: Mixer Output Voltage and the OSNS Quantization Code for the pair of elements (1,2) corresponding to modulus $m_2=11$.

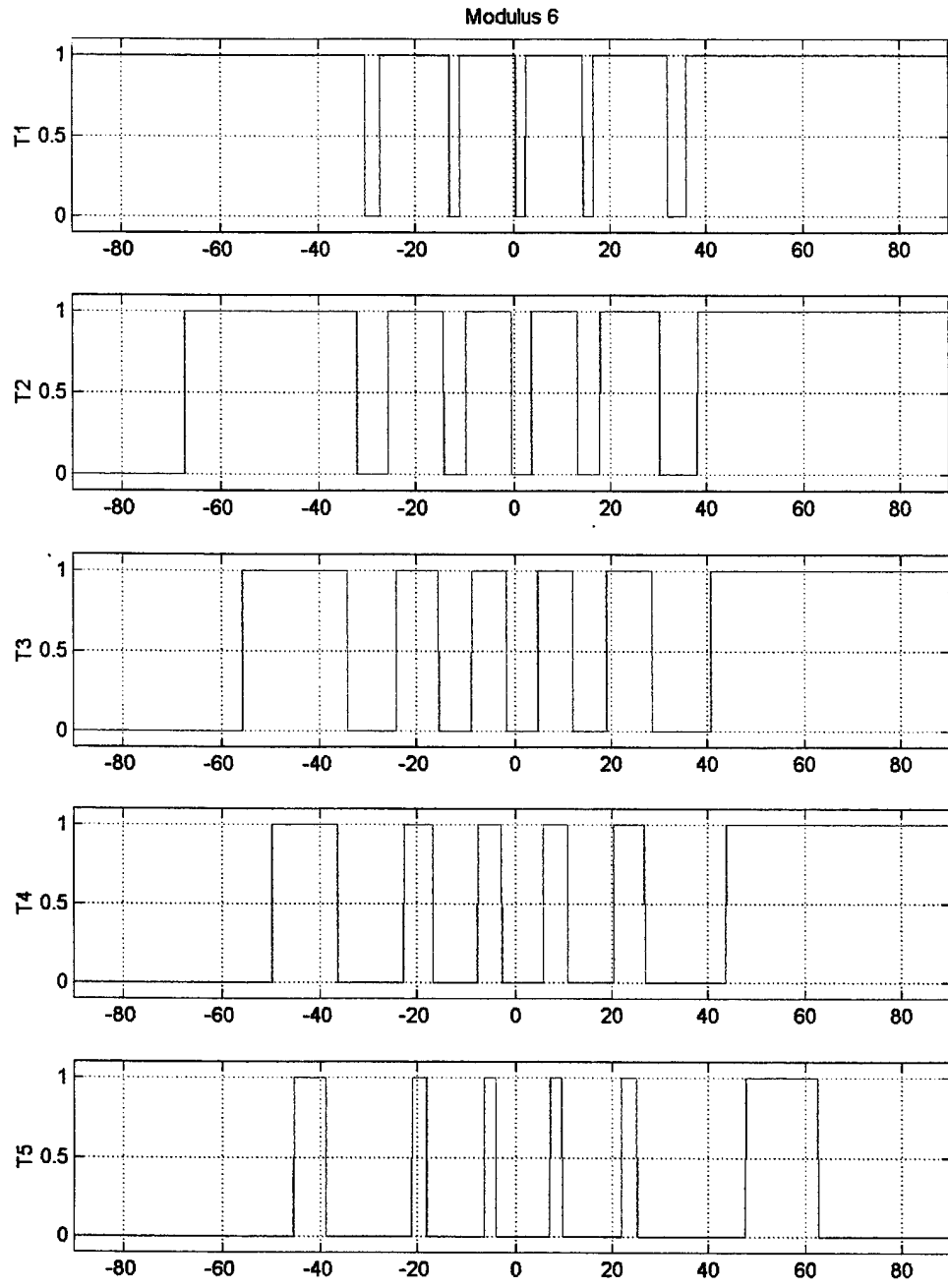


Figure 7.3: Comparator Outputs corresponding to modulus $m_1=6$
(thresholds T1 – T5).

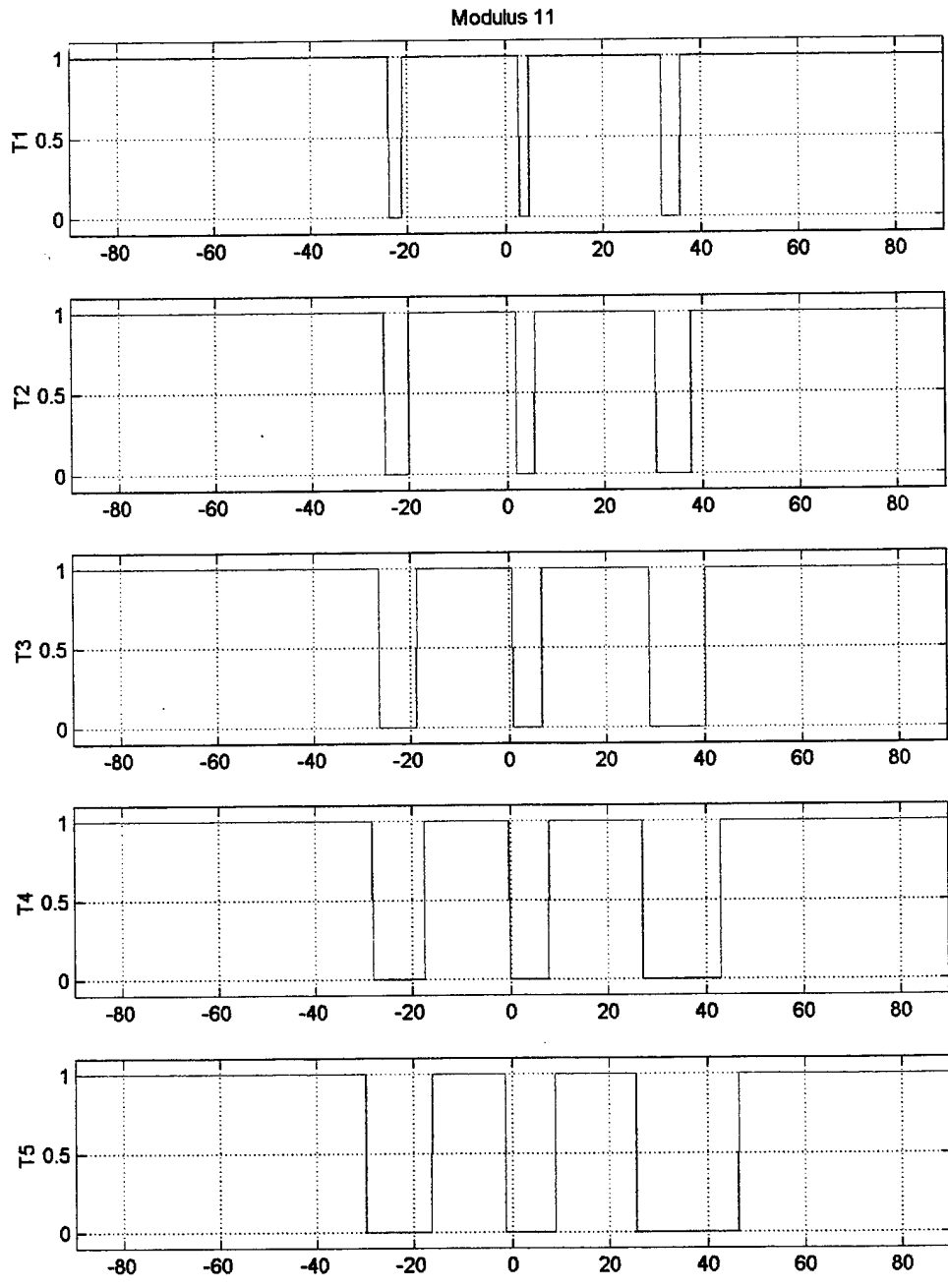


Figure 7.4: Comparator Outputs corresponding to modulus $m_2=11$
(thresholds T1 – T5).

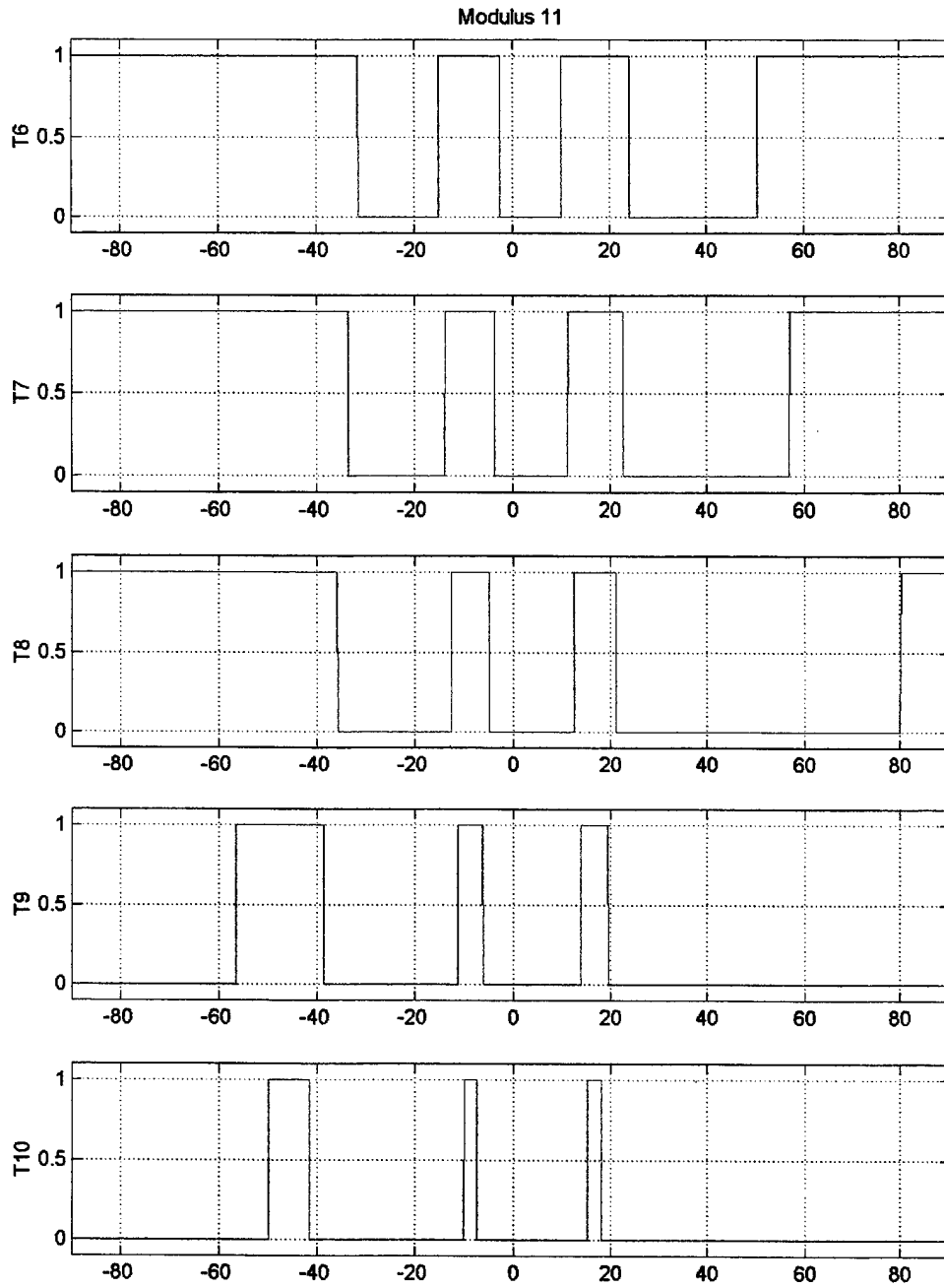


Figure 7.5: Comparator Outputs corresponding to modulus $m_2=11$
(thresholds T6 – T10).

Figure 7.6 shows the simulated transfer function of the array antenna having the EF included. A number of errors appear in this plot. These errors occur when the input direction of arrival occurs about a code transition point. At this point some of the comparators switch as they should but some may not. This results in a large error in the resolution DOA. These errors or “glitches” can however be isolated and corrected through interpolation signal processing. We can also decrease the field of view ($-50^\circ < \phi < 50^\circ$). As a final result of the simulation analysis the array transfer function for the smaller interval is illustrated in Figure 7.7.

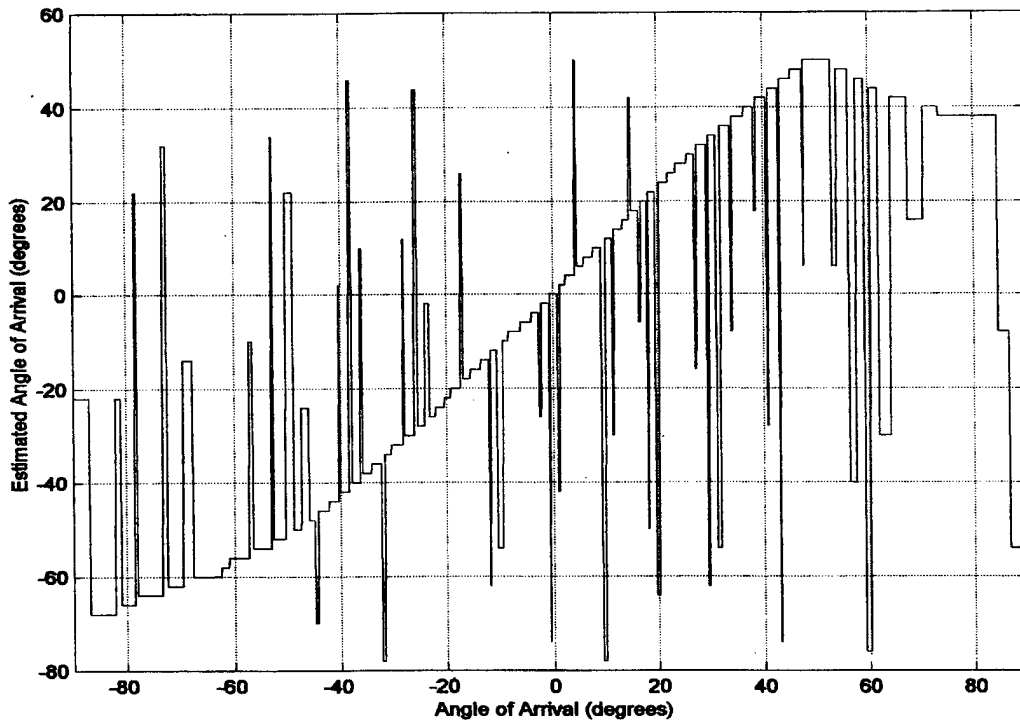


Figure 7.6: OSNS Resolved Direction of Arrival for $-90^\circ < \phi < 90^\circ$ and the effect of the element factor (EF) on the array antenna transfer function.

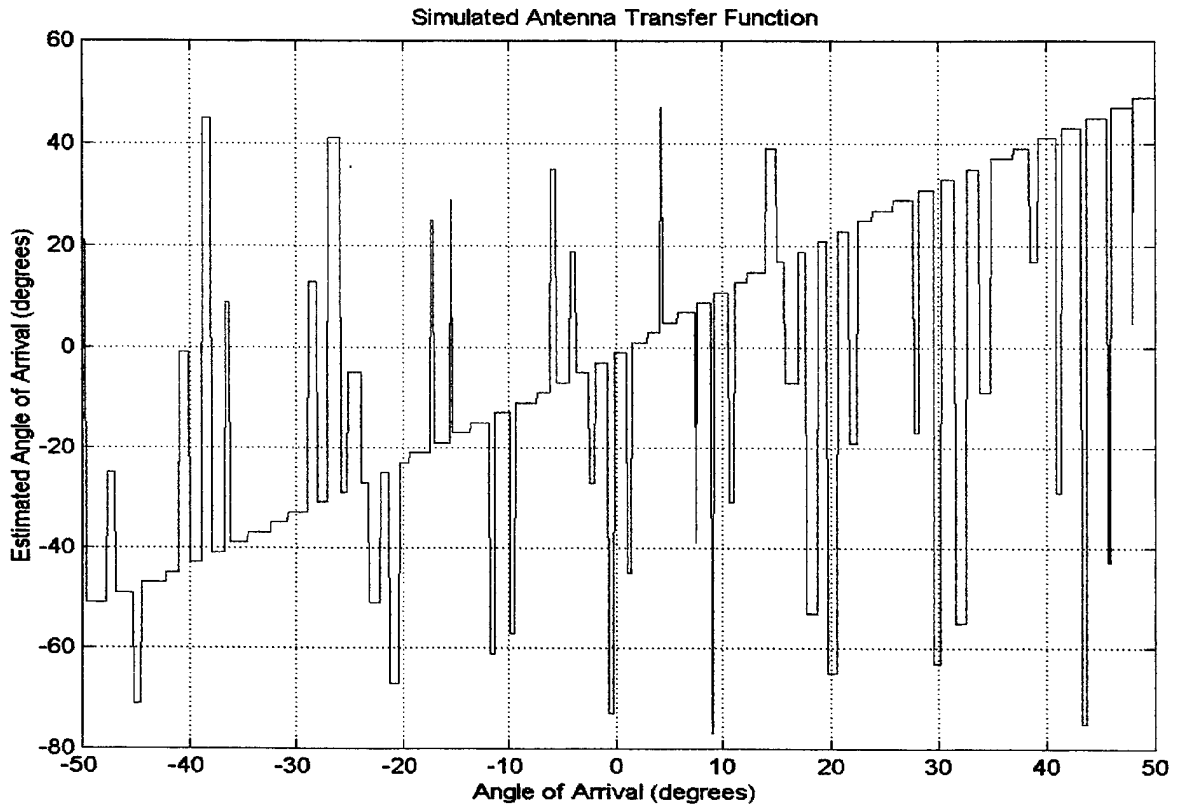


Figure 7.7: Simulated Transfer Function of OSNS antenna, for interval $-50^\circ < \phi < 50^\circ$,
 using $m_1=6$ and $m_2=11$.

VIII. EXPERIMENTAL RESULTS & COMPARISON WITH THE THEORETICAL ONES

A. MIXER OUTPUT

Using the anechoic chamber facility at the Naval Postgraduate School, antenna pattern measurements were taken for each pair of elements. The experimental measurements of the mixer output voltages response for both channels, are shown in Figure 8.1. The similarity of the experimental results to the simulated folding waveforms IS shown in Figure 8.2 for channel 1 ($m_1 = 6$) and in Figure 8.3 for channel 2 ($m_2 = 11$).

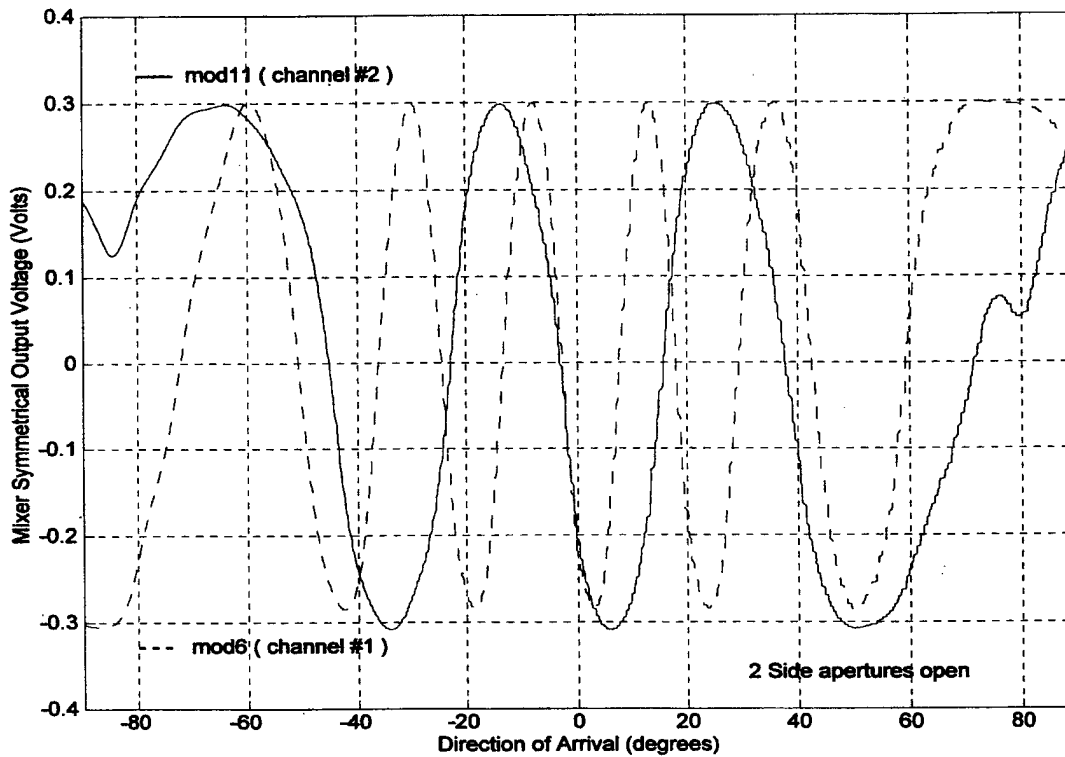


Figure 8.1: Experimental Measurements of the response of both channels.

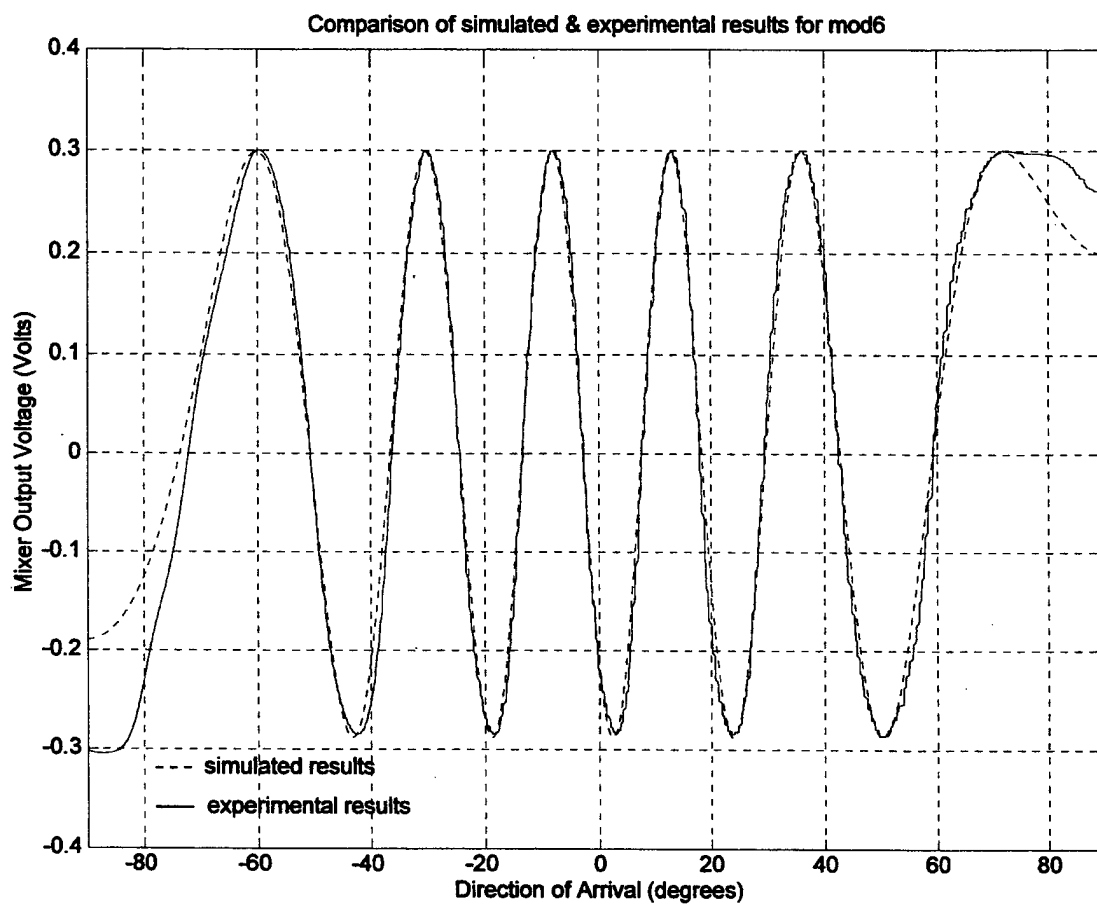


Figure 8.2: Experimental and simulated folding waveforms using channel 1 ($m_1 = 6$).

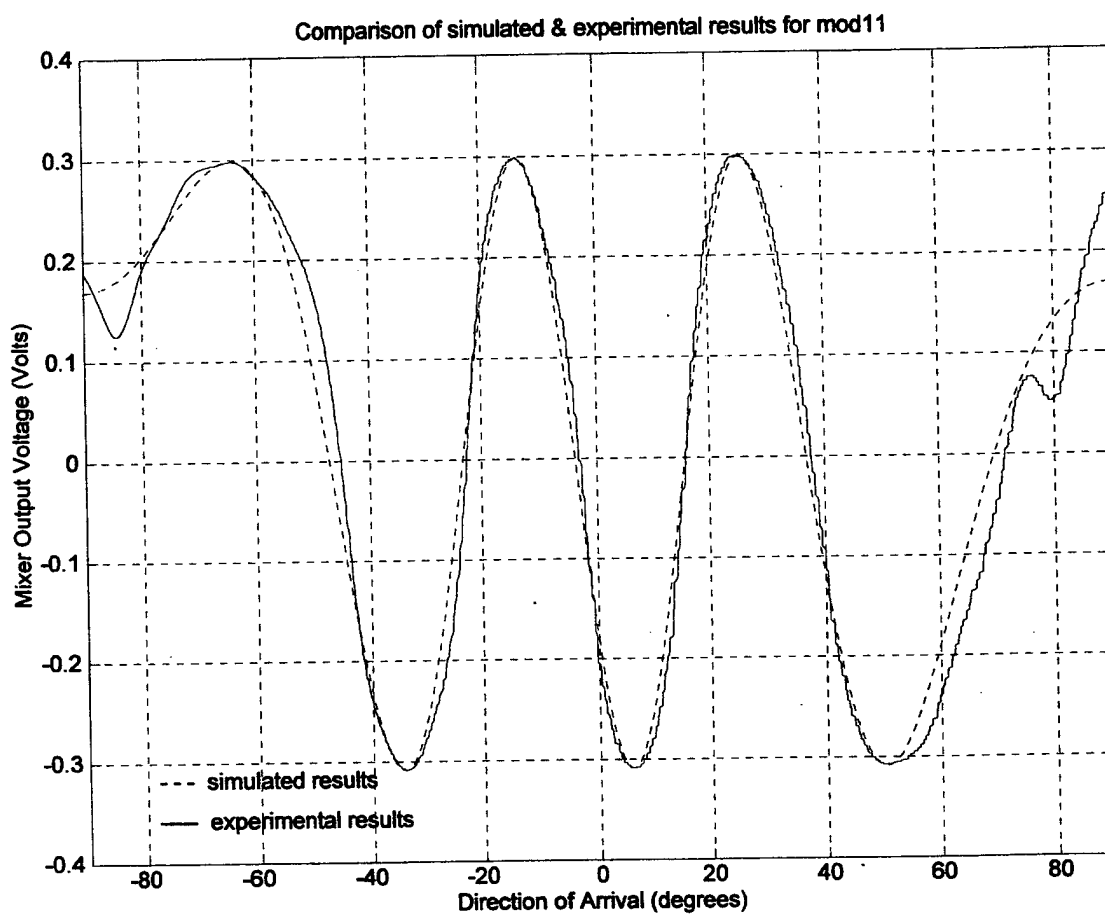


Figure 8.3: Experimental and simulated folding waveforms using channel 2 ($m_2 = 11$).

The differences between the experimental results and the simulated ones for angles close to the normal of the array antenna are very small. The major difference between the experimental results and the simulated ones is at wide angles due to the reflection and scattering from the edges of the ground plane. These differences are highlighted as shown in Figure 8.4 ($m_1 = 6$) and in Figure 8.5 ($m_2 = 11$). These plots show the response of the arrays at both edges of the ground plane for various absorber and edge waveguide configurations. The element patterns of the open-ended waveguides cause the mutual coupling due to the non-periodic spacing of the elements.

The corresponding experimental transfer function of the array antenna is shown in Figure 8.6, using the smaller interval ($-50^\circ < \theta < 50^\circ$). These results show only the performance of the antenna array with all the subsequent processing (e.g. comparators, EEPROM, etc.) done using a computer. The encoding errors in Figure 7.7 are also present in the experimental results. They do, however, occur with different amplitudes and positions within the DOA due to the differences with phase response in each channel. It must be emphasized that the encoding errors are typical and are correctable.

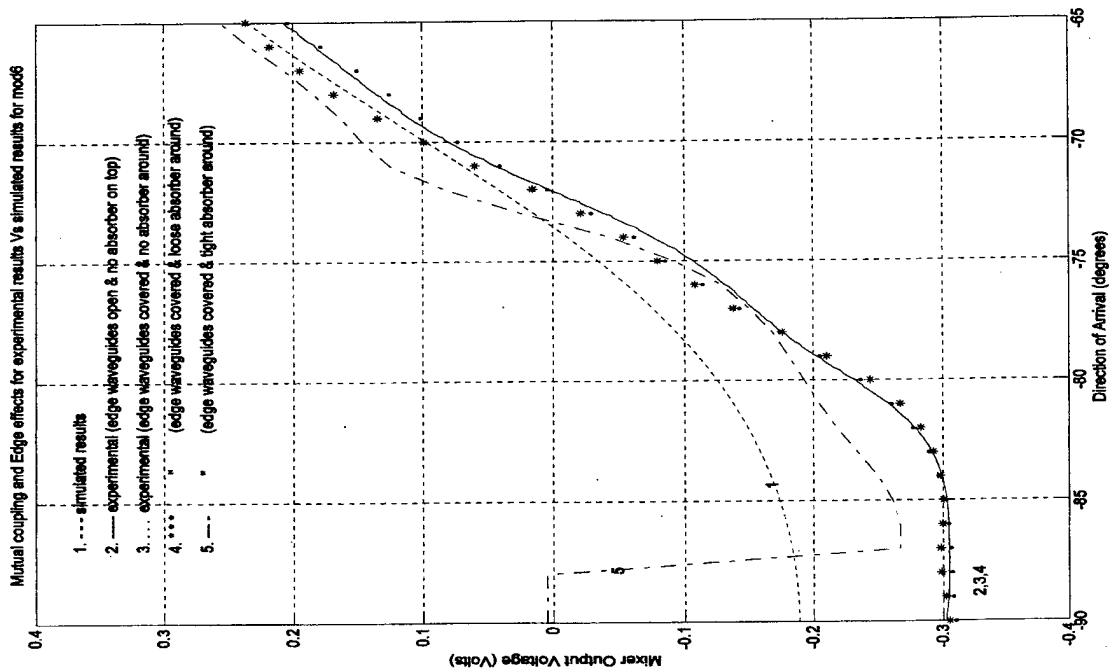
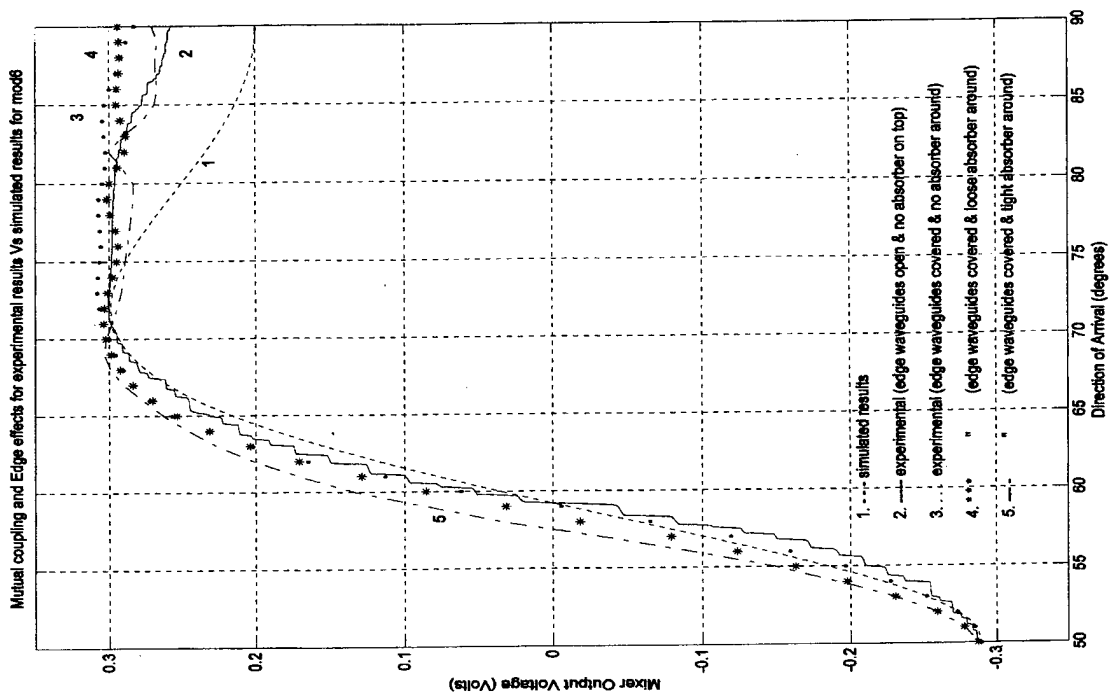


Figure 8.4: Wide angle experimental results due to edge effects for $m_1 = 6$.

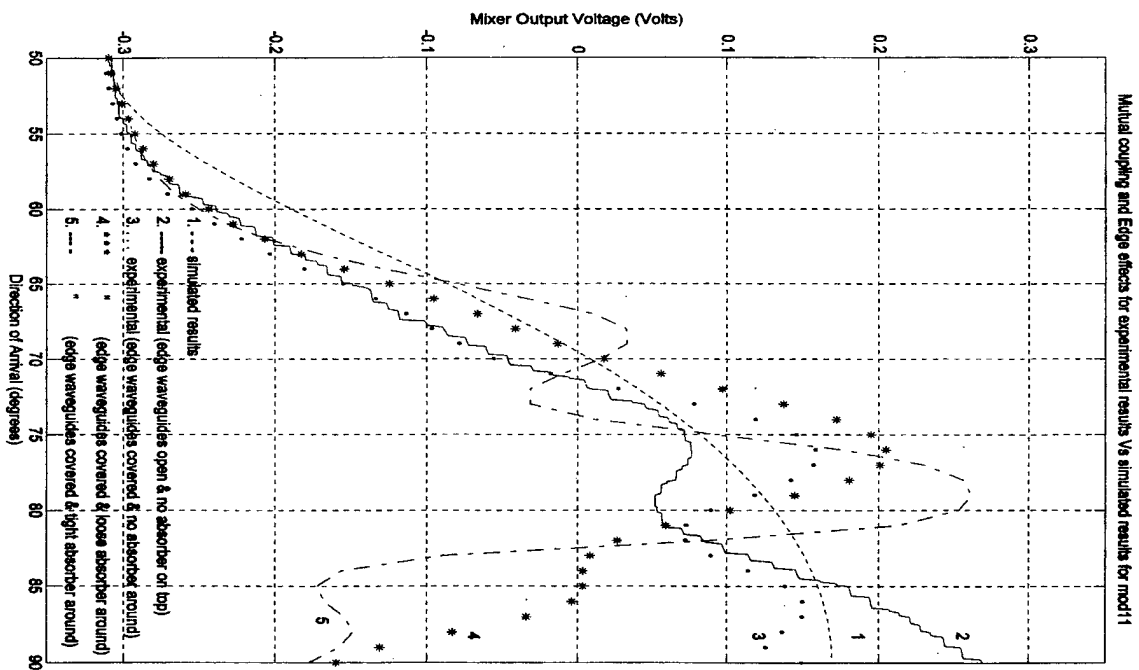
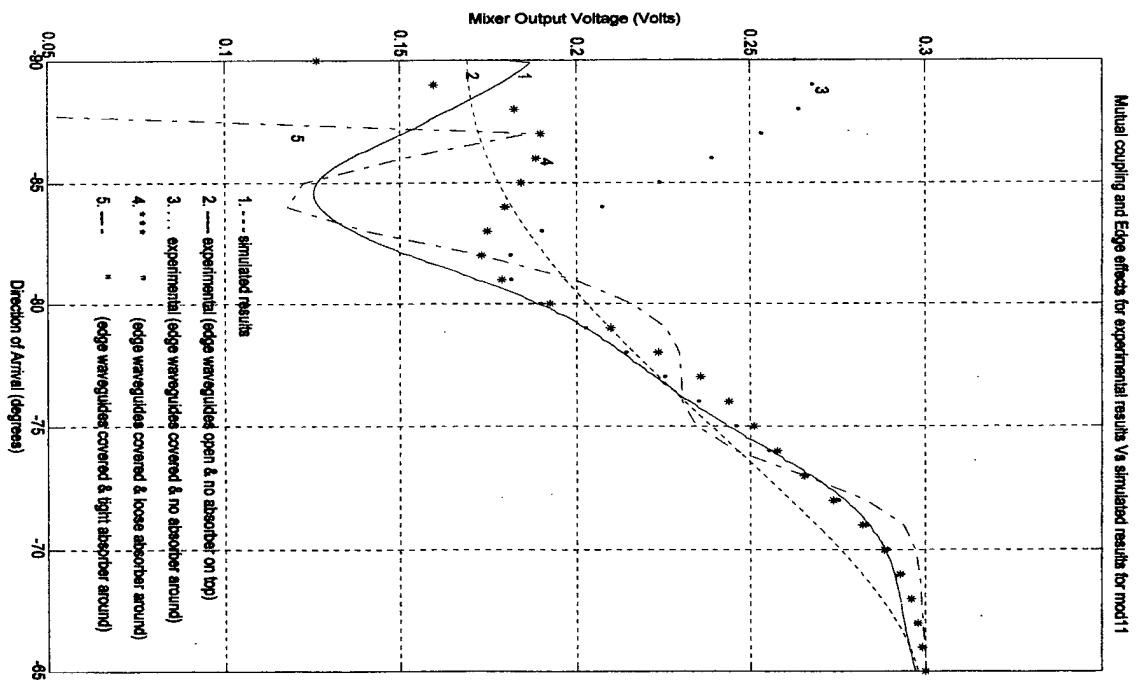


Figure 8.5: Wide angle experimental results due to mutual coupling and edge effects for

$$m_2 = 11.$$

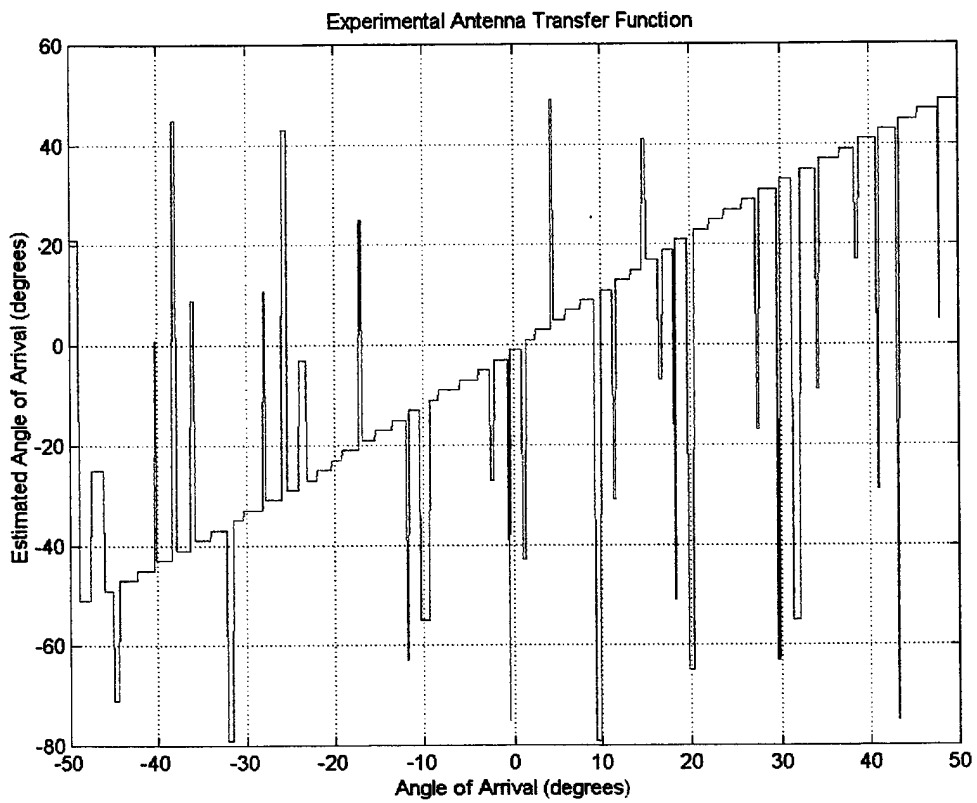


Figure 8.6: Experimental antenna Transfer Function, using computer code.

B. SUMMING AMPLIFIER OUTPUT

Continuing with the other components of the construction, the output voltages of the summing amplifier, for the two channels, are shown in Figure 8.7. Note the shifting that has been done to obtain the desired input voltage to the comparators and the amplification to spread the threshold levels for better resolution between them.

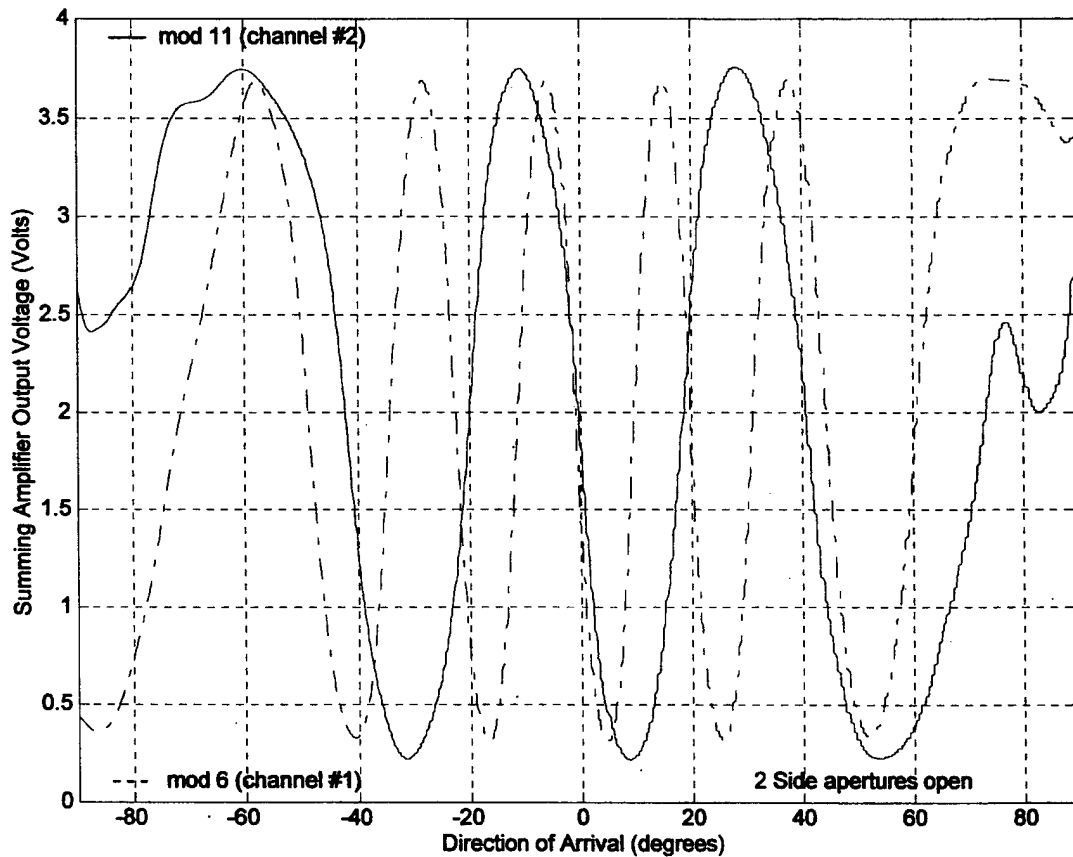


Figure 8.7: Summing Amplifier's Output Voltage.

C. A/D CONVERSION OUTPUT

The logic outputs of the comparators are addressed to the EEPROM. Using the predetermined program in the EEPROM, these values are mapped. The 7-bit word outputs from the EEPROM are transferred, through the DI/O board, to a LabVIEW VI program to get the experimental transfer function of the array antenna, as shown in Figure 8.8.

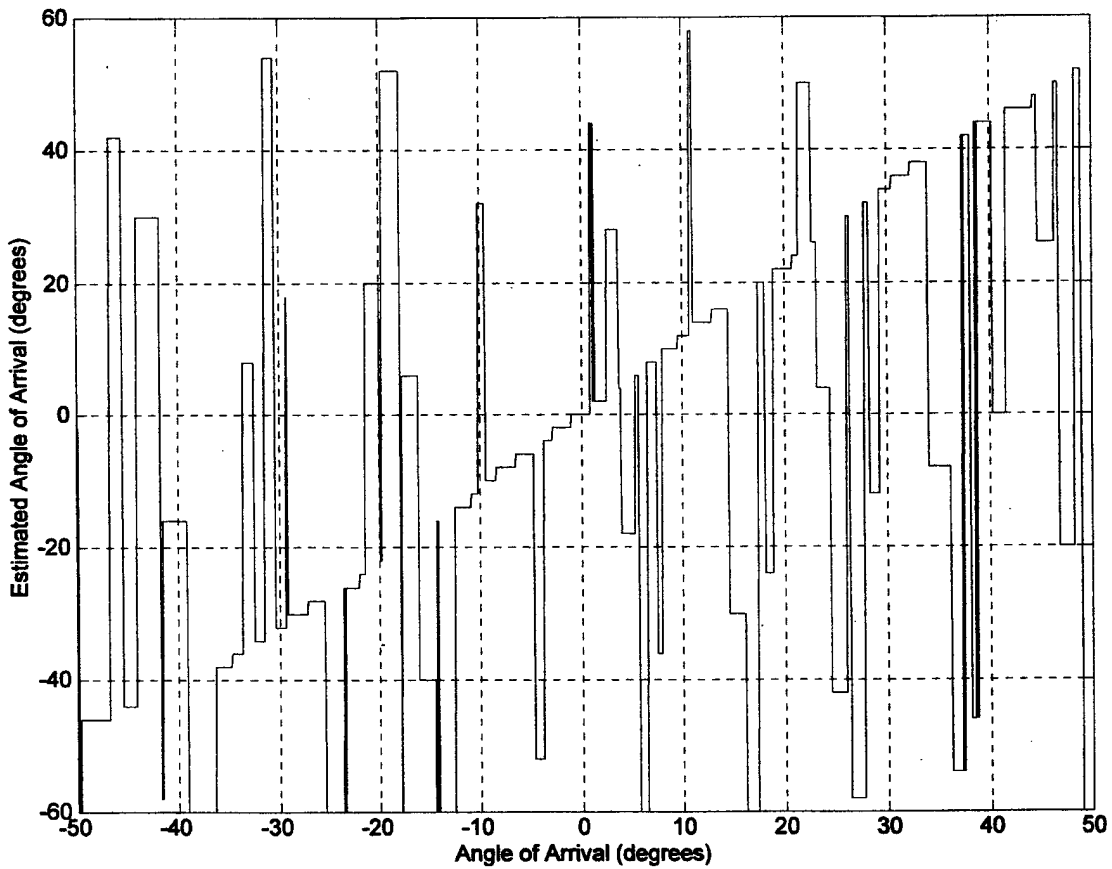


Figure 8.8: Experimental antenna Transfer Function.

IX. SUMMARY AND CONCLUSIONS

In this thesis, a new, phase-sampled direction finding architecture based on the optimum symmetrical number system has been designed, fabricated, and tested for high angular resolution of the direction of arrival of the incident electromagnetic wave. Three rectangular waveguide antenna elements mounted on a ground plane have been used, forming two pairs (channels) with the first element shared by each one of the other elements playing the role of the reference element. The design of an OSNS array is described by the equations

$$M = \prod_{i=1}^N m_i \qquad d_i = n_i \frac{\lambda}{2} = \left(\frac{M}{2m_i} \right) \frac{\lambda}{2}$$
$$n_i = \frac{M}{2m_i} \qquad r = \frac{FOV}{M},$$

providing the dynamic range (DR) M , the folding period n_i , the inter-element spacing d_i , and the spatial resolution r , respectively. All of the above variables (n_i , d_i , r) are determined by the dynamic range M . Dynamic range M can be increased by

1. increasing the number of moduli, or
2. increasing the values of the individual moduli.

If we need to keep the antenna size as small as possible, i.e. without adding antenna elements, implies that it is necessary to increase the values of the individual moduli, since m_i , in the DR equation is equivalent to a channel.

The spatial resolution is commonly expressed in bits, B . Thus, the equivalent number of bit resolution is obtained from $M=2^B$.

The inter-element spacing is specified in equation

$$d_i = n_i \frac{\lambda}{2} = \left(\frac{M}{2m_i} \right) \frac{\lambda}{2}.$$

Large m_i results in small spacing. In general, as m_i decreases, the channel spacing increases but the number of comparators decreases, given by m_i-1 .

The basic tradeoffs, which also form the advantages of the OSNS concept, are illustrated in Figure 9.1, for two and three channel arrays. The solid line is classical Rayleigh resolution limit, λ/d_{\max} , where d_{\max} is the distance between the farthest elements in the array. Each circle represents an OSNS array design based on a set of two (for $N=2$) or three (for $N=3$) relatively prime integers less than 50, like in our set of moduli (6,11). The appeal the OSNS architecture is its flexibility and ability to provide high resolution with as few as three closely spaced elements. Even finer spatial resolution can be obtained for shorter baselines when integers greater than 50 are included. In practice, the element spacings will be limited by the size of the antenna elements themselves.

There are three major advantages of the OSNS DF architecture. First, it has a wide instantaneous field of view that is only limited by the receiving element pattern edge effect. The DF process does not require any antenna steering or beam scanning. This is critical

for intercepting low probability of intercept signals. Second, the architecture is capable of wideband operation. The transmission lines incorporated in the feed do not have to compensate for space delays as they do in many scanning arrays. Therefore the line lengths can be kept short. Finally, the OSNS architecture has the ability to provide high resolution DF with as few as three closely spaced elements, which can be arranged in a number of possible configurations. In some applications element placement at certain locations on the platform may be prohibited, in which case an alternate OSNS design could be used to provide the same unambiguous DOA resolution.

In this antenna, the outputs of each channel are mixed together using a mixer, shifted and amplified using a summing amplifier, and phase analyzed using a ladder of comparators. The experimental results obtained from an EEPROM in the anechoic chamber compared with the simulated ones and they have been found similar except for some small differences. The definite actual ground plane compared with the ideal infinite one produces the edge effects for wide off boresight angles. In this case it is not possible to obtain the direction of arrival information over the entire field of view (0° to $\pm 90^\circ$). However, a smaller interval is available (from 0° to $\pm 50^\circ$), where the experimental and the simulated results are identical.

The antenna transfer function has a lot of similarities with the simulated one, except for the errors, which appear when the input direction of arrival occurs about a code transition point. At this point some of the comparators switch, as they should, but some don't. The main reason that some comparators fail to switch at the right point is the thermal noise they face. The failure of switching at the right threshold level produces the

spikes (“glitches”), since the mapping process is very sensitive for these changes. Even a failure of a single comparator can produce a large ambiguity in the resolved direction of arrival.

There are some solutions for the previous problems. These “glitches” can be isolated and corrected through interpolation signal processing. Another approach for correcting some of these errors is the parity checking, using parity check codes. This last process affects the number of comparators in the architecture and another construction has to be obtained for getting the desired results. This process can provide another field of future research in this new array interferometer architecture.

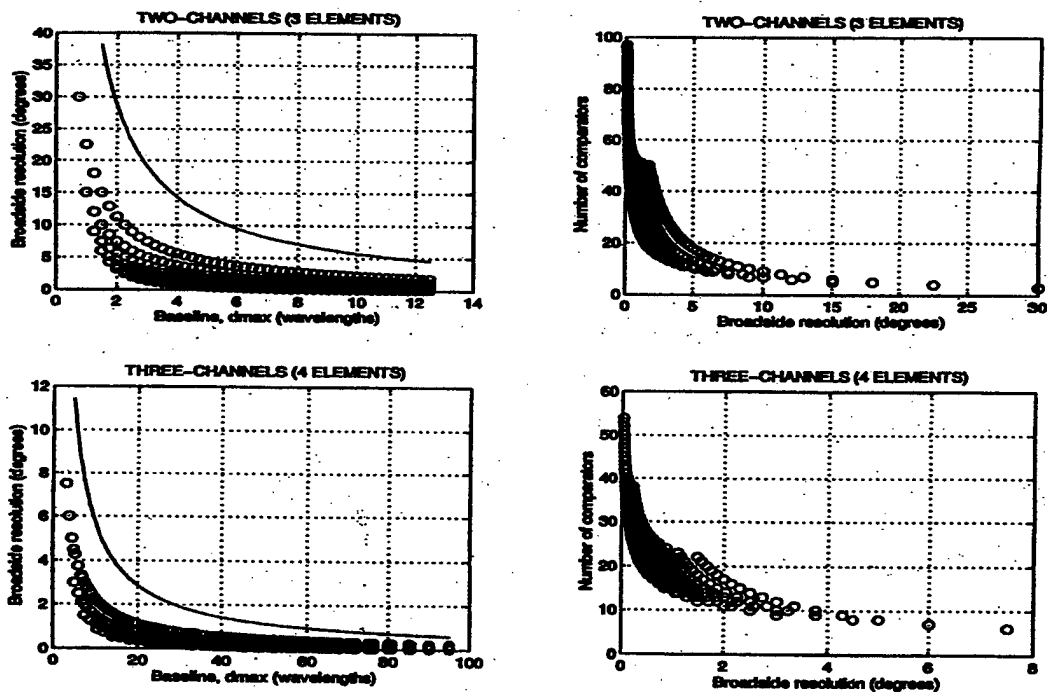


Figure 9.1: Tradeoffs for two and three channel arrays for combinations of relatively prime integers less than 50. Each circle represents a unique OSNS configuration. [Ref. 10]

APPENDIX A. MATLAB CODES

Program 1

```
% This program "OSNS6.m" calculates the simulated results (array factor, phase delay,
% mixer output voltage) of the array for the moduli set (6,11) and by loading the data
% from the measurements in the anechoic chamber it compares them together.
% Check OSNS design with mixers vs. phase and array output results.
% Two element arrays assumed.
% m = modulus; d = spacing (m); f = frequency

clear
f=8.5e9; c=3e8; wavl=c/f;
k=2*pi/wavl;
rad=pi/180;
modscale6=(0.2863+ 0.3005)/2;

% number of moduli in array design and their values
mm=[6 11]; nm=length(mm);
disp('moduli are: '),disp(mm)

% specify a modulus to plot
m=input('enter a modulus: ');

% from design equations
M=prod(mm);
nf=M/2/m;
%dw=nf; % old design for phase differences
dw=nf/2; % new design for mixer outputs
d=dw*wavl;
args=k*d*sin(-pi/2);

% start, stop, increment angles
start=-90; stop=90; inc=0.1;
N=floor((stop-start)/inc)+1;
for n=1:N
    thd(n)=start+(n-1)*inc;
    thr=thd(n)*rad;
    arg(n)=k*d*sin(thr);

% array factor (normalized coupler output)
af(n)=2;
faz(n)=0;
    aa=arg(n)-args;
    if abs(aa)>.0001
```

```

    af(n)=sin(aa)/sin(aa/2);
    faz(n)=atan2(1e-10,af(n));
end

% mixer output unscaled
mx1(n)=cos(arg(n)-args-55*(pi/180))
mx2(n)=flipud(mx1(n));
% mixer output scaled
mx(n)=modscale6*cos(arg(n)-args-131.5*(pi/180))+(0.2986-0.2934);

% wave front phase difference
ph(n)=mod(arg(n),2*pi);
u(n)=arg(n)/k/d;
end

% Simulated results for the channel 1 (mod6) of the OSNS antenna
figure(1)
% Generates the Array Factor of the antenna
subplot(221)
plot(thd,af)
xlabel('theta (deg)')
ylabel('array factor'),grid
axis([-90,90,-2,2])
title([' bins = ',num2str(M),' modulus = ',num2str(m),' folds = ',num2str(nf)])
% Calculates the Space delay as a function of theta in degrees
subplot(222)
plot(thd,ph/rad)
xlabel('theta (deg)')
ylabel('space delay (deg)'),grid
axis([-90,90,0,360])
title(['frequency = ',num2str(f/1e9),' GHz', ' spacing = ',num2str(d/.0254),' in '])
% Calculates the Mixer Output Voltage
subplot(223)
plot(thd,mx2)
xlabel('theta (deg)')
ylabel('mixer voltage'),grid
axis([-90,90,-1,1])
% Calculates the Space delay as a function of sin(theta) in degrees
subplot(224)
plot(u,ph/rad)
xlabel('sin(theta)')
ylabel('space delay (deg)'),grid
axis([-1,1,0,360])

% load the data from the experimental measurements in the anechoic chamber
load df5.dat

```

```

load df1.dat
load df2.dat
load df3.dat

both6=[thd' mx'];

save simu6.dat both6 -ascii

% Compares the simulated & the experimental results
figure(2)
plot(df5(:,3),df5(:,4),'b-')
hold on
plot(thd,mx,'b:')
xlabel('Direction of Arrival (degrees)')
ylabel('Mixer Output Voltage (Volts)'),grid
hold off
title(['Comparison of simulated & experimental results for mod',num2str(m),])
text(-78,-.32,'- - - experimental results')
text(-78,-.36,'----- simulated results')
axis([-90,90,-.4,.4])

% Illustrates the mutual coupling and Edge effects for experimental results Vs simulated
results for angles (-90 to -65)
figure(3)
plot(df5(:,3),df5(:,4),'b-') % 2. ---- experimental results (edge waveguides open & no
absorber on top)
hold on
plot(df3(:,3),df3(:,4),'b-') % 5. --- - " " (edge waveguides covered & tight
absorber around)
hold on
plot(df2(:,3),df2(:,4),'b*') % 4. * * * " " (edge waveguides covered & loose
absorber around)
hold on
plot(df1(:,3),df1(:,4),'b.') % 3. . . . experimental results (edge waveguides covered & no
absorber around)
hold on
plot(thd,mx,'b:') % 1. - - - simulated results
xlabel('Direction of Arrival (degrees)')
ylabel('Mixer Output Voltage (Volts)'), grid
hold off
title(['Mutual coupling and Edge effects for experimental results Vs simulated results for
mod',num2str(m),])
text(-87,.365,'1. - - - simulated results')
text(-87,.34,'2. ----- experimental (edge waveguides open & no absorber on top)')
text(-87,.315,'3. . . . experimental (edge waveguides covered & no absorber around)')
text(-87,.29,'4. * * * " (edge waveguides covered & loose absorber around)')

```

```

text(-87,.265, '5. --- -      "      (edge waveguides covered & tight absorber around)')
text(-89,-.33, '2,3,4')
text(-84.5,-.17, '1')
text(-88,-.05, '5')
axis([-90,-65,-.4,.4])
orient tall

% Illustrates the mutual coupling and Edge effects for experimental results Vs simulated
results for angles (50 to 90 degrees)
figure(4)
plot(df5(:,3),df5(:,4),'b-') % 2. ----- experimental results (edge waveguides open & no
absorber on top)
hold on
plot(df3(:,3),df3(:,4),'b-') % 5. --- -      "      "      (edge waveguides covered & tight
absorber around)
hold on
plot(df2(:,3),df2(:,4),'b*') % 4. * * *      "      "      (edge waveguides covered & loose
absorber around)
hold on
plot(df1(:,3),df1(:,4),'b.') % 3. . . . experimental results (edge waveguides covered & no
absorber around)
hold on
plot(thd,mx,'b:') % 1. - - - simulated results
xlabel('Direction of Arrival (degrees)')
ylabel('Mixer Output Voltage (Volts)'), grid
hold off
title(['Mutual coupling and Edge effects for experimental results Vs simulated results for
mod',num2str(m),'])
text(58,-.21, '1. - - - simulated results')
text(58,-.235, '2. ----- experimental (edge waveguides open & no absorber on top)')
text(58,-.26, '3. . . . experimental (edge waveguides covered & no absorber around)')
text(58,-.285, '4. * * *      "      (edge waveguides covered & loose absorber around)')
text(58,-.31, '5. --- -      "      (edge waveguides covered & tight absorber around)')
text(88,.245, '2')
text(81,.23, '1')
text(84,.32, '3')
text(88,.31, '4')
text(58,.075, '5')
axis([50,90,-.35,.35])
orient tall

```

Program 2

```
% The previous program itself is organized for modulus 6, but it can be used for modulus
% 11, as well, by changing the appropriate parameters (columns) for modulus 11
% (e.g. from modulus 6          plot(df5(:,3),df5(:,4),'b-')
% change to                    plot(df5(:,1),df5(:,2),'b-')
% also you have to take into account the following changes

modscale11=(0.2986+0.3087)/2;

% mixer output unscaled
mx1(n)=cos(arg(n)-args-55*(pi/180));
% mixer output
mx(n)=modscale11*cos(arg(n)-args-55*(pi/180))-(0.3036-0.2986);

both11=[thd' mx'];
save simul1.dat both11 -ascii
```

Program 3

```
% This program measures the response of the Low Noise Amplifiers

% Input Power to the Amplifiers
X = -50:2:-20;
% Output Power form the Amplifier 450873
Y1 = [-14.05,-13.22,-12.09,-10.73,-9.21,-7.53,-5.88,-4.0,-2.13,-
0.27,1.56,3.21,4.80,6.10,6.93,7.5];
% Output Power form the Amplifier 450874
Y2 = [-14.34,-13.57,-12.47,-11.15,-9.63,-7.97,-6.32,-4.47,-2.60,-
0.75,1.04,2.60,4.11,5.24,6.0,6.68];
% Output Power form the Amplifier 450875
Y3 = [-12.11,-11.34,-10.18,-8.82,-7.32,-5.68,-4.07,-2.27,-
0.45,1.31,2.97,4.34,5.53,6.2,6.68,6.96];
% Output Power form the Amplifier 451376
Y4 = [-13.35,-12.53,-11.55,-10.11,-8.7,-7.0,-5.42,-3.58,-
1.74,0.04,1.7,3.0,4.0,4.81,5.4,5.77];
% Output Power form the Amplifier 002
Y5 = [-10.72,-9.75,-8.48,-7.0,-5.37,-3.61,-
1.87,0.15,2.3,4.29,6.26,8.08,10.04,11.91,13.57,14.96];
% Output Power form the Amplifier 001
Y6 = [-11.02,-10.09,-8.82,-7.37,-5.75,-4.01,-2.29,-
0.27,1.71,3.69,5.66,7.51,9.47,11.38,13.07,14.57];
% Output Power form a Cascade of the Amplifiers 450873 - 451376
Y14= [-18.76,-18.76,-18.76,-18.77,-18.78,-18.78,-18.78,-18.79,-18.78,-18.75,-
18.74,-18.73,-18.72,-18.72];
```

```

% Output Power form a Cascade of the Amplifiers 450874 - 450875
Y23= [-18.54,-18.54,-18.54,-18.55,-18.56,-18.56,-18.57,-18.56,-18.55,-18.55,-18.54,-
18.53,-18.52,-18.52,-18.51,-18.51];
% Output Power form a Cascade of the Amplifiers 000 - 002
Y56= [-20.17,-20.13,-20.06,-19.95,-19.85,-19.80,-19.80,-19.79,-19.74,-19.69,-19.59,-
19.54,-19.54,-19.54,-19.53,-19.47];

% Comparison of the amplifiers (LNAs) individually and in cascades
figure(1)
plot(X, Y1, 'b', X, Y2, 'b', X, Y3, 'b', X, Y4, 'b', X, Y5, 'b--', X, Y6, 'b--',
', X, Y14, 'b+', X, Y23, 'bo', X, Y56, 'b*'), grid
title(' Transfer function of the Low Noise Amplifiers (LNAs) ')
xlabel(' Input Power ( dBm ) ')
ylabel(' Output Power ( dBm ) ')
text(-34, 6, '001-002')
text(-29, 1, '450873-450874')
text(-29, -1, '450875-451376')
text(-39, -15.5, 'Cascades 450873 - 451376 " o "')
text(-35.1, -17, '450874 - 450875 " + "')
text(-39, -22, 'Cascade 001 - 002 " * "')

```

Program 4

```

% Response of the Weigthed Summing Amplifier circuit

% load the input & the output signal values
load dc3.dat

figure(1)
plot(dc3(:,1), '-')
hold on
plot(dc3(:,2), '*')
hold off
axis([1 73 -.7 6.4])
title('Response of the Weighted Summing Amplifier (output) vs mixer output voltage (input)')
xlabel('One folding period')
ylabel('Input - Output Voltage (Vdc)')
text(6, -4, '- input signal')
text(6, 3.7, '* output signal')
grid

```

Program 5

```

%*****
% This program " osnsantsimt7.m " calculates the number of comparators in each time
% step for modulus 6 and modulus 11, both for simulated and experimental results.
% It also plots the waveform for each threshold level (for the two moduli)
% It plots the Mixer output voltage in comparison with the number of comparators for
% each time step.
% Finally, it calculates the Estimated Angle of Arrival.
% This program switches from the simulated results to the experimental ones by simply
% change (switch to %.....) the loading files, the variables, and the threshold voltages.
% The threshold voltages referred to the mixer outputs.

```

```

load simu11.dat
load simu6.dat
df1=simu11;

```

```

%load df5.dat
%df1=[df5(:,1) df5(:,2)];
%*****
point_num=1801; %1801

```

```

%comparators mod 11

```

```

for i=1:point_num

```

```

    c_m11(i,[1])=i;
    c_m11(i,[2])=0;
    c_m11(i,[3])=0;
    c_m11(i,[4])=0;
    c_m11(i,[5])=0;
    c_m11(i,[6])=0;
    c_m11(i,[7])=0;
    c_m11(i,[8])=0;
    c_m11(i,[9])=0;
    c_m11(i,[10])=0;
    c_m11(i,[11])=0;

```

```

end

```

```

% SIMULATION THRESHOLDS FOR MOD 11

```

```

t1 = -0.2983505;
t2 = -0.2734341;
t3 = -0.2260299;
t4 = -0.1632086;
t5 = -0.0864785;
t6 = -0.0009030;
t7 = 0.0867593;

```



```

t8 = 0.1685504;
t9 = 0.2386783;
t10 = 0.2829338;
% EXPERIMENTAL THRESHOLDS FOR MOD 11
%t1 = -0.300122;
%t2 = -0.277011;
%t3 = -0.233625;
%t4 = -0.165201;
%t5 = -0.040460;
%t6 = 0.050343;
%t7 = 0.149914;
%t8 = 0.212881;
%t9 = 0.264524;
%t10 = 0.289688;

for i=1:point_num

% all the data points
% c1 is the bottom comparator
% t1 is the threshold voltage for c1 etc

if (df1(i,[2]))> t1
    c_m11(i,[2]) = 1;
else
    c_m11(i,[2]) = 0;
end

if (df1(i,[2]))> t2
    c_m11(i,[3]) = 1;
else
    c_m11(i,[3]) = 0;
end

if (df1(i,[2]))> t3
    c_m11(i,[4]) = 1;
else
    c_m11(i,[4]) = 0;
end

if (df1(i,[2]))> t4
    c_m11(i,[5]) = 1;
else
    c_m11(i,[5]) = 0;
end

```

```

if (df1(i,[2]))> t5
    c_m11(i,[6]) = 1;
else
    c_m11(i,[6]) = 0;
end

if (df1(i,[2]))> t6
    c_m11(i,[7]) = 1;
else
    c_m11(i,[7]) = 0;
end

if (df1(i,[2]))> t7
    c_m11(i,[8]) = 1;
else
    c_m11(i,[8])= 0;
end

if (df1(i,[2]))> t8
    c_m11(i,[9]) = 1;
else
    c_m11(i,[9]) = 0;
end

if (df1(i,[2]))> t9
    c_m11(i,[10]) = 1;
else
    c_m11(i,[10]) = 0;
end

if (df1(i,[2]))> t10
    c_m11(i,[11]) = 1;
else
    c_m11(i,[11]) = 0;
end

end
    %encoding the thermometer code into a decimal number.
    %osns_m11 contains the number of comparators on at each time
    %step

for j=1:point_num

    A=c_m11(j,[2]);
    B=c_m11(j,[3]);
    C=c_m11(j,[4]);

```

```

D=c_m11(j,[5]);
E=c_m11(j,[6]);
F=c_m11(j,[7]);
G=c_m11(j,[8]);
H=c_m11(j,[9]);
I=c_m11(j,[10]);
J=c_m11(j,[11]);

Z=A+B+C+D+E+F+G+H+I+J;

osns_m11(j)=Z;

```

```
end
```

```

N=1801;
D=2/(N-1);
for i=1:N
    u(i)=-1+(i-1)*D;
    u1(i)=asin(u(i));
    u2(i)=u1(i)*180/pi;
end

```

```

figure(1)
subplot(2,1,1)
plot(df1(:,1),df1(:,2),'b-')
xlabel('Input Angle of Arrival (degrees)')
ylabel('Mixer Output Voltage (Volts)'),grid
title('Simulated results for mod11')
axis([-90,90,-.4,.4])
subplot(2,1,2)
plot(u2,osns_m11(:)),grid
xlabel('Incident Angle of Arrival (degrees)')
ylabel('Number of Comparators')
title('Number of Comparators on each time step for mod 11')
axis([-90 90 -0.5 10.5])
orient tall

```

```

figure(2)
subplot(5,1,1),plot(u2,c_m11(:,2)),grid,axis([-90 90 -0.1 1.1])
title('Modulus 11'),ylabel('T1'),orient tall
subplot(5,1,2),plot(u2,c_m11(:,3)),grid,axis([-90 90 -0.1 1.1])
ylabel('T2'),orient tall
subplot(5,1,3),plot(u2,c_m11(:,4)),grid,axis([-90 90 -0.1 1.1])
ylabel('T3'),orient tall
subplot(5,1,4),plot(u2,c_m11(:,5)),grid,axis([-90 90 -0.1 1.1])
ylabel('T4'),orient tall

```

```
subplot(5,1,5),plot(u2,c_m11(:,6)),grid,axis([-90 90 -0.1 1.1])
ylabel('T5'),orient tall
```

```
figure(3)
```

```
subplot(5,1,1),plot(u2,c_m11(:,7)),grid,axis([-90 90 -0.1 1.1])
```

```
title('Modulus 11'),ylabel('T6'),orient tall
```

```
subplot(5,1,2),plot(u2,c_m11(:,8)),grid,axis([-90 90 -0.1 1.1])
```

```
ylabel('T7'),orient tall
```

```
subplot(5,1,3),plot(u2,c_m11(:,9)),grid,axis([-90 90 -0.1 1.1])
```

```
ylabel('T8'),orient tall
```

```
subplot(5,1,4),plot(u2,c_m11(:,10)),grid,axis([-90 90 -0.1 1.1])
```

```
ylabel('T9'),orient tall
```

```
subplot(5,1,5),plot(u2,c_m11(:,11)),grid,axis([-90 90 -0.1 1.1])
```

```
ylabel('T10'),orient tall
```

```
%*****
```

```
clear df1
```

```
df1=simu6;
```

```
%df1=[df5(:,3) df5(:,4)];
```

```
%*****
```

```
%comparators mod 6
```

```
for i=1:point_num
```

```
    c_m6(i,[1])=i;
```

```
    c_m6(i,[2])=0;
```

```
    c_m6(i,[3])=0;
```

```
    c_m6(i,[4])=0;
```

```
    c_m6(i,[5])=0;
```

```
    c_m6(i,[6])=0;
```

```
end
```

```
% SIMULATION THRESHOLDS FOR MOD 6
```

```
t1 = -0.2557467;
```

```
t2 = -0.1601630;
```

```
t3 = -0.0182199;
```

```
t4 = 0.1293009;
```

```
t5 = 0.2513182;
```

```
% EXPERIMENTAL THRESHOLDS FOR MOD 6
```

```
%t1 = -0.258821;
```

```
%t2 = -0.187919;
```

```
%t3 = -0.013512;
```

```

%t4 = 0.143976;
%t5 = 0.268280;

for i=1:point_num

    % all the data points
    % c1 is the bottom comparator
    % t1 is the threshold voltage for c1 etc

    if (df1(i,[2]))> t1
        c_m6(i,[2]) = 1;
    else
        c_m6(i,[2]) = 0;
    end

    if (df1(i,[2]))> t2
        c_m6(i,[3]) = 1;
    else
        c_m6(i,[3]) = 0;
    end

    if (df1(i,[2]))> t3
        c_m6(i,[4]) = 1;
    else
        c_m6(i,[4]) = 0;
    end

    if (df1(i,[2]))> t4
        c_m6(i,[5]) = 1;
    else
        c_m6(i,[5]) = 0;
    end

    if (df1(i,[2]))> t5
        c_m6(i,[6]) = 1;
    else
        c_m6(i,[6]) = 0;
    end

end

%encoding the thermometer code into a decimal number.
%osns_m6 contains the number of comparators on at each time
%step

for j=1:point_num

```

```

A=c_m6(j,[2]);
B=c_m6(j,[3]);
C=c_m6(j,[4]);
D=c_m6(j,[5]);
E=c_m6(j,[6]);

```

```

Z=A+B+C+D+E;

```

```

osns_m6(j)=Z;

```

```

end

```

```

figure(4)
subplot(2,1,1)
plot(df1(:,1),df1(:,2),'b-')
xlabel('Input Angle of Arrival (degrees)')
ylabel('Mixer Output Voltage (Volts)'),grid
title('Simulated results for mod6')
axis([-90,90,-.4,.4])
subplot(2,1,2)
plot(u2,osns_m6(:),grid)
xlabel('Incident Angle of Arrival (degrees)')
ylabel('Number of Comparators')
title('Number of Comparators on each time step for m6')
axis([-90 90 -0.5 5.5])

```

```

figure(5)
subplot(5,1,1),plot(u2,c_m6(:,2)),grid,axis([-90 90 -0.1 1.1])
title('Modulus 6'),ylabel('T1'),orient tall
subplot(5,1,2),plot(u2,c_m6(:,3)),grid,axis([-90 90 -0.1 1.1])
ylabel('T2'),orient tall
subplot(5,1,3),plot(u2,c_m6(:,4)),grid,axis([-90 90 -0.1 1.1])
ylabel('T3'),orient tall
subplot(5,1,4),plot(u2,c_m6(:,5)),grid,axis([-90 90 -0.1 1.1])
ylabel('T4'),orient tall
subplot(5,1,5),plot(u2,c_m6(:,6)),grid,axis([-90 90 -0.1 1.1])
ylabel('T5'),orient tall

```

```

figure(6)
plot(u2,osns_m11(:),'b-'),grid
hold on
plot(u2,osns_m6(:),'r:')
hold off
xlabel('Incident Angle of Arrival (degrees)')
ylabel('Number of Comparators')

```

```
title('Number of Comparators on each time step for mod 11 & mod 6')
axis([-90 90 -0.5 10.5])
orient landscape
```

```
for k=1:point_num
```

```
    if (osns_m11(k)==0 & osns_m6(k)==0)
        doa(k) = 0;

    elseif (osns_m11(k)==1 & osns_m6(k)==1)
        doa(k) = 1;

    elseif (osns_m11(k)==2 & osns_m6(k)==2)
        doa(k) = 2;

    elseif (osns_m11(k)==3 & osns_m6(k)==3)
        doa(k) = 3;

    elseif (osns_m11(k)==4 & osns_m6(k)==4)
        doa(k) = 4;

    elseif (osns_m11(k)==5 & osns_m6(k)==5)
        doa(k) = 5;

    elseif (osns_m11(k)==6 & osns_m6(k)==5)
        doa(k) = 6;

    elseif (osns_m11(k)==7 & osns_m6(k)==4)
        doa(k) = 7;

    elseif (osns_m11(k)==8 & osns_m6(k)==3)
        doa(k) = 8;

    elseif (osns_m11(k)==9 & osns_m6(k)==2)
        doa(k) = 9;

    elseif (osns_m11(k)==10 & osns_m6(k)==1)
        doa(k) = 10;

    elseif (osns_m11(k)==10 & osns_m6(k)==0)
        doa(k) = 11;

    elseif (osns_m11(k)==9 & osns_m6(k)==0)
        doa(k) = 12;

    elseif (osns_m11(k)==8 & osns_m6(k)==1)
```

```
    doa(k) = 13;

elseif (osns_m11(k)==7 & osns_m6(k)==2)
    doa(k) = 14;

elseif (osns_m11(k)==6 & osns_m6(k)==3)
    doa(k) = 15;

elseif (osns_m11(k)==5 & osns_m6(k)==4)
    doa(k) = 16;

elseif (osns_m11(k)==4 & osns_m6(k)==5)
    doa(k) = 17;

elseif (osns_m11(k)==3 & osns_m6(k)==5)
    doa(k) = 18;

elseif (osns_m11(k)==2 & osns_m6(k)==4)
    doa(k) = 19;

elseif (osns_m11(k)==1 & osns_m6(k)==3)
    doa(k) = 20;

elseif (osns_m11(k)==0 & osns_m6(k)==2)
    doa(k) = 21;

elseif (osns_m11(k)==0 & osns_m6(k)==1)
    doa(k) = 22;

elseif (osns_m11(k)==1 & osns_m6(k)==0)
    doa(k) = 23;

elseif (osns_m11(k)==2 & osns_m6(k)==0)
    doa(k) = 24;

elseif (osns_m11(k)==3 & osns_m6(k)==1)
    doa(k) = 25;

elseif (osns_m11(k)==4 & osns_m6(k)==2)
    doa(k) = 26;

elseif (osns_m11(k)==5 & osns_m6(k)==3)
    doa(k) = 27;

elseif (osns_m11(k)==6 & osns_m6(k)==4)
    doa(k) = 28;
```



```
elseif (osns_m11(k)==7 & osns_m6(k)==5)
    doa(k) = 29;

elseif (osns_m11(k)==8 & osns_m6(k)==5)
    doa(k) = 30;

elseif (osns_m11(k)==9 & osns_m6(k)==4)
    doa(k) = 31;

elseif (osns_m11(k)==10 & osns_m6(k)==3)
    doa(k) = 32;

elseif (osns_m11(k)==10 & osns_m6(k)==2)
    doa(k) = 33;

elseif (osns_m11(k)==9 & osns_m6(k)==1)
    doa(k) = 34;

elseif (osns_m11(k)==8 & osns_m6(k)==0)
    doa(k) = 35;

elseif (osns_m11(k)==7 & osns_m6(k)==0)
    doa(k) = 36;

elseif (osns_m11(k)==6 & osns_m6(k)==1)
    doa(k) = 37;

elseif (osns_m11(k)==5 & osns_m6(k)==2)
    doa(k) = 38;

elseif (osns_m11(k)==4 & osns_m6(k)==3)
    doa(k) = 39;

elseif (osns_m11(k)==3 & osns_m6(k)==4)
    doa(k) = 40;

elseif (osns_m11(k)==2 & osns_m6(k)==5)
    doa(k) = 41;

elseif (osns_m11(k)==1 & osns_m6(k)==5)
    doa(k) = 42;

elseif (osns_m11(k)==0 & osns_m6(k)==4)
    doa(k) = 43;
```

```
elseif (osns_m11(k)==0 & osns_m6(k)==3)
    doa(k) = 44;

elseif (osns_m11(k)==1 & osns_m6(k)==2)
    doa(k) = 45;

elseif (osns_m11(k)==2 & osns_m6(k)==1)
    doa(k) = 46;

elseif (osns_m11(k)==3 & osns_m6(k)==0)
    doa(k) = 47;

elseif (osns_m11(k)==4 & osns_m6(k)==0)
    doa(k) = 48;

elseif (osns_m11(k)==5 & osns_m6(k)==1)
    doa(k) = 49;

elseif (osns_m11(k)==6 & osns_m6(k)==2)
    doa(k) = 50;

elseif (osns_m11(k)==7 & osns_m6(k)==3)
    doa(k) = 51;

elseif (osns_m11(k)==8 & osns_m6(k)==4)
    doa(k) = 52;

elseif (osns_m11(k)==9 & osns_m6(k)==5)
    doa(k) = 53;

elseif (osns_m11(k)==10 & osns_m6(k)==5)
    doa(k) = 54;

elseif (osns_m11(k)==10 & osns_m6(k)==4)
    doa(k) = 55;

elseif (osns_m11(k)==9 & osns_m6(k)==3)
    doa(k) = 56;

elseif (osns_m11(k)==8 & osns_m6(k)==2)
    doa(k) = 57;

elseif (osns_m11(k)==7 & osns_m6(k)==1)
    doa(k) = 58;

elseif (osns_m11(k)==6 & osns_m6(k)==0)
```

```

doa(k) = 59;

elseif (osns_m11(k)==5 & osns_m6(k)==0)
doa(k) = 60;

elseif (osns_m11(k)==4 & osns_m6(k)==1)
doa(k) = 61;

elseif (osns_m11(k)==3 & osns_m6(k)==2)
doa(k) = 62;

elseif (osns_m11(k)==2 & osns_m6(k)==3)
doa(k) = 63;

elseif (osns_m11(k)==1 & osns_m6(k)==4)
doa(k) = 64;

elseif (osns_m11(k)==0 & osns_m6(k)==5)
doa(k) = 65;

else
doa(k) = 100;

end

end

xarray=[-90:180/1800:90];
newvar=100/66;

figure(7)
doa1=doa(1:1400);
lgt=length(doa1);
dlg=100/(lgt-1);
xary=[-50:dlg:50];
plot(xary, -(doa1*newvar-33*newvar)),grid
xlabel('Angle of Arrival (degrees)')
ylabel('Estimated Angle of Arrival (degrees)')
orient landscape

```

APPENDIX B. LABVIEW VI CODE

LabVIEW Virtual Instruments (VI) code has been used to create the Thomas.vi program. The Thomas.vi is used to control GPIB in order to communicate with the multimeter to get the output voltage values of the mixer and store them.

Before proceeding to the small description of the program itself it is useful to say a few words about the GPIB.

The General Purpose Interface Bus (GPIB), also called IEEE 488, is a method of communicating with standard-alone instruments, such as multimeters and oscilloscopes. The most direct method is to install a plug-in GPIB board in the computer and connect the respective instrument directly to this board with a GPIB cable, as the Figure B.1 shows. The GPIB cable consists of a shielded 24-conductor cable, which has both a plug and a receptacle connector at each end, as Figure B.2 shows. [Ref. 19]

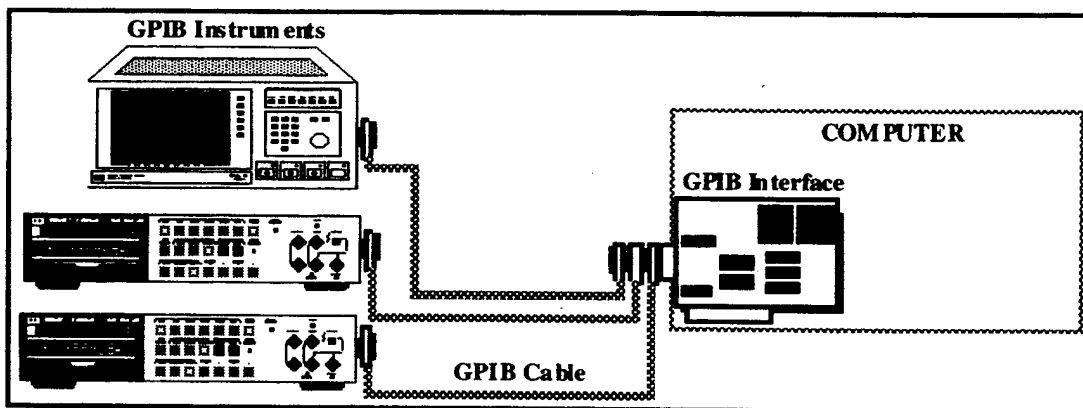


Figure B.1: Configuration to link devices using a GPIB cable. [Ref. 19]

The GPIB carries device-dependent messages and interface messages. GPIB devices can be Talkers, Listeners, and Controllers. A multimeter, like in our case, is a Talker and may be a Listener as well. The Controller manages the flow of information on the GPIB by sending commands to all devices.

With the GPIB interface board and its software, the computer plays all three roles:

- Controller – to manage the GPIB,
- Talker – to send data,
- Listener – to receive data.

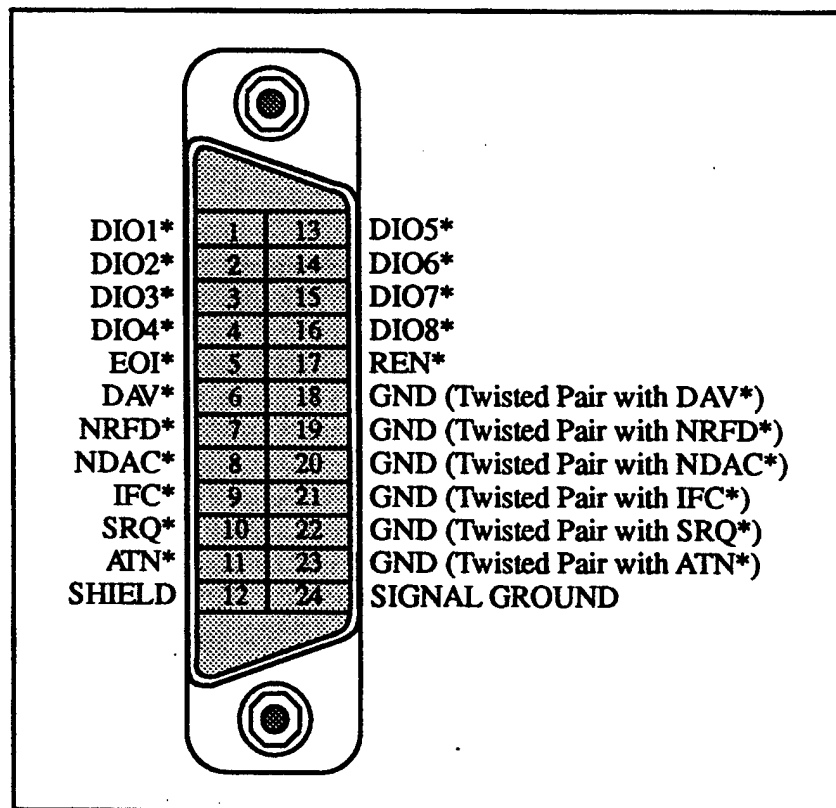


Figure B.2: A GPIB Connector Showing Signal Assignment. [Ref. 19]

After this small analysis, the code will be understandable easily.

Any VI contains an interactive user interface, which is called the front panel, because it simulates the panel of physical instrument. The front panel can contain knobs, push buttons, graphs, and other controls and indicators, as shown in Figure B.3. VI receives instructions from a block diagram, which it can be constructed using the graphical programming language, G. We can think of the block diagram as source code.

The procedure for this code and the small steps, that are followed for the successful communication between a GPIB device and a computer, are shown below:

- i. Service Request (SRQ). The GPIB line that the device asserts to notify the CIC (Controller-In-Charge) that the device needs servicing.
- ii. Writes command string and send it to the GPIB device (multimeter), as the frame 0 in Figure B.4 shows.
- iii. Waits for GPIB to assert SRQ to indicate that reading is available, as shown in Figure B.5 (frame 1).
- iv. Reads measurement from multimeter, as shown in Figure B.5 (frame 2). As the left icon in this frame indicates, reads by the count number of bytes from the GPIB device (multimeter). As the right icon indicates, it copies the measurement value.
- v. Figure B.6 shows that it clears the SRQ mode in order to be ready for the next request. [Ref. 19]

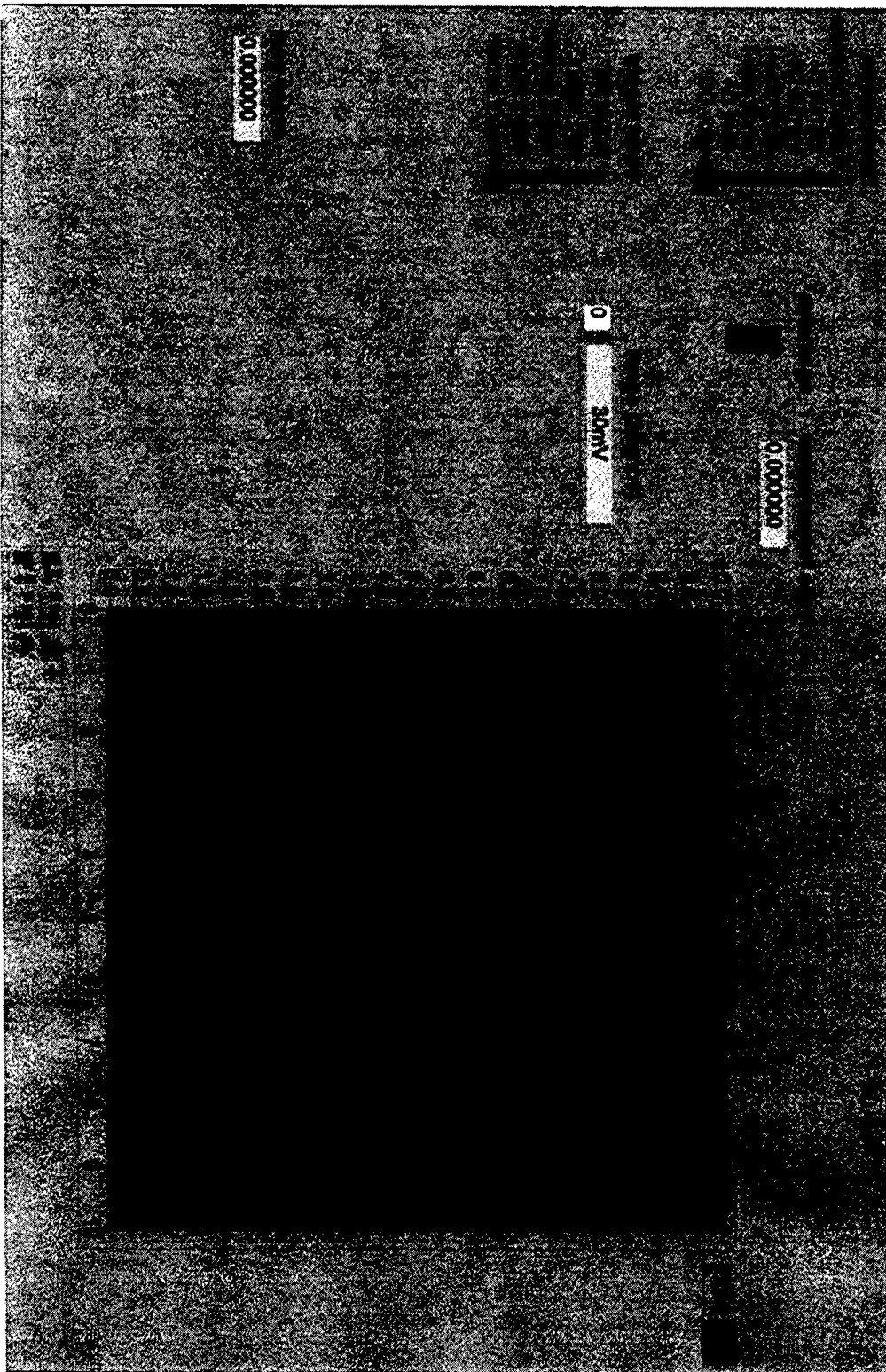


Figure B.3: Front Panel.

Thomas.vi
Last modified on 10/3/97 at 11:56 AM

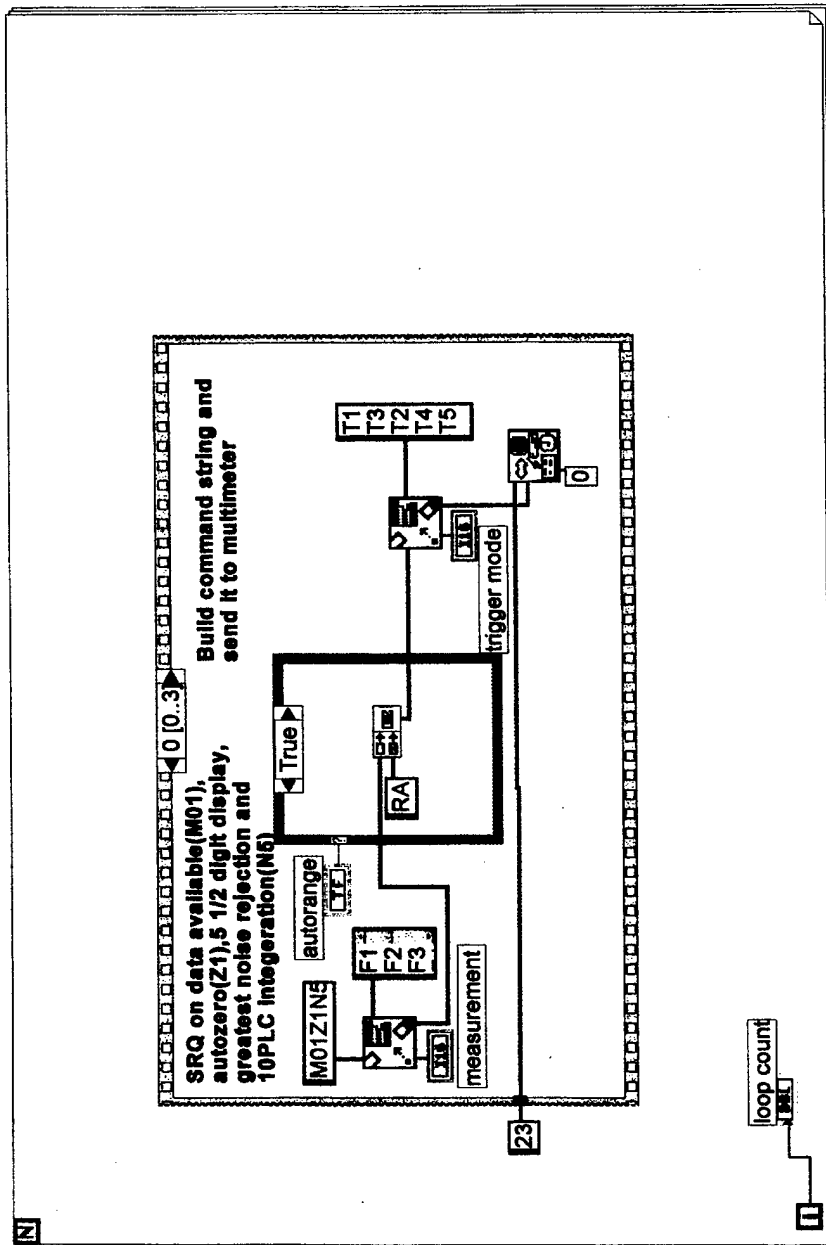


Figure B.4: Writes command string and send it to the GPIB device (multimeter).

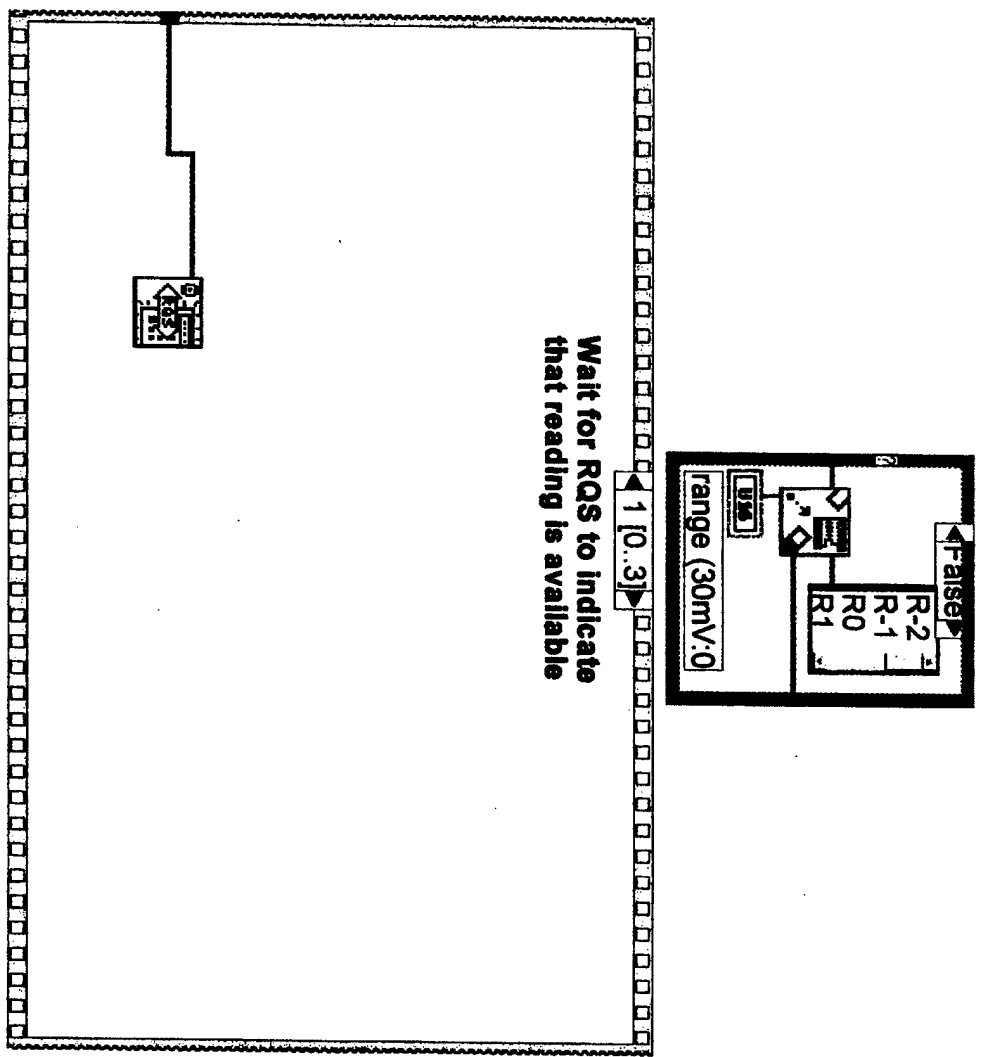
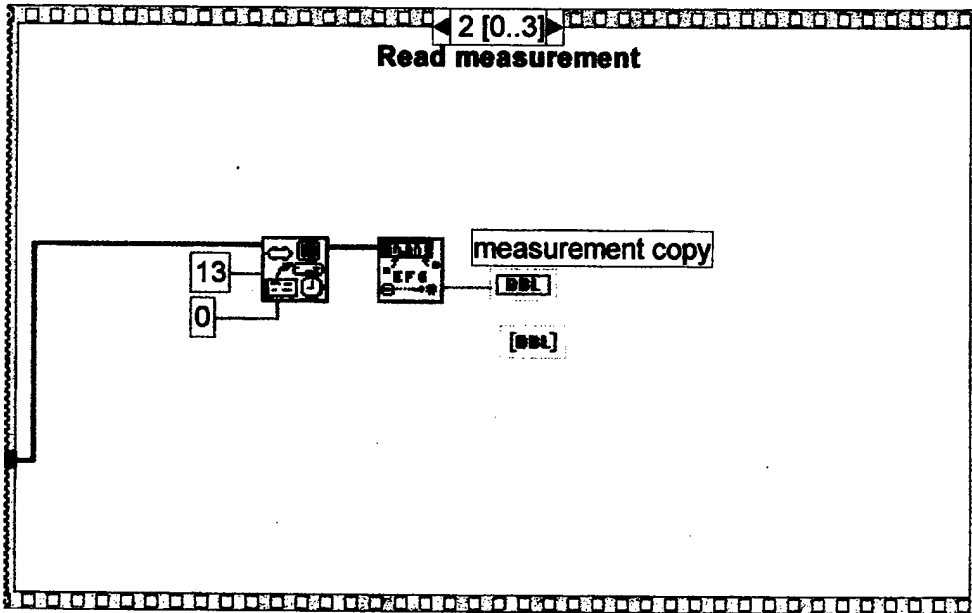


Figure B.5: Frame 1 waits for GPIB to assert SRQ.

Frame 2 reads measurement from multimeter.

Thomas.vi
Last modified on 10/3/97 at 11:56 AM



Thomas.vi
Last modified on 10/3/97 at 11:56 AM

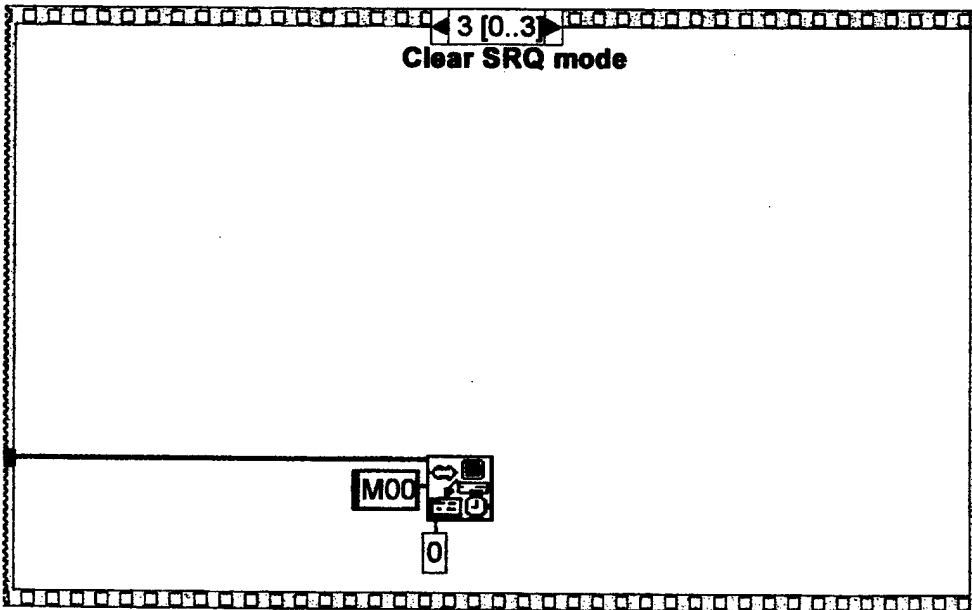


Figure B.6: Clears the SRQ mode in order to be ready for the next request.

APPENDIX C. MOD_EMUP PROGRAM FOR EEPROM

The programming of the EEPROM is made using a specific program MOD_EMUP made by Universal Programmer & Tester MODULAR CIRCUIT TECHNOLOGY.

The memory of EEPROM is organized into words. The memory map, with the intermission of each row with each column, is corresponding to a different address.

```
00000 00 16 FF 15 FF FF FF 2C --FF FF FF FF FF FF FF 2B .....+
00010 FF FF FF FF FF FF FF FF --FF FF FF FF FF FF FF 41 .....A
00020 17 01 FF 2D FF FF FF 14 --FF FF FF FF FF FF FF 40 ...-.....@
00030 FF FF FF FF FF FF FF FF --FF FF FF FF FF FF FF 2A .....*
00040 FF FF FF FF FF FF FF FF --FF FF FF FF FF FF FF FF .....
00050 FF FF FF FF FF FF FF FF --FF FF FF FF FF FF FF FF .....
00060 18 2E FF 02 FF FF FF 3F --FF FF FF FF FF FF FF 13 .....?.....
00070 FF FF FF FF FF FF FF FF --FF FF FF FF FF FF FF 29 .....)
00080 FF FF FF FF FF FF FF FF --FF FF FF FF FF FF FF FF .....
00090 FF FF FF FF FF FF FF FF --FF FF FF FF FF FF FF FF .....
000A0 FF FF FF FF FF FF FF FF --FF FF FF FF FF FF FF FF .....
000B0 FF FF FF FF FF FF FF FF --FF FF FF FF FF FF FF FF .....
000C0 FF FF FF FF FF FF FF FF --FF FF FF FF FF FF FF FF .....
000D0 FF FF FF FF FF FF FF FF --FF FF FF FF FF FF FF FF .....
000E0 2F 19 FF 3E FF FF FF 03 --FF FF FF FF FF FF FF 28 /..>.....(
```

000F0 FF FF FF FF FF FF FF FF --FF FF FF FF FF FF FF 12
 00100 FF FF FF FF FF FF FF FF --FF FF FF FF FF FF FF FF
 00110 FF FF FF FF FF FF FF FF --FF FF FF FF FF FF FF FF
 00120 FF FF FF FF FF FF FF FF --FF FF FF FF FF FF FF FF
 00130 FF FF FF FF FF FF FF FF --FF FF FF FF FF FF FF FF
 00140 FF FF FF FF FF FF FF FF --FF FF FF FF FF FF FF FF
 00150 FF FF FF FF FF FF FF FF --FF FF FF FF FF FF FF FF
 00160 FF FF FF FF FF FF FF FF --FF FF FF FF FF FF FF FF
 00170 FF FF FF FF FF FF FF FF --FF FF FF FF FF FF FF FF
 00180 FF FF FF FF FF FF FF FF --FF FF FF FF FF FF FF FF
 00190 FF FF FF FF FF FF FF FF --FF FF FF FF FF FF FF FF
 001A0 FF FF FF FF FF FF FF FF --FF FF FF FF FF FF FF FF
 001B0 FF FF FF FF FF FF FF FF --FF FF FF FF FF FF FF FF
 001C0 FF FF FF FF FF FF FF FF --FF FF FF FF FF FF FF FF
 001D0 FF FF FF FF FF FF FF FF --FF FF FF FF FF FF FF FF
 01E0 30 3D FF 1A FF FF FF 27 --FF FF FF FF FF FF FF 04 0=.....
 001F0 FF FF FF FF FF FF FF FF --FF FF FF FF FF FF FF 11
 00200 FF FF FF FF FF FF FF FF --FF FF FF FF FF FF FF FF
 00210 FF FF FF FF FF FF FF FF --FF FF FF FF FF FF FF FF

 003C0 FF FF FF FF FF FF FF FF --FF FF FF FF FF FF FF FF
 003D0 FF FF FF FF FF FF FF FF --FF FF FF FF FF FF FF FF
 003E0 3C 31 FF 26 FF FF FF 1B --FF FF FF FF FF FF FF 10 <1.&.....

003F0 FF FF FF FF FF FF FF FF --FF FF FF FF FF FF FF 05

00400 FF FF FF FF FF FF FF FF --FF FF FF FF FF FF FF FF

00410 FF FF FF FF FF FF FF FF --FF FF FF FF FF FF FF FF

... ..

007C0 FF FF FF FF FF FF FF FF --FF FF FF FF FF FF FF FF

007D0 FF FF FF FF FF FF FF FF --FF FF FF FF FF FF FF FF

007E0 3B 25 FF 32 FF FF FF 0F --FF FF FF FF FF FF FF 1C ;%.2.....

007F0 FF FF FF FF FF FF FF FF --FF FF FF FF FF FF FF 06

00800 FF FF FF FF FF FF FF FF --FF FF FF FF FF FF FF FF

00810 FF FF FF FF FF FF FF FF --FF FF FF FF FF FF FF FF

... ..

00FC0 FF FF FF FF FF FF FF FF --FF FF FF FF FF FF FF FF

00FD0 FF FF FF FF FF FF FF FF --FF FF FF FF FF FF FF FF

00FE0 24 34 FF 0E FF FF FF 33 --FF FF FF FF FF FF FF 07 \$:.....3.....

00FF0 FF FF FF FF FF FF FF FF --FF FF FF FF FF FF FF 1D

01000 FF FF FF FF FF FF FF FF --FF FF FF FF FF FF FF FF

01010 FF FF FF FF FF FF FF FF --FF FF FF FF FF FF FF FF

... ..

01FC0 FF FF FF FF FF FF FF FF --FF FF FF FF FF FF FF FF

01FD0 FF FF FF FF FF FF FF FF --FF FF FF FF FF FF FF FF
01FE0 23 0D FF 39 FF FF FF 08 --FF FF FF FF FF FF FF FF 34 #..9.....4
01FF0 FF FF FF FF FF FF FF FF --FF FF FF FF FF FF FF FF 1E
02000 FF FF FF FF FF FF FF FF --FF FF FF FF FF FF FF FF
02010 FF FF FF FF FF FF FF FF --FF FF FF FF FF FF FF FF

...

03FC0 FF FF FF FF FF FF FF FF --FF FF FF FF FF FF FF FF
03FD0 FF FF FF FF FF FF FF FF --FF FF FF FF FF FF FF FF
03FE0 0C 22 FF 09 FF FF FF 38 --FF FF FF FF FF FF FF FF 1F .“.....8.....
03FF0 FF FF FF FF FF FF FF FF --FF FF FF FF FF FF FF FF 35
04000 FF FF FF FF FF FF FF FF --FF FF FF FF FF FF FF FF
04010 FF FF FF FF FF FF FF FF --FF FF FF FF FF FF FF FF

...

07FC0 FF FF FF FF FF FF FF FF --FF FF FF FF FF FF FF FF
07FD0 FF FF FF FF FF FF FF FF --FF FF FF FF FF FF FF FF
07FE0 0B 0A FF 21 FF FF FF 20 --FF FF FF FF FF FF FF FF 37 ...!....7
07FF0 FF FF FF FF FF FF FF FF --FF FF FF FF FF FF FF FF 366
08000 FF FF FF FF FF FF FF FF --FF FF FF FF FF FF FF FF
08010 FF FF FF FF FF FF FF FF --FF FF FF FF FF FF FF FF

... ..

09000 FF FF FF FF FF FF FF FF --FF FF FF FF FF FF FF FF

09010 FF FF FF FF FF FF FF FF --FF FF FF FF FF FF FF FF

09020 FF FF FF FF FF FF FF FF --FF FF FF FF FF FF FF FF

09030 FF FF FF FF FF FF FF FF --FF FF FF FF FF FF FF FF

APPENDIX D. MAX916 DATA SHEETS

19-0183; Rev 0; 9/93



Ultra High-Speed, High-Resolution, Single-/Dual-Supply TTL Comparators

MAX915/MAX916

General Description

The MAX915/MAX916 high-speed, single and dual TTL voltage comparators eliminate oscillation by separating the comparator input and output stages with a negative edge-triggered master/slave flip-flop. Comparator propagation delay is typically 6ns, and is insensitive to input overdrive. The MAX915 and MAX916 resolve input signals as small as 2mV and 2.4mV, respectively.

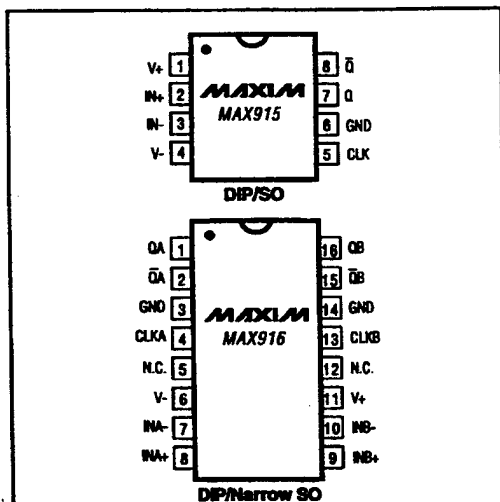
These comparators operate either from dual supplies or from a single +5V supply. The input common-mode voltage range extends below the negative supply rail, allowing ground-sensing applications with a single +5V supply.

The MAX915 is a single TTL comparator, available in 8-pin DIP and SO packages. The MAX916 is a dual version available in 16-pin DIP and SO packages. For equivalent devices with complementary ECL outputs and 2ns propagation delay, see the single/dual MAX905/MAX906.

Applications

- High-Speed A/D Converters
- High-Speed Line Receivers
- Peak Detectors
- Threshold Detectors
- High-Speed Triggers
- Synchronous Data Discriminators

Pin Configurations



Features

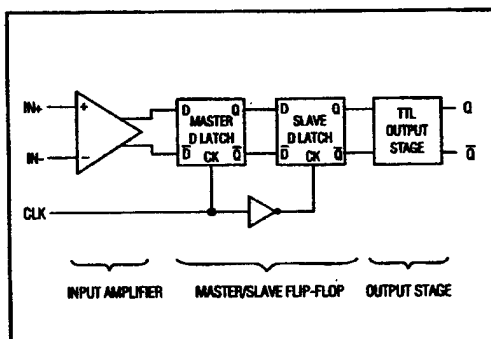
- ◆ Oscillation Free: Clocked Architecture
- ◆ 6ns Propagation Delay
- ◆ Propagation Delay Insensitive to Overdrive
- ◆ Single +5V or Dual ±5V Supplies
- ◆ 2mV Input Resolution (MAX915)
- ◆ Input Range Includes Negative Supply Rail
- ◆ Low Power: 14mA (70mW) per Comparator, +5V
- ◆ 1.5ns Setup Time with 5mV Overdrive
- ◆ No Minimum Requirement for Input Signal Slew Rate
- ◆ Complementary TTL Outputs

Ordering Information

PART	TEMP. RANGE	PIN-PACKAGE
MAX915CPA	0°C to +70°C	8 Plastic DIP
MAX915CSA	0°C to +70°C	8 SO
MAX915C/D	0°C to +70°C	Dice*
MAX915EPA	-40°C to +85°C	8 Plastic DIP
MAX915ESA	-40°C to +85°C	8 SO
MAX915MJA	-55°C to +125°C	8 CERDIP
MAX916CPE	0°C to +70°C	16 Plastic DIP
MAX916CSE	0°C to +70°C	16 Narrow SO
MAX916C/D	0°C to +70°C	Dice*
MAX916EPE	-40°C to +85°C	16 Plastic DIP
MAX916ESE	-40°C to +85°C	16 Narrow SO

* Contact factory for dice specifications.

Functional Diagram



Ultra High-Speed, High-Resolution, Single-/Dual-Supply TTL Comparators

ABSOLUTE MAXIMUM RATINGS

Positive Supply Voltage (V+ to GND).....	+5V
Negative Supply Voltage (V- to GND).....	-5V
Differential Input Voltage.....	(V- - 0.3V) to (V+ + 0.3V)
Common-Mode Input Voltage.....	(V- - 0.3V) to (V+ + 0.3V)
Clock Input Voltage.....	(GND - 0.3V) to (V+ + 0.3V)
Output Short-Circuit Duration	
To V+, GND.....	Continuous
To V-.....	10sec
Output Current (Q or \bar{Q}).....	20mA

Continuous Power Dissipation (TA = +70°C)

8-Pin Plastic DIP (derate 9.09mW/°C above +70°C).....	727mW
8-Pin SO (derate 5.88mW/°C above +70°C).....	471mW
8-Pin CERDIP (derate 8.00mW/°C above +70°C).....	640mW
16-Pin Plastic DIP (derate 10.53mW/°C above +70°C).....	842mW
16-Pin Narrow SO (derate 8.70mW/°C above +70°C).....	696mW
Storage Temperature Range.....	-65°C to +150°C
Junction Temperature Range.....	-65°C to +170°C
Lead Temperature (soldering, 10sec).....	+300°C

Stresses beyond those listed under "Absolute Maximum Ratings" may cause permanent damage to the device. These are stress ratings only, and functional operation of the device at these or any other conditions beyond those indicated in the operational sections of the specifications is not implied. Exposure to absolute maximum rating conditions for extended periods may affect device reliability.

ELECTRICAL CHARACTERISTICS

(V+ = +5V, V- = -5V, TA = +25°C, unless otherwise noted.)

PARAMETER	SYMBOL	CONDITIONS		MIN	TYP	MAX	UNITS
Input Offset Voltage	VOS	VCM = 0V	MAX915		0.5	1.5	mV
			MAX916		0.5	2.0	
Input Bias Current	IB	IB+ or IB-			5	10	μA
Input Offset Current	IOS	VCM = 0V			0.2	1.0	μA
Input Referred Noise Voltage	en	(Note 1)			600	900	μV
Input Common-Mode Range	VCMR			V- - 0.1		V+ - 2.2	V
Common-Mode Rejection Ratio	CMRR	(Note 2)			90	120	μV/V
Power-Supply Rejection Ratio	PSRR	(Note 3)			60	120	μV/V
Output High Voltage	VOH	(Note 4)		2.8	3.5		V
Output Low Voltage	VOL	(Note 4)			0.3	0.4	V
Clock Input Voltage High	VIH			2			V
Clock Input Voltage Low	VIL					0.8	V
Clock Input Current High	IiH				0.5	10	μA
Clock Input Current Low	IiL				2.5	10	μA
Positive Supply Current (Note 5)	I+	MAX915			14	18	mA
		MAX916			28	36	
Negative Supply Current (Note 5)	I-	MAX915			3	4	mA
		MAX916			6	8	
Power Dissipation (Note 5)	PD	V+ = 5.25V, V- = -5.25V	MAX915		85	115	mW
			MAX916		170	230	
Propagation Delay (Notes 6, 7, 9)	tPD+	Q, \bar{Q} rising			6	8	ns
	tPD-	Q, \bar{Q} falling			6	8	
Propagation-Delay Skew	tSKEW	(Notes 6, 7, 8)			0.5	3.0	ns
Clock Setup Time (Notes 6, 9)	tSU	VOD = 5mV			1.5		ns
		VOD = 10mV			1.0	2.0	

Ultra High-Speed, High-Resolution, Single-/Dual-Supply TTL Comparators

MAX915/MAX916

ELECTRICAL CHARACTERISTICS

(V+ = +5V, V- = -5V, TA = TMIN to TMAX, unless otherwise noted.)

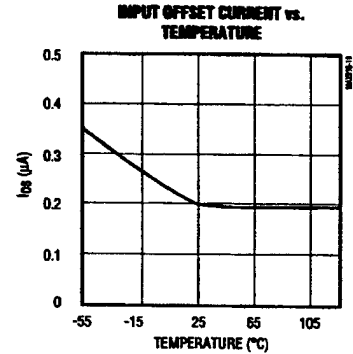
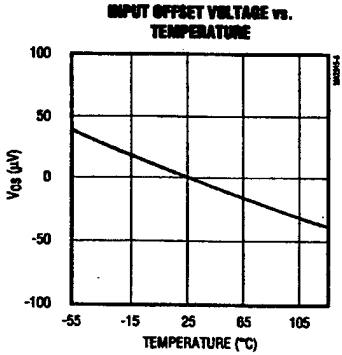
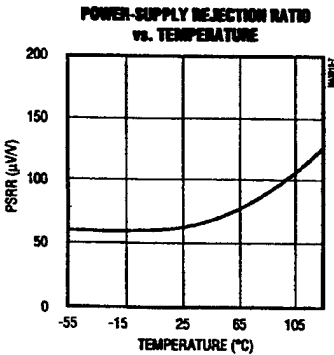
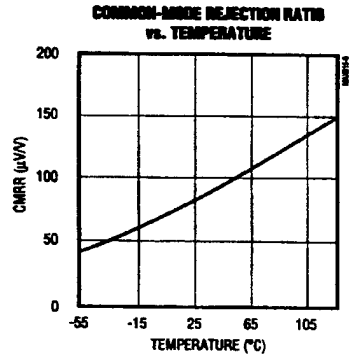
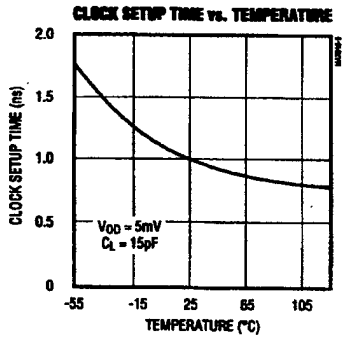
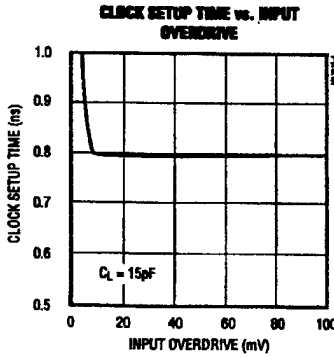
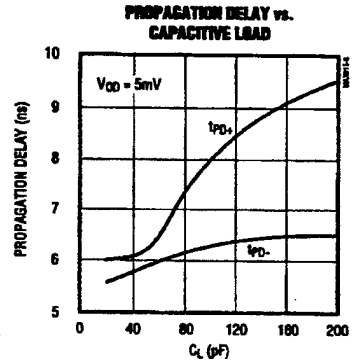
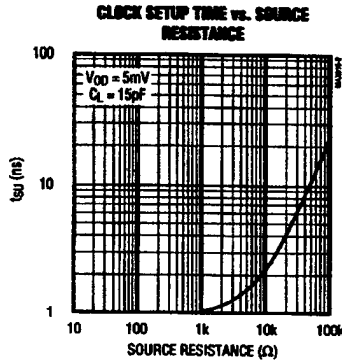
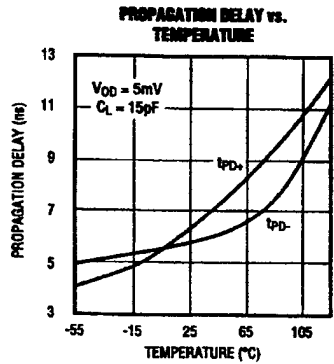
PARAMETER	SYMBOL	CONDITIONS		MIN	TYP	MAX	UNITS
Input Offset Voltage	V _{OS}	V _{CM} = 0V	MAX915	0.5	2.0	mV	
			MAX916	0.5	3.0		
Input Bias Current	I _B	I _{B+} or I _{B-}		5	15	μA	
Input Offset Current	I _{OS}	V _{CM} = 0V		0.2	2.0	μA	
Input Referred Noise Voltage	e _n	(Note 1)		600	900	μV	
Input Common-Mode Range	V _{CMR}			V- - 0.1	V+ - 2.2	V	
Common-Mode Rejection Ratio	CMRR	(Note 2)		90	150	μV/V	
Power-Supply Rejection Ratio	PSRR	(Note 3)		60	150	μV/V	
Output High Voltage	V _{OH}	(Note 4)		2.8	3.5	V	
Output Low Voltage	V _{OL}	(Note 4)		0.3	0.4	V	
Clock Input Voltage High	V _{IH}			2		V	
Clock Input Voltage Low	V _{IL}					0.8	V
Clock Input Current High	I _{IH}			0.5	15	μA	
Clock Input Current Low	I _{IL}			2.5	15	μA	
Positive Supply Current (Note 5)	I ₊	MAX915		14	22	mA	
		MAX916		28	44		
Negative Supply Current (Note 5)	I ₋	MAX915		3	6	mA	
		MAX916		6	12		
Power Dissipation (Note 5)	PD	V+ = 5.25V, V- = -5.25V	MAX915	85	150	mW	
			MAX916	170	300		
Propagation Delay (Notes 6, 7, 9)	t _{PD+}	Q, \bar{Q} rising	MAX91_C	6	10	ns	
			MAX91_E	6	12		
			MAX91_M	6	15		
	t _{PD-}	Q, \bar{Q} falling	MAX91_C	6	10		
			MAX91_E	6	12		
			MAX91_M	6	15		
Propagation-Delay Skew	t _{SKEW}	(Notes 6, 7, 8)		0.5	4.0	ns	
Clock Setup Time (Notes 6, 9)	t _{SU}	V _{OD} = 5mV		1.5		ns	
		V _{OD} = 10mV		1.0	2.0		

- Note 1:** Guaranteed by design. Input referred noise voltage uncertainty is specified over the full bandwidth of the device.
- Note 2:** Common-mode rejection ratio is tested over the full common-mode range. The common-mode range for dual-supply operation is from (V- - 0.1V) to (V+ - 2.2V). The common-mode range for single-supply operation is from -0.1V to (V+ - 2.2V).
- Note 3:** Tested for 4.75V < V+ < 5.25V and -5.25V < V- < 0V.
- Note 4:** TTL output voltage high and low tested with V+ = 4.75V, I_{OH} = 4mA, I_{OL} = 8mA.
- Note 5:** I+, I-, and PD tested for worst-case condition of V+ = 5.25V and V- = -5.25V. Output not loaded.
- Note 6:** Guaranteed by design. Measured in a high-speed fixture with C_L = 15pF, I_Q = 2mA. See Figure 1 for timing parameter definitions. Guaranteed for both single- and dual-supply operation.
- Note 7:** Propagation delay measured with an input signal of 100mV, with 5mV overdrive.
- Note 8:** Propagation delay skew is defined as the difference in t_{PD} for the complementary outputs, Q and \bar{Q} (see Figure 1).
- Note 9:** Clock input voltage rise and fall times should not exceed 100ns for correct triggering of comparator.

Ultra High-Speed, High-Resolution, Single-/Dual-Supply TTL Comparators

Typical Operating Characteristics

($V_+ = +5V$, $V_- = -5V$, $T_A = +25^\circ C$, unless otherwise noted.)

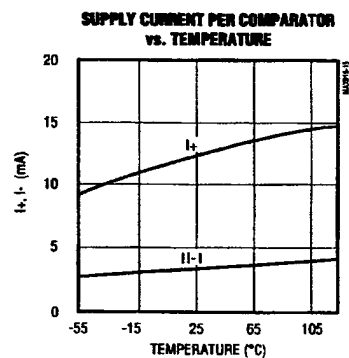
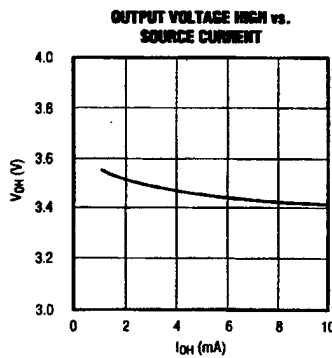
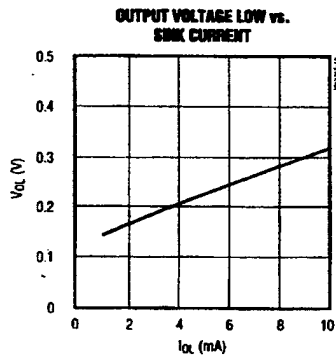
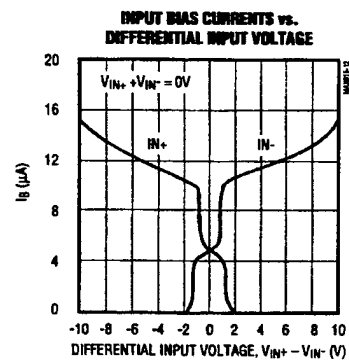
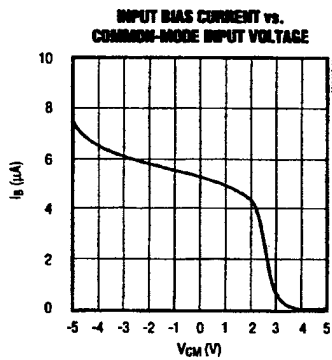
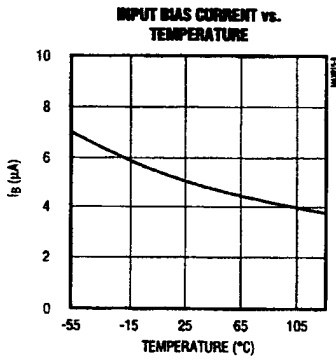


Ultra High-Speed, High-Resolution, Single-/Dual-Supply TTL Comparators

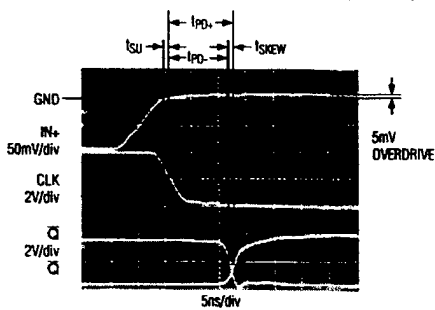
Typical Operating Characteristics (continued)

($V_+ = +5V$, $V_- = -5V$, $T_A = +25^\circ C$, unless otherwise noted.)

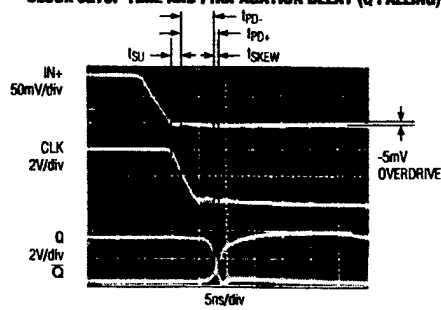
MAX915/MAX916



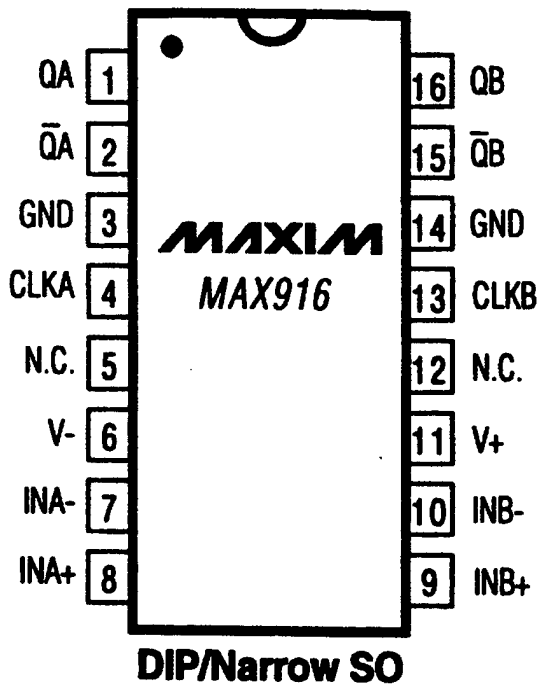
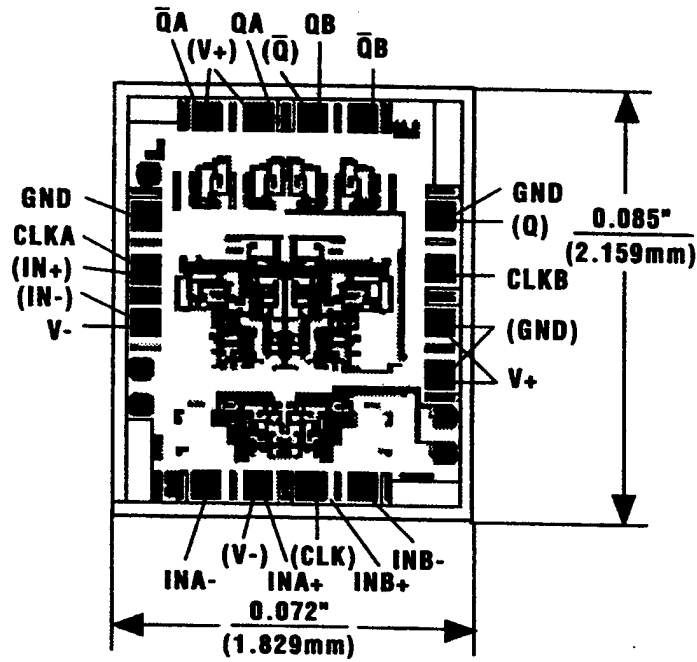
CLOCK SETUP TIME AND PROPAGATION DELAY (Q RISING)



CLOCK SETUP TIME AND PROPAGATION DELAY (Q FALLING)



Chip Topography

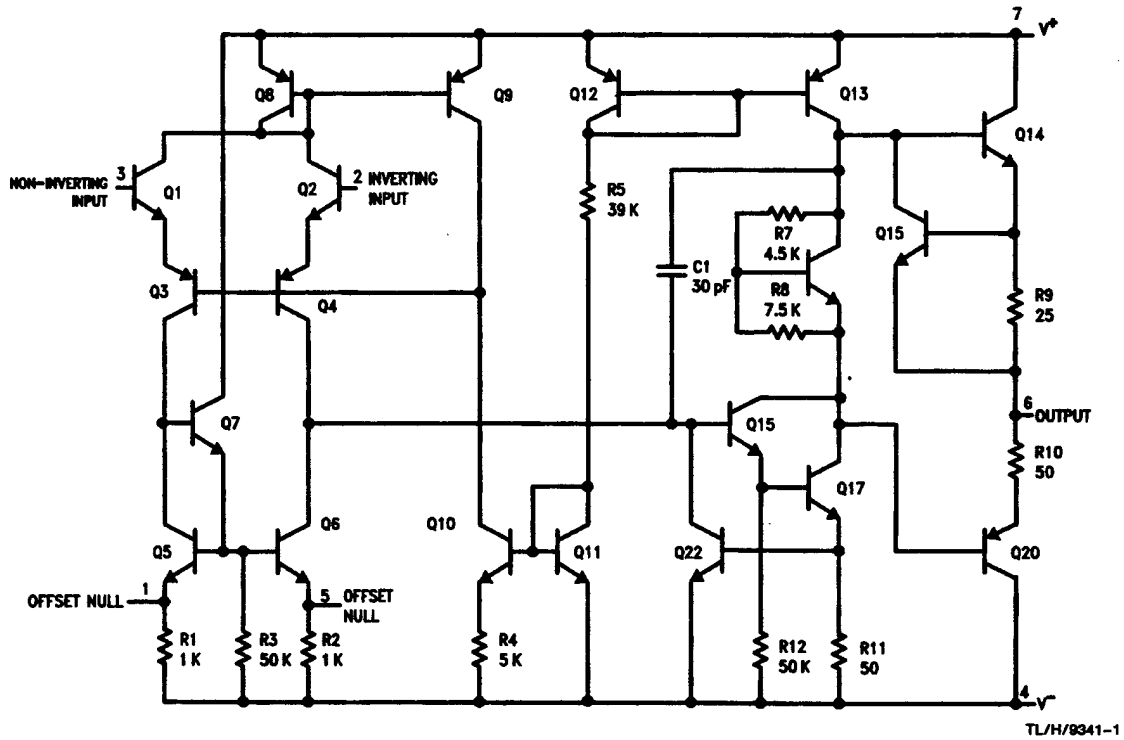


Pin Descriptions

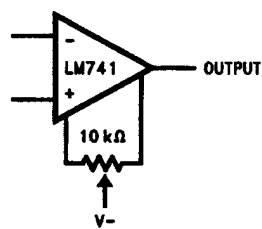
MAX916		
PIN	NAME	FUNCTION
1	QA	TTL Output, Channel A
2	$\bar{Q}A$	Complementary TTL Output, Channel A
3	GND	Ground
4	CLKA	Clock Input, Channel A
5, 12	N.C.	No Connect. Not internally connected.
6	V-	Negative Supply. Connect to GND for single-supply operation.
7	INA-	Inverting Input, Channel A
8	INA+	Noninverting Input, Channel A
9	INB+	Noninverting Input, Channel B
10	INB-	Inverting Input, Channel B
11	V+	Positive Supply
13	CLKB	Clock Input, Channel B
14	GND	Ground
15	$\bar{Q}B$	Complementary TTL Output, Channel B
16	QB	TTL Output, Channel B

APPENDIX E. LM 741CN DATA SHEETS

Schematic Diagram



Offset Nulling Circuit



Absolute Maximum Ratings

If Military/Aerospace specified devices are required, please contact the National Semiconductor Sales Office/Distributors for availability and specifications.

(Note 5)

	LM741A	LM741E	LM741	LM741C
Supply Voltage	±22V	±22V	±22V	±18V
Power Dissipation (Note 1)	500 mW	500 mW	500 mW	500 mW
Differential Input Voltage	±30V	±30V	±30V	±30V
Input Voltage (Note 2)	±15V	±15V	±15V	±15V
Output Short Circuit Duration	Continuous	Continuous	Continuous	Continuous
Operating Temperature Range	-55°C to +125°C	0°C to +70°C	-55°C to +125°C	0°C to +70°C
Storage Temperature Range	-65°C to +150°C	-65°C to +150°C	-65°C to +150°C	-65°C to +150°C
Junction Temperature	150°C	100°C	150°C	100°C
Soldering Information				
N-Package (10 seconds)	260°C	260°C	260°C	260°C
J- or H-Package (10 seconds)	300°C	300°C	300°C	300°C
M-Package				
Vapor Phase (60 seconds)	215°C	215°C	215°C	215°C
Infrared (15 seconds)	215°C	215°C	215°C	215°C

See AN-450 "Surface Mounting Methods and Their Effect on Product Reliability" for other methods of soldering surface mount devices.

ESD Tolerance (Note 6)	400V	400V	400V	400V
------------------------	------	------	------	------

Electrical Characteristics (Note 3)

Parameter	Conditions	LM741A/LM741E			LM741			LM741C			Units
		Min	Typ	Max	Min	Typ	Max	Min	Typ	Max	
Input Offset Voltage	$T_A = 25^\circ\text{C}$ $R_S \leq 10\text{ k}\Omega$ $R_S \leq 50\Omega$		0.8	3.0		1.0	5.0		2.0	6.0	mV mV
	$T_{\text{AMIN}} \leq T_A \leq T_{\text{AMAX}}$ $R_S \leq 50\Omega$ $R_S \leq 10\text{ k}\Omega$			4.0			6.0			7.5	mV mV
				15							$\mu\text{V}/^\circ\text{C}$
Average Input Offset Voltage Drift				15							$\mu\text{V}/^\circ\text{C}$
Input Offset Voltage Adjustment Range	$T_A = 25^\circ\text{C}, V_S = \pm 20\text{V}$	±10				±15			±15		mV
Input Offset Current	$T_A = 25^\circ\text{C}$		3.0	30		20	200		20	200	nA
	$T_{\text{AMIN}} \leq T_A \leq T_{\text{AMAX}}$			70		85	500			300	nA
Average Input Offset Current Drift				0.5							nA/°C
Input Bias Current	$T_A = 25^\circ\text{C}$		30	80		80	500		80	500	nA
	$T_{\text{AMIN}} \leq T_A \leq T_{\text{AMAX}}$			0.210			1.5			0.8	μA
Input Resistance	$T_A = 25^\circ\text{C}, V_S = \pm 20\text{V}$	1.0	6.0		0.3	2.0		0.3	2.0		M Ω
	$T_{\text{AMIN}} \leq T_A \leq T_{\text{AMAX}}$ $V_S = \pm 20\text{V}$	0.5									M Ω
Input Voltage Range	$T_A = 25^\circ\text{C}$							±12	±13		V
	$T_{\text{AMIN}} \leq T_A \leq T_{\text{AMAX}}$				±12	±13					V
Large Signal Voltage Gain	$T_A = 25^\circ\text{C}, R_L \geq 2\text{ k}\Omega$ $V_S = \pm 20\text{V}, V_O = \pm 15\text{V}$ $V_S = \pm 15\text{V}, V_O = \pm 10\text{V}$	50			50	200		20	200		V/mV V/mV
	$T_{\text{AMIN}} \leq T_A \leq T_{\text{AMAX}}$ $R_L \geq 2\text{ k}\Omega$ $V_S = \pm 20\text{V}, V_O = \pm 15\text{V}$ $V_S = \pm 15\text{V}, V_O = \pm 10\text{V}$	32			25			15			V/mV V/mV
	$V_S = \pm 5\text{V}, V_O = \pm 2\text{V}$	10									V/mV

Electrical Characteristics (Note 3) (Continued)

Parameter	Conditions	LM741A/LM741E			LM741			LM741C			Units
		Min	Typ	Max	Min	Typ	Max	Min	Typ	Max	
Output Voltage Swing	$V_S = \pm 20V$ $R_L \geq 10 k\Omega$ $R_L \geq 2 k\Omega$	± 16 ± 15									V V
	$V_S = \pm 15V$ $R_L \geq 10 k\Omega$ $R_L \geq 2 k\Omega$				± 12 ± 10	± 14 ± 13		± 12 ± 10	± 14 ± 13		V V
Output Short Circuit Current	$T_A = 25^\circ C$ $T_{AMIN} \leq T_A \leq T_{AMAX}$	10 10	25	35 40		25			25		mA mA
Common-Mode Rejection Ratio	$T_{AMIN} \leq T_A \leq T_{AMAX}$ $R_S \leq 10 k\Omega, V_{CM} = \pm 12V$ $R_S \leq 50\Omega, V_{CM} = \pm 12V$	80	95		70	90		70	90		dB dB
Supply Voltage Rejection Ratio	$T_{AMIN} \leq T_A \leq T_{AMAX}$ $V_S = \pm 20V$ to $V_S = \pm 5V$ $R_S \leq 50\Omega$ $R_S \leq 10 k\Omega$	86	96		77	96		77	96		dB dB
Transient Response Rise Time	$T_A = 25^\circ C$, Unity Gain		0.25	0.8		0.3			0.3		μs
Overshoot			6.0	20		5			5		%
Bandwidth (Note 4)	$T_A = 25^\circ C$	0.437	1.5								MHz
Slew Rate	$T_A = 25^\circ C$, Unity Gain	0.3	0.7			0.5			0.5		V/ μs
Supply Current	$T_A = 25^\circ C$					1.7	2.8		1.7	2.8	mA
Power Consumption	$T_A = 25^\circ C$ $V_S = \pm 20V$ $V_S = \pm 15V$		80	150		50	85		50	85	mW mW
	LM741A $V_S = \pm 20V$ $T_A = T_{AMIN}$ $T_A = T_{AMAX}$			165 135							mW mW
	LM741E $V_S = \pm 20V$ $T_A = T_{AMIN}$ $T_A = T_{AMAX}$			150 150							mW mW
	LM741 $V_S = \pm 15V$ $T_A = T_{AMIN}$ $T_A = T_{AMAX}$					60 45	100 75				mW mW

Note 1: For operation at elevated temperatures, these devices must be derated based on thermal resistance, and T_j max. (listed under "Absolute Maximum Ratings"). $T_j = T_A + (\theta_{JA} P_D)$.

Thermal Resistance	Cardip (J)	DIP (N)	HO8 (H)	SO-8 (B)
θ_{JA} (Junction to Ambient)	100°C/W	100°C/W	170°C/W	185°C/W
θ_{JC} (Junction to Case)	N/A	N/A	25°C/W	N/A

Note 2: For supply voltages less than $\pm 15V$, the absolute maximum input voltage is equal to the supply voltage.

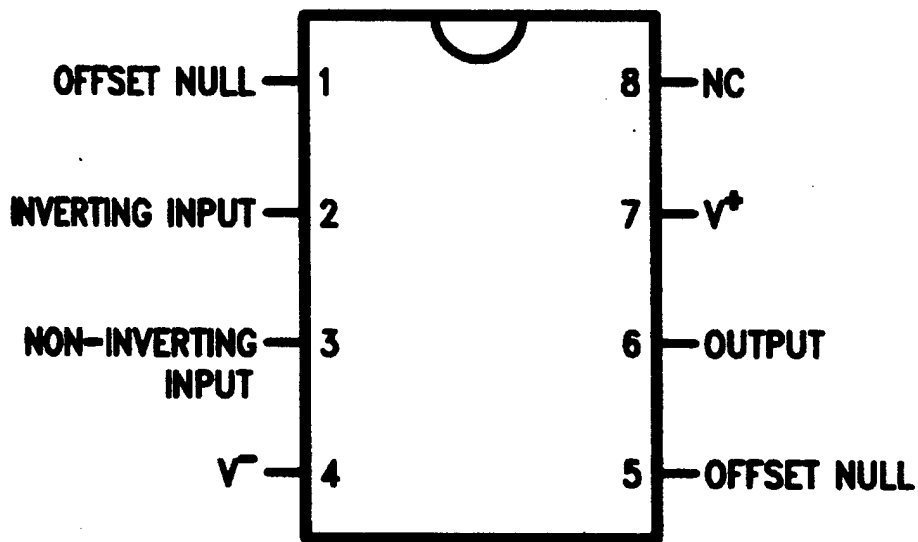
Note 3: Unless otherwise specified, these specifications apply for $V_S = \pm 15V$, $-55^\circ C \leq T_A \leq +125^\circ C$ (LM741/LM741A). For the LM741C/LM741E, these specifications are limited to $0^\circ C \leq T_A \leq +70^\circ C$.

Note 4: Calculated value from: BW (MHz) = $0.35/\text{Rise Time}(\mu s)$.

Note 5: For military specifications see RETS741X for LM741 and RETS741AX for LM741A.

Note 6: Human body model, 1.5 k Ω in series with 100 pF.

Dual-In-Line or S.O. Package

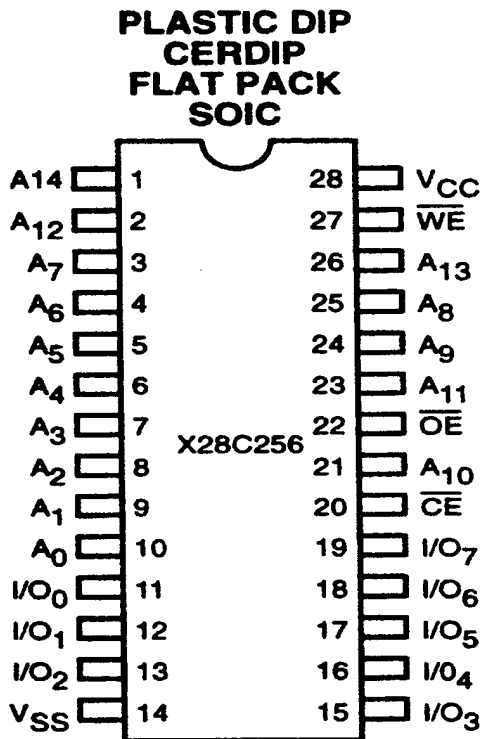


TL/H/9341-3

**Order Number LM741J, LM741J/883,
LM741CM, LM741CN or LM741EN
See NS Package Number J08A, M08A or N08E**

APPENDIX F. XICOR X28C256 DATA SHEETS

1. Pin Description



3855 FHD F02

PIN DESCRIPTIONS

Addresses (A_0 - A_{14})

The Address inputs select an 8-bit memory location during a read or write operation.

Chip Enable (\overline{CE})

The Chip Enable input must be LOW to enable all read/write operations. When \overline{CE} is HIGH, power consumption is reduced.

Output Enable (\overline{OE})

The Output Enable input controls the data output buffers and is used to initiate read operations.

Data In/Data Out (I/O_0 - I/O_7)

Data is written to or read from the X28C256 through the I/O pins.

Write Enable (\overline{WE})

The Write Enable input controls the writing of data to the X28C256.

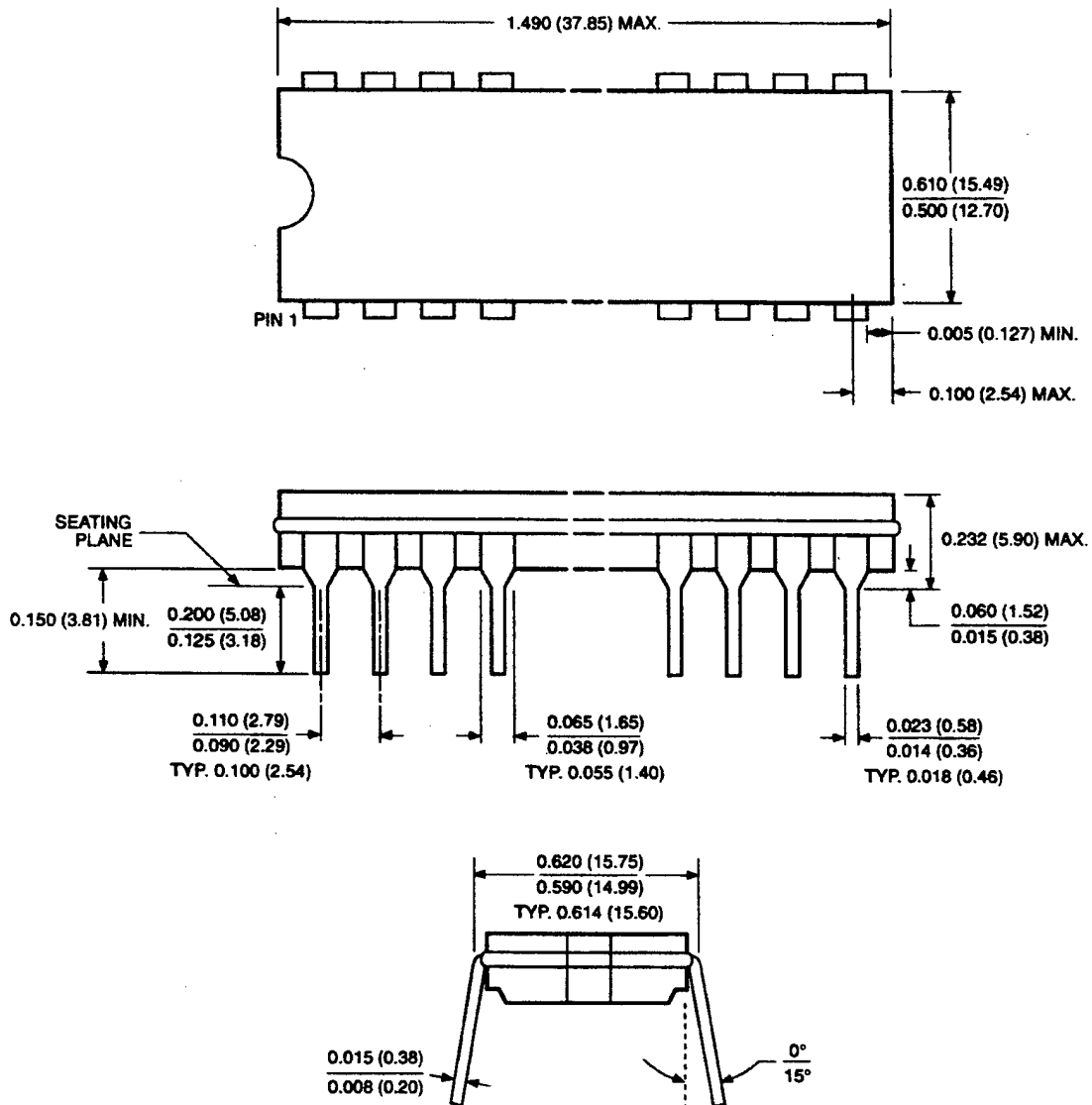
PIN NAMES

Symbol	Description
A_0 - A_{14}	Address Inputs
I/O_0 - I/O_7	Data Input/Output
\overline{WE}	Write Enable
\overline{CE}	Chip Enable
\overline{OE}	Output Enable
V_{CC}	+5V
V_{SS}	Ground
NC	No Connect

3855 PGM T01

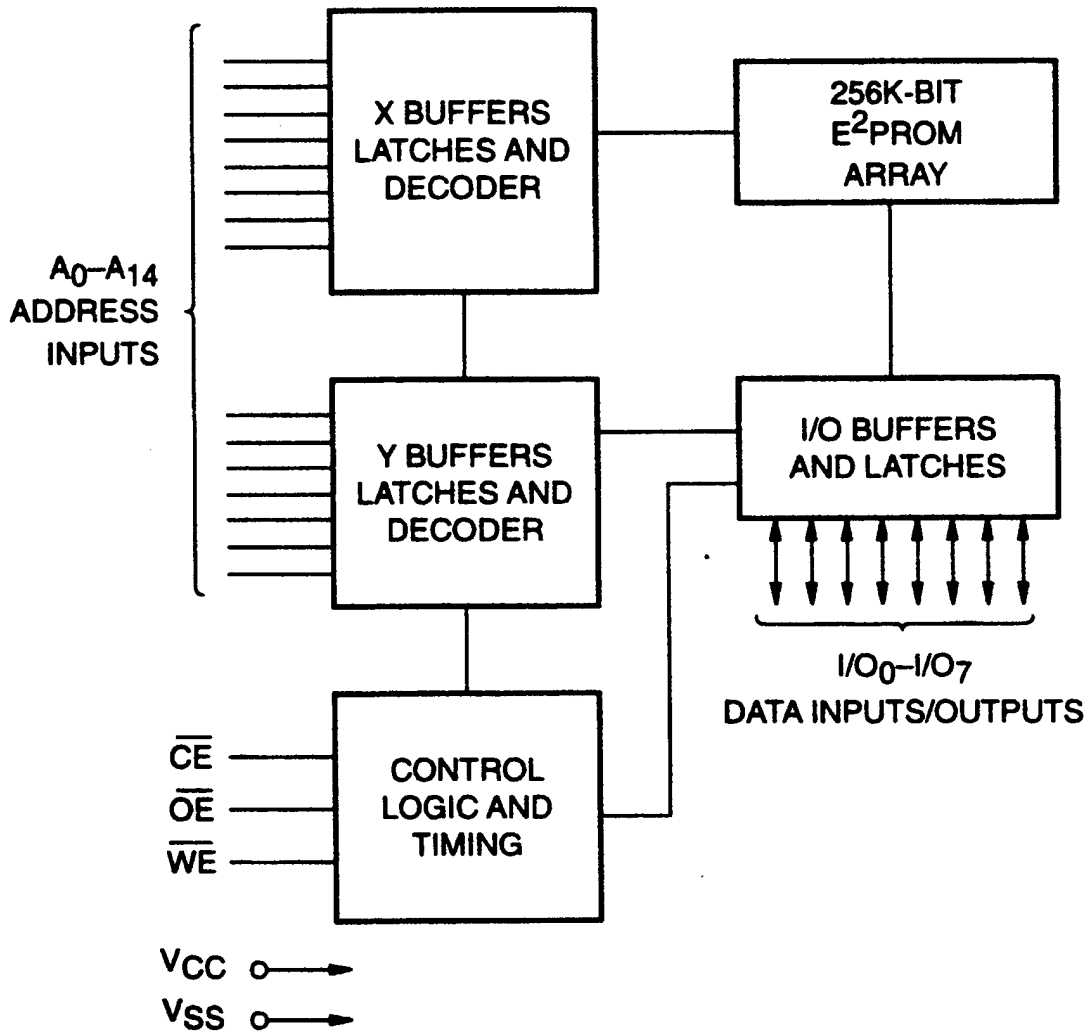
2. Packing Information

28-LEAD HERMETIC DUAL IN-LINE PACKAGE TYPE D



NOTE: ALL DIMENSIONS IN INCHES (IN PARENTHESES IN MILLIMETERS)

3. Functional Diagram



4. Characteristics

ABSOLUTE MAXIMUM RATINGS*

Temperature under Bias	
X28C256	-10°C to +85°C
X28C256I, X28C256M	-65°C to +135°C
Storage Temperature	-65°C to +150°C
Voltage on any Pin with Respect to V _{SS}	-1V to +7V
D.C. Output Current	5mA
Lead Temperature (Soldering, 10 seconds)	300°C

*COMMENT

Stresses above those listed under "Absolute Maximum Ratings" may cause permanent damage to the device. This is a stress rating only and the functional operation of the device at these or any other conditions above those indicated in the operational sections of this specification is not implied. Exposure to absolute maximum rating conditions for extended periods may affect device reliability.

RECOMMENDED OPERATING CONDITIONS

Temperature	Min.	Max.
Commercial	0°C	+70°C
Industrial	-40°C	+85°C
Military	-55°C	+125°C

3855 PGM T02.1

Supply Voltage	Limits
X28C256	5V ±10%

3855 PGM T03.1

D.C. OPERATING CHARACTERISTICS (over recommended operating conditions, unless otherwise specified)

Symbol	Parameter	Limits			Units	Test Conditions
		Min.	Typ.(1)	Max.		
I _{CC}	V _{CC} Current (Active) (TTL Inputs)		30	60	mA	$\overline{CE} = \overline{OE} = V_{IL}$, $WE = V_{IH}$, All I/O's = Open, Address Inputs = .4V/2.4V @ f = 5MHz
I _{SB1}	V _{CC} Current (Standby) (TTL Inputs)		1	2	mA	$\overline{CE} = V_{IH}$, $\overline{OE} = V_{IL}$ All I/O's = Open, Other Inputs = V _{IH}
I _{SB2} (2)	V _{CC} Current (Standby) (CMOS Inputs)		200	500	μA	$\overline{CE} = V_{CC} - 0.3V$, $\overline{OE} = V_{IL}$ All I/O's = Open, Other Inputs = V _{CC} - 0.3V
I _{LI}	Input Leakage Current			10	μA	V _{IN} = V _{SS} to V _{CC}
I _{LO}	Output Leakage Current			10	μA	V _{OUT} = V _{SS} to V _{CC} , $\overline{CE} = V_{IH}$
V _{IL} (3)	Input LOW Voltage	-1		0.8	V	
V _{IH} (3)	Input HIGH Voltage	2		V _{CC} + 1	V	
V _{OL}	Output LOW Voltage			0.4	V	I _{OL} = 2.1mA
V _{OH}	Output HIGH Voltage	2.4			V	I _{OH} = -400μA

3855 PGM T04.2

- Notes: (1) Typical values are for T_A = 25°C and nominal supply voltage and are not tested
 (2) I_{SB2} max. of 200μA available from Xicor. Contact local sales office and reference X28C256 C7125.
 (3) V_{IL} min. and V_{IH} max. are for reference only and are not tested.

ENDURANCE AND DATA RETENTION

Parameter	Min.	Units
Endurance	100,000	Cycles
Data Retention	100	Years

3855 PGM T05.3

POWER-UP TIMING

Symbol	Parameter	Max.	Units
$t_{PUR}^{(4)}$	Power-up to Read Operation	100	μ s
$t_{PUW}^{(4)}$	Power-up to Write Operation	5	ms

3855 PGM T06

CAPACITANCE $T_A = +25^\circ\text{C}$, $f = 1\text{MHz}$, $V_{CC} = 5\text{V}$

Symbol	Parameter	Max.	Units	Test Conditions
$C_{IO}^{(4)}$	Input/Output Capacitance	10	pF	$V_{IO} = 0\text{V}$
$C_{IN}^{(4)}$	Input Capacitance	6	pF	$V_{IN} = 0\text{V}$

3855 PGM T07.1

A.C. CONDITIONS OF TEST

Input Pulse Levels	0V to 3V
Input Rise and Fall Times	10ns
Input and Output Timing Levels	1.5V

3855 PGM T08.1

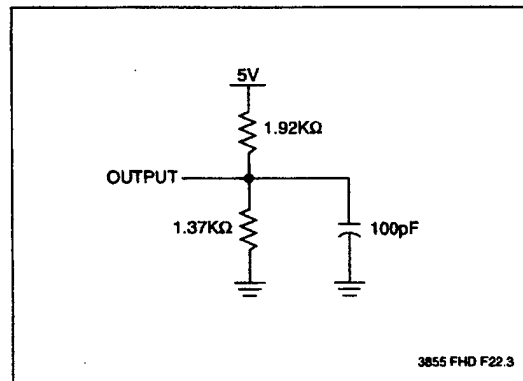
MODE SELECTION

$\overline{\text{CE}}$	$\overline{\text{OE}}$	$\overline{\text{WE}}$	Mode	I/O	Power
L	L	H	Read	D_{OUT}	Active
L	H	L	Write	D_{IN}	Active
H	X	X	Standby and Write Inhibit	High Z	Standby
X	L	X	Write Inhibit	—	—
X	X	H	Write Inhibit	—	—

3855 PGM T09

Note: (4) This parameter is periodically sampled and not 100% tested.

EQUIVALENT A.C. LOAD CIRCUIT



SYMBOL TABLE

WAVEFORM	INPUTS	OUTPUTS
	Must be steady	Will be steady
	May change from LOW to HIGH	Will change from LOW to HIGH
	May change from HIGH to LOW	Will change from HIGH to LOW
	Don't Care: Changes Allowed	Changing: State Not Known
	N/A	Center Line is High Impedance

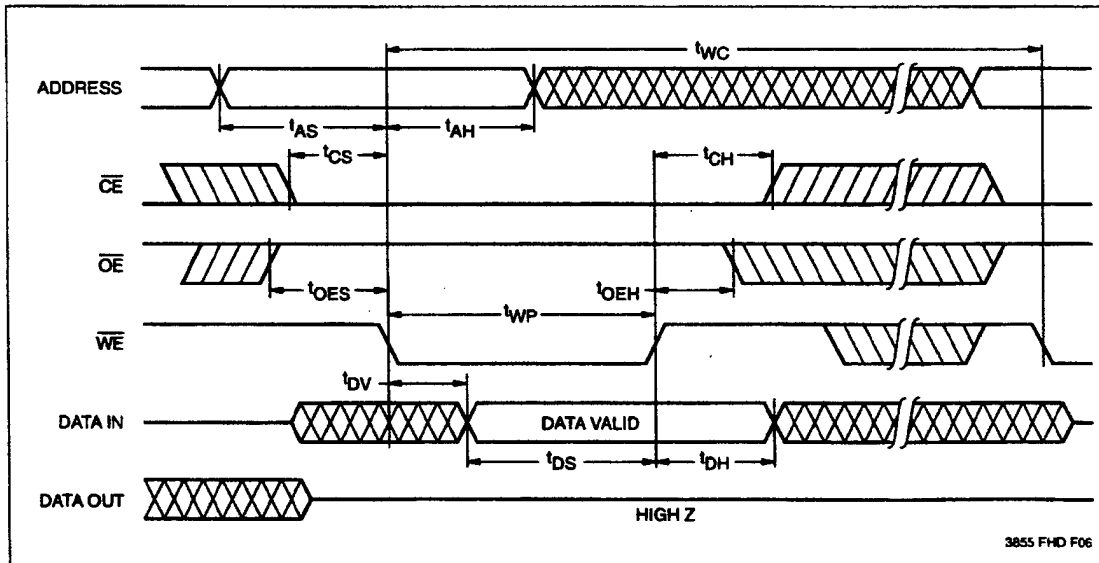
5. WE Controlled Write Cycle

WRITE CYCLE LIMITS

Symbol	Parameter	Min. ⁽⁹⁾	Typ. ⁽⁶⁾	Max.	Units
$t_{WC}^{(7)}$	Write Cycle Time		5	10	ms
t_{AS}	Address Setup Time	0			ns
t_{AH}	Address Hold Time	150			ns
t_{CS}	Write Setup Time	0			ns
t_{CH}	Write Hold Time	0			ns
t_{CW}	\overline{CE} Pulse Width	100			ns
t_{OES}	\overline{OE} HIGH Setup Time	10			ns
t_{OEH}	\overline{OE} HIGH Hold Time	10			ns
t_{WP}	\overline{WE} Pulse Width	100			ns
t_{WPH}	\overline{WE} HIGH Recovery	50			ns
$t_{WPH2}^{(8)}$	SDP \overline{WE} Recovery	1			μ s
t_{DV}	Data Valid			1	μ s
t_{DS}	Data Setup	50			ns
t_{DH}	Data Hold	10			ns
t_{DW}	Delay to Next Write	10			μ s
$t_{BLC}^{(9)}$	Byte Load Cycle	1		100	μ s

3855 PGM T11.1

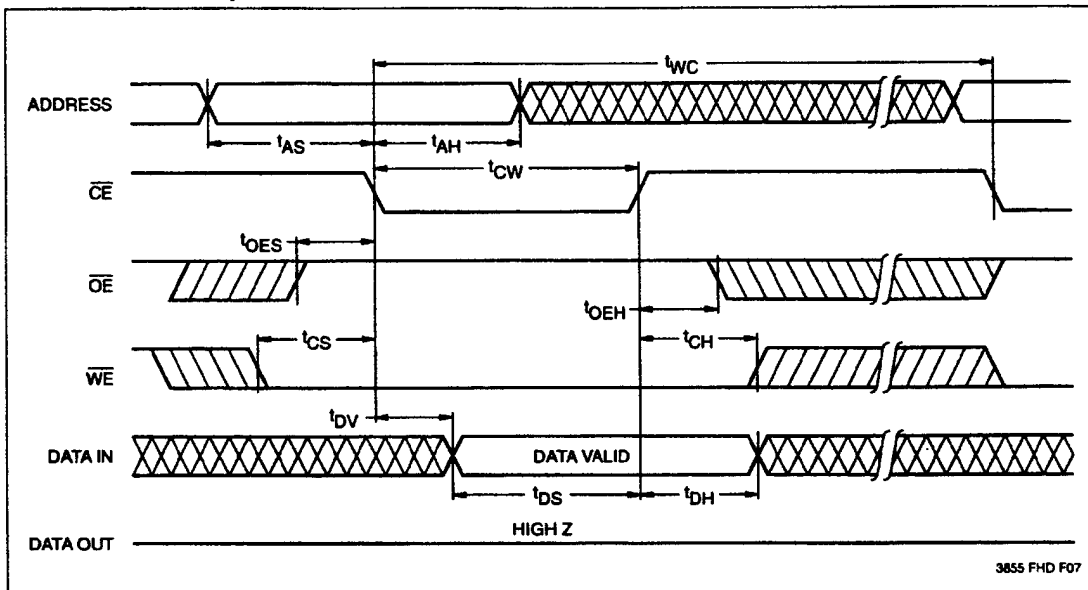
WE Controlled Write Cycle



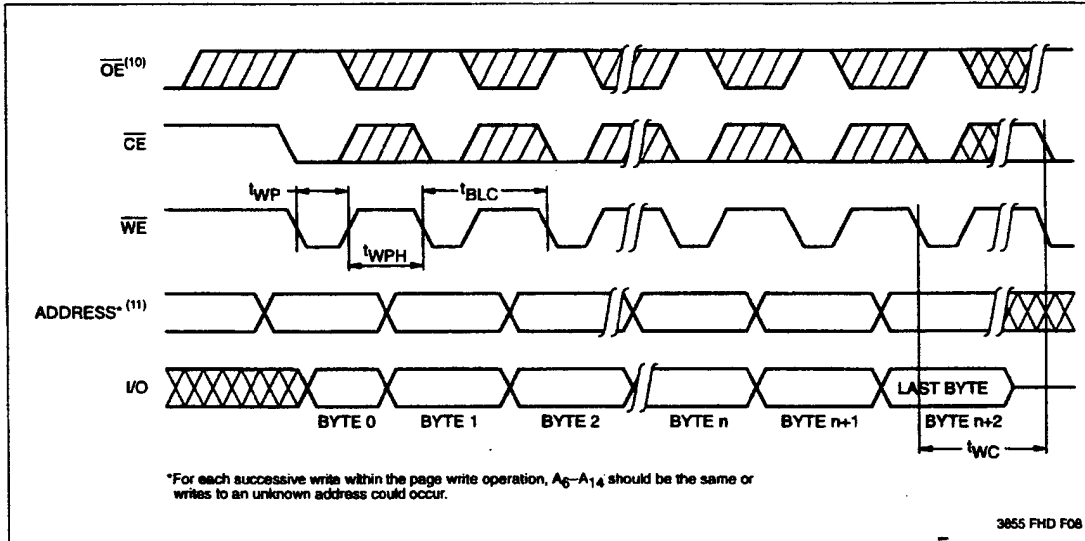
- Notes: (6) Typical values are for $T_A = 25^\circ\text{C}$ and nominal supply voltage.
 (7) t_{WC} is the minimum cycle time to be allowed from the system perspective unless polling techniques are used. It is the maximum time the device requires to automatically complete the internal write operation.
 (8) t_{WPH} is the normal page write operation \overline{WE} recovery time. t_{WPH2} is the \overline{WE} recovery time needed only after the end of issuing the three-byte SDP command sequence and before writing the first byte of data to the array. Refer to Figure 6 which illustrates the t_{WPH2} requirement.
 (9) For faster t_{WC} and t_{BLC} , refer to X28HC256 or X28VC256.

6. CE Controlled Write Cycle

$\overline{\text{CE}}$ Controlled Write Cycle



Page Write Cycle



- Notes:**
- (10) Between successive byte writes within a page write operation, $\overline{\text{OE}}$ can be strobed LOW: e.g. this can be done with $\overline{\text{CE}}$ and $\overline{\text{WE}}$ HIGH to fetch data from another memory device within the system for the next write; or with $\overline{\text{WE}}$ HIGH and $\overline{\text{CE}}$ LOW effectively performing a polling operation.
 - (11) The timings shown above are unique to page write operations. Individual byte load operations within the page write must conform to either the $\overline{\text{CE}}$ or $\overline{\text{WE}}$ controlled write cycle timing.

LIST OF REFERENCES

1. Stephen E. Lipsky, *Microwave Passive Direction Finding*, John Wiley & Sons, Inc., NY, 1987.
2. Herndon H. Jenkins, *Small-Aperture Radio Direction Finding*, Artech House Inc, Norwood, MA, 1991.
3. Curtis Schleher, Ph. D., *Introduction to Electronic Warfare*, Artech House Inc., Dedham, MA, 1987.
4. D. C. Jenn, P. E. Pace, T. Hatzathanasiou, R. Vitale, "Symmetrical Number System Phase Sampled DF Antenna Architectures", *1998 IEEE AP-S International Symposium and URSI North American Radio Science Meeting*, June 1998.
5. Panagiotis Papandreou, "Design and Prototype Development of an Optimum Symmetrical Number System Direction Finding Array", Naval Postgraduate School Master's Thesis, March 1997.
6. P. E. Pace, J. L. Schafer, D. Styer, "Optimum Analog Preprocessing for Folding ADCs," *IEEE Transactions on Circuits and Systems-II: Analog and Digital Signal Processing*, Vol. 42, No 12, pp 825-829, December 1995.
7. P. E. Pace, P. A. Ramamoorthy, David Styer, "A Preprocessing Architecture for Resolution Enhancement in High-Speed Analog-to-Digital Converters", *IEEE Transactions on Circuits and Systems--II: Analog and Digital Signal Processing*, Vol. 41, No. 6, pp. 373—379, June 1994.
8. P. E. Pace, W. Ringer, K. Foster, and J. Powers, "Optical Signal Integrity and Interpolation Signal Processing in Wideband SNS Digital Antennas," *Proc. 1997 DARPA Photonic Systems for Antenna Applications*, Jan. 13, 1997.
9. P. E. Pace, R. Leino, and D. Styer, "Use of the Symmetrical Number System in Resolving Single-Frequency Undersampling Aliases," *IEEE Trans. On Signal Processing*, Vol.45, pp.1153—1160, May.
10. D. C. Jenn, P. E. Pace, T. Hatzathanasiou, R. Vitale, "High Resolution Wideband Direction Finding Arrays based on Optimum Symmetrical Number System Encoding", *Institution of Electrical Engineers accepted for publication*, April 1998.
11. Constantine A. Balanis, *Antenna Theory, Analysis and Design*, John Wiley & Sons, Inc., York, NY, 1997.

12. Luis E. Moita Rodrigues, "High-Resolution Residue Antenna Architectures for Wideband Direction Finding," Naval Postgraduate School Master's Thesis, June 1996.
13. John G. Proakis and Dimitris G. Manolakis, *Digital Signal Processing Principles, Algorithms, and Applications*, Prentice Hall, Inc., Simon & Schuster/A Viacom Company, Upper Saddle River, NJ, 1996.
14. James Bao-Yen Tsui, *Digital Techniques for Wideband Receivers*, Artech House, Inc., 685 Canton Street, Norwood MA, 1995.
15. Byron Edde, *Radar Principles, Technology, Applications*, Prentice-Hall, Inc, Upper Saddle River, NJ, 1993.
16. George B. Rutkowski, P.E., *Operational Amplifiers: Integrated and Hybrid Circuits*, John Wiley & Sons, Inc., 605 Third Avenue, New York NY, 1993.
17. MAXIM, *MAX916, Ultra High-Speed, High-Resolution, Single-/Dual-Supply TTL Comparators*, Maxim Integrated Products, Sunnyvale, CA, Rev 0; 9/1993.
18. Adel S. Sedra and Kenneth C. Smith, *Microelectronic Circuits*, Oxford University Press, Inc., 198 Madison Avenue, New York, NY, 1998.
19. National Instruments, *LabVIEW Data Acquisition VI Reference Manual*, National Instruments Corporate Headquarters, Austin, TX, 1995.
20. National Semiconductor, *LM 741 Operational Amplifier*, National Semiconductor Corporation, Santa Clara, CA, 1995.
21. Xicor, *X28C256, 32Kx8Bit, Byte Alterable EEPROM*, Xicor Inc. Milpitas, CA, 1998.

INITIAL DISTRIBUTION LIST

	No of Copies
1. Defense Technical Information Center 2 8725 John J. Kingman Rd., STE 0944 Ft. Belvoir, VA 22060-6218	
2. Dudley Knox Library 2 Naval Postgraduate School 411 Dyer Rd. Monterey, Ca 93943-5101	
3. Chairman, Code PH 1 Department of Physics Naval Postgraduate School Monterey, CA, 93943-5121	
4. Professor Phillip E. Pace, Code EC/PC 2 Department of Electrical and Computer Engineering Naval Postgraduate School Monterey, CA, 93943-5121	
5. Professor David D. Cleary, Code PH/CL 1 Physics Department Naval Postgraduate School Monterey, CA, 93943-5121	
6. Professor David C. Jenn, Code EC/JN 1 Department of Electrical and Computer Engineering Naval Postgraduate School Monterey, CA, 93943-5121	
7. Bob Vitale, Code EC/EL 1 Department of Electrical and Computer Engineering Naval Postgraduate School Monterey, CA, 93943-5121	
8. Major Thomas N. Hatziathanasiou 3 Andromahis 16, P. Faliro, Athens, 17564, GREECE	

8. Efstratios Hatziathanasiou 2
Adramitiou 7, Neapolis,
Thessaloniki, 56728, GREECE